



UNIVERSIDADE FEDERAL DE PERNAMBUCO
CENTRO DE TECNOLOGIA E GEOCIÊNCIAS
DEPARTAMENTO DE ENGENHARIA MECÂNICA
PROGRAMA DE PÓS-GRADUAÇÃO EM ENGENHARIA MECÂNICA

Gustavo Galindez Ramirez

**Numerical simulation of two-phase flow in petroleum reservoirs using high-order CPR
method coupled to a non-orthodox MPFA-D finite volume scheme**

Recife

2018

Gustavo Galindez Ramirez

Numerical simulation of two-phase flow in petroleum reservoirs using high-order CPR method coupled to a non-orthodox MPFA-D finite volume scheme

A thesis submitted to the graduate program as a partial fulfillment of the requirement for the award of Doctor in Engineering degree

Supervisor: Paulo Roberto Maciel Lyra

Co-supervisor: Darlan karlo Elisiário de Carvalho

Recife

2018

Catálogo na fonte
Bibliotecário Gabriel Luz, CRB-4 / 2222

R173n Ramirez, Gustavo Galindez.
Numerical simulation of two-phase flow in petroleum reservoirs using high-order CPR method coupled to a non-orthodox MPFA-D finite volume scheme / Gustavo Galindez Ramirez - 2018.
100 folhas, figs.; tabs.; abrev. e simb.

Orientador: Prof. Dr. Paulo Roberto Maciel Lyra.
Coorientador: Prof. Dr. Darlan Karlo Elisiário de Carvalho.

Tese (Doutorado) – Universidade Federal de Pernambuco. CTG.
Programa de Pós-Graduação em Engenharia Mecânica, 2018.
Inclui Referências e Anexos.

1. Engenharia Mecânica. 2. High order methods. 3. CPR. 4. MLP. 5. MPFA-D. 6. IMPES. 7. Raviart-Thomas interpolation. 8. The Piola transformation. 9. Two-phase flows in porous media. I. Lyra, Paulo Roberto Maciel. (Orientador). II. Carvalho, Darlan Karlo Elisiário de. (Coorientador). III. Título.

UFPE

621 CDD (22. ed.) BCTG/2019 - 87

Gustavo Galindez Ramirez

Numerical simulation of two-phase flow in petroleum reservoirs using high-order CPR method coupled to a non-orthodox MPFA-D finite volume scheme

A thesis submitted to the graduate program as a partial fulfillment of the requirement for the award of Doctor in Engineering degree

The PhD evaluation committee with the following examiners, coordinated by the first, considers the PhD candidate **Gustavo Galindez Ramirez, Approved**. Recife, november 30th of 2018:

Prof. Dr. Paulo Roberto Maciel Lyra
Orientador - UFPE

Prof. Dr. Darlan Karlo Elisiário de Carvalho
Coorientador - UFPE

Prof. Dr. Maicon Ribeiro Correa
Unicamp

Prof. Dr. Ramiro Brito Willmersdorf
UFPE

Prof. Dr. Alessandro Romario Echevarria
Antunes
UFPE

Prof. Dr. Márcio Rodrigo de Araújo Souza
UFPB

To my parents, my wife and my son.

ACKNOWLEDGEMENTS

First of all, I want to thank my supervisors Paulo Roberto Maciel Lyra and Darlan Karlo Elisiário de Carvalho for their patience, help, and extended critiques of my work during my DSc project.

I would also thank Fernando Contreras and Márcio Souza as for support using the MPFA-D solver and for using their source code. Thanks to Manuel Diaz for help on different subjects, including the CPR-algorithm and initial source code.

Thanks to Alexandra Asanovna Elbakyan, for her contribution to freedom of scientific knowledge.

Finally, the author gratefully acknowledge the financial support provide by the Pernambuco Research Agency FACEPE, Energi Simulation, The Brazilian Research Council CNPq and CENPES-PETROBRAS.

ABSTRACT

The study and development of high resolution numerical approximations for the modeling and simulation of multiphase flows in petroleum reservoirs is still a challenge, from the computational viewpoint, due to the difficulties posed by some physical features such as heterogeneity and anisotropy of the medium, that are of paramount importance in this class of applications. Several methods have been proposed in the past that are based on FD (Finite-Difference), FV (Finite-Volume) or FE (Finite-Element). These methods, in their classical formulations, are of low order of approximation and suffer excessive smearing at saturation front introducing error into the numerical solution. These deficiencies can be mitigated or suppressed using high-resolution methods such as the k -exact or ENO (Essentially non-Oscillatory) FV methods, which require large stencils to reconstruct high order polynomial within a control volume, resulting in an increase of the storage requirements and computational cost. On the other hand, over the last decades DG (Discontinuous Galerkin), SV (Spectral Volume), SD (Spectral Difference) and FR (Flux Reconstruction)/CPR (Correction Procedure via Reconstruction) methods were developed, which can achieve high order accuracy via a compact stencil consisting of the current cell and its immediate neighbors. In addition, the FR/CPR recovery simplified versions of nodal DG, SV and SD methods by choosing an adequate polynomial reconstruction function, whose coefficients are preprocessed and stored. The focus of this work is to investigate and to apply a very high resolution CPR method for the discretization of the saturation equation, which is generally advection-dominated and that results from the modeling of the 2-D Oil-Water displacement through porous formations. In order to suppress numerical oscillations (under/overshoots) near shocks that are typical in higher order schemes, and handling the high accuracy in smooth regions of the solution a hierarchical multi-dimensional limiting strategy (MLP) is used in the reconstruction stage. The integration in time is carried out using a third-order Runge-Kutta method. To solve the pressure equation a non-orthodox cell centered MPFA-D (Multipoint Flux Approximation-*Diamond* type) finite volume method is employed. In order to properly couple the MPFA-D method with the CPR formulation, it is necessary to obtain an adequate velocity reconstruction throughout the control volumes of the mesh. Because the cell-centered finite volume method naturally delivers fluxes across cell faces that belong to the primal grid, a reconstruction operator based on the lowest Raviart-Thomas interpolation functions and the Piola transformation is built, to get the complete knowledge of conservative velocity field throughout the domain. The reconstruction operator receives, as input, the density fluxes across control volume faces and returns the point-wise values of velocity anywhere within the cell. Finally, the coupling of the pressure-saturation system of equations is carried out using a classical IMPES (Implicit Pressure Explicit Saturation) procedure. Some two-phase flow benchmark problems in one and two dimensions were analyzed and numerical and/or analytical comparisons have been used to verify the accuracy, efficiency and shock-capturing capability of the proposed methodology.

Keywords: High Order Methods. CPR. MLP. MPFA-D. IMPES. Raviart-Thomas interpolation. The Piola transformation. Two-phase flows in porous media.

RESUMO

O estudo e desenvolvimento de aproximações numéricas de alta resolução para a modelagem e simulação de fluxos multifásicos em reservatórios de petróleo ainda é um desafio do ponto de vista computacional, devido às dificuldades colocadas por algumas características físicas tais como heterogeneidade e anisotropia do meio, que são de suma importância nesta classe de aplicações. Vários métodos foram propostos no passado, baseados em FD (diferenças finitas), FV (volumes finitos) ou FE (elementos finitos). Esses métodos, nas suas formulações clássicas, são de baixa ordem de aproximação e sofrem excessiva suavização na frente de saturação, introduzindo erro na solução numérica. Estas deficiências podem ser mitigadas ou suprimidas usando os métodos de alta resolução, como os métodos FV *k-exact* ou ENO (*Essentially non-Oscillatory*), que requerem estênceis grandes para reconstruir polinômios de alta ordem dentro de um volume de controle, resultando em um aumento da necessidade de armazenamento e custo computacional. Por outro lado, nas últimas décadas, métodos como DG (*Discontinuous Galerkin*), SV (*Spectral Volume*), SD (*Spectral Difference*) e FR (*Flux Reconstruction*)/CPR (*Correction Procedure via Reconstruction*) foram desenvolvidos, podendo alcançar alta precisão com um estêncil compacto que consiste na célula alvo e seus vizinhos imediatos. Além disso, FR/CPR recupera versões simplificadas dos métodos nodais DG, SV e SD usando uma função de reconstrução polinomial adequada, cujos coeficientes são pré-processados e armazenados. O foco deste trabalho é investigar e aplicar o método de alta resolução CPR para a discretização da equação de saturação, que geralmente é de advecção dominante, e que resulta da modelagem do escoamento bidimensional de óleo-água em formações porosas. A fim de suprimir oscilações numéricas (*under/ over shoots*) perto de choques que são típicos em esquemas de alta ordem e entregar a alta precisão em regiões suaves da solução, uma estratégia limitadora multidimensional hierárquica (MLP) é usada em o estágio de reconstrução. A integração no tempo é realizada usando um método Runge-Kutta de terceira ordem. Para resolver a equação de pressão, um método dos volumes finitos não-ortodoxo o MPFA-D (Aproximação do Fluxo por Múltiplos pontos-tipo Diamante) centrado na célula é empregado. Para acoplar adequadamente o método MPFA-D com a formulação do CPR é necessário obter uma reconstrução de velocidade adequada através dos volumes de controle da malha. Como o método de volumes finitos centrado na célula fornece naturalmente fluxos através das faces da célula que pertencem à malha primal, um operador de reconstrução baseado nas funções de interpolação de Raviart-Thomas de ordem mais baixa e na transformação de Piola é construído para obter o conhecimento completo do campo de velocidade conservativo em todo o domínio. O operador de reconstrução recebe, como entrada, as vazões nas faces dos volumes de controle e retorna os valores de velocidade em qualquer ponto da célula. Finalmente, o acoplamento do sistema das equações de saturação e pressão é realizado usando um procedimento clássico IMPES (*IMplicit Pressure Explicit Saturation*). Alguns problemas *benchmark* de fluxo bifásico em uma e duas dimensões são analisados e comparações numéricas e / ou analíticas foram usadas para verificar a precisão, a eficiência e a

capacidade de captura de choque da metodologia proposta.

Palavras chave: Métodos de alta ordem. CPR. MLP. MPFA-D. IMPES. Interpolação de Raviart-Thomas. Transformação de Piola. Fluxos bifásicos em meios porosos.

RESUMEN

El estudio y desarrollo de aproximaciones numéricas de alta resolución para el modelado y simulación de flujos multifásicos en yacimientos de petróleo sigue siendo un desafío, desde el punto de vista computacional, debido a las dificultades que presentan algunas características físicas tales como la heterogeneidad y la anisotropía del medio, que son de suma importancia en esta clase de aplicaciones. Varios métodos han sido propuestos en el pasado, los cuales están basados en FD (Diferencias finitas), FV (Volúmenes finitos) o FE (Elementos finitos). Estos métodos, en sus formulaciones clásicas, son de bajo orden de aproximación y sufren de excesiva dispersión en el frente de saturación introduciendo un error en la solución numérica. Esta deficiencia puede ser mitigada o suprimida usando los métodos de alta resolución como los métodos de FV *k-exact* o ENO (*Essentially non-Oscillatory*), que requieren grandes conjuntos de celdas para reconstruir polinomios de alto orden dentro de un volumen de control, lo que resulta en un aumento de la necesidad de almacenamiento y de costo computacional. Por otro lado, en las últimas décadas fueron desarrollados métodos, como, DG (Galerkin discontinuo), SV (Volumen espectral), SD (Diferencia espectral) y FR (Reconstrucción de Flujo) / CPR (Procedimiento de Corrección vía Reconstrucción), que puede lograr una precisión de alto orden a través de un conjunto de celdas compacto que consiste en la celda actual y sus vecinos inmediatos. Además, el FR / CPR recupera versiones simplificadas de los métodos nodales DG, SV y SD eligiendo una función adecuada de reconstrucción polinómica, cuyos coeficientes son preprocesados y almacenados. El objetivo de este trabajo es investigar y aplicar un método CPR de muy alta resolución para la discretización de la ecuación de saturación, que generalmente es de advección-dominante y que resulta del modelado del desplazamiento 2-D de petróleo-agua a través de formaciones porosas. Para suprimir las oscilaciones numéricas (*under/ over shoots*) cerca de choques que son típicos en esquemas de orden superior, y para entregar alta precisión en regiones suaves de la solución, se utiliza una estrategia de limitación multidimensional jerárquica (MLP) en la etapa de reconstrucción. La integración en el tiempo se lleva a cabo utilizando un Método de Runge-Kutta de tercer orden. Para resolver la ecuación de presión, un método de volúmenes finitos no ortodoxo MPFA-D (Aproximación de flujo por múltiples puntos-tipo diamante) centrado en la celda es empleado. Para poder combinar el método MPFA-D con la formulación de CPR, es necesario obtener una reconstrucción adecuada de la velocidad a través de los volúmenes de control de la malla. Debido a que el método de volúmenes finitos centrado en la celda proporciona naturalmente flujos a través de las caras de las celdas que pertenecen a la malla primaria, se construye un operador de reconstrucción basado en las funciones de interpolación de Raviart-Thomas de mas bajo orden y la transformación Piola, para obtener el conocimiento completo del campo de velocidad conservativo en todo el dominio. El operador de reconstrucción recibe, como entrada, la densidad de flujos a través del volumen de control y devuelve los valores puntuales de velocidad en cualquier lugar dentro de la celda. Finalmente, el acoplamiento del sistema de ecuaciones de saturación y de presión se lleva a cabo utilizando

un procedimiento clásico IMPES (*Implicit Pressure Explicit Saturation*). Algunos problemas modelo para el flujo bidimensional en una y dos dimensiones se llevaron a cabo y se usaron comparaciones numéricas y / o semi-analíticas para verificar la precisión, eficiencia y capacidad de captura de discontinuidades de la metodología propuesta.

Palabras clave: Métodos de alto orden. CPR. MLP. MPFA-D. IMPES. Interpolación de Raviart-Thomas. La transformación Piola. Flujos bifásicos en medios porosos.

LIST OF FIGURES

Figure 1	– Reservoir model, illustrating the displacement of oil by water in a system of dip angle θ .	31
Figure 2	– Relative permeability functions for water-oil phases.	32
Figure 3	– External and internal boundaries in Ω domain.	33
Figure 4	– IMPES methodology algorithm.	34
Figure 5	– Part of a polygonal mesh, illustrating the diamond path.	36
Figure 6	– Part of a quadrilateral mesh, illustrating the RT_0 velocity interpolation.	37
Figure 7	– MPFA-D Pressure field and RT_0 velocity reconstruction for quadrangular grids (a) Homogeneous quarter of five spot configuration and (b) Heterogeneous quarter of five spot configuration.	39
Figure 8	– P_3 degree solution polynomials, including cell interfaces.	42
Figure 9	– Solution and flux points on reference 2D domain for P_2 approximation.	43
Figure 10	– Correction function g_{DG} and its derivative g'_{DG} , for $n = 1$.	44
Figure 11	– Spectral accuracy of the SV/SD, DG and CPR schemes using p-refinement, for the advection equation (a) A close-up view of spectral accuracy test (b).	47
Figure 12	– Buckley Leverett problem for $t = 0.4$, 80 cells and $CFL = 0.9$ (a) Solution using a low-order approximation (b) Solution using a high-order approximation.	50
Figure 13	– MLP stencil for Ω_i .	52
Figure 14	– Flowchart of the hierarchical MLP limiting procedure, solid green line \rightarrow if criteria is satisfied, and dashed red line \rightarrow else.	53
Figure 15	– Buckley Leverett problem for $t = 0.4$, 32 cells and $CFL = 0.9$ (a) Solution without gravity effect (b) Solution with gravity effect.	54
Figure 16	– Solution point on reference domain.	55
Figure 17	– Solution at $t = 2$.	59
Figure 18	– Stability regions of the Runge-Kutta method in the complex $\Omega\Delta t$ -plane, from 1 to 4 stages.	61
Figure 19	– Rates of spatial convergence from the grid refinement studies using a CPR- P_3 spatial reconstructions for the 1D linear wave equation at $t = 2$ with $CFL = 0.9$ (a) Solution using a first-order forward Euler scheme (b) Solution using a third-order TVD-RK method.	62
Figure 20	– Quarter five-spot problem set-up, using a five-spot pattern, with four injection wells on the corners and one production well at the center.	64
Figure 21	– Buckley Leverett problem for $t=1,500$ days (a) p-refinement and (b) h-refinement.	67
Figure 22	– Domain $\Omega = \Omega_I \cup \Omega_{II}$.	67
Figure 23	– Two-phase flow in heterogeneous porous media with capillary pressure effect for $t = 0.45$ and $CFL = 0.9$.	68
Figure 24	– Two-phase flow in heterogeneous porous media with capillary pressure effect for $t = 0.45$ and $CFL = 0.9$, for FOU- P_0 (250 cells) \times CPR- P_3 (50 cells).	69

Figure 25 – Saturation profiles at different time levels on a quarter five-spot problem computed on a uniform Cartesian grid up to water-breakthrough in the production well, with CFL = 0.9: (a) to (c) Shows the reference solution, (d) to (f) gives the FOU- P_0 results and (g) to (i) illustrates the CPR- P_3 solutions.	70
Figure 26 – Cross-section curves for a homogeneous quarter of a five spot problem for quadrangular structured grids up to PVI = 0.3 and CFL = 0.9. (a) FOU method, (b) CPR- P_3	71
Figure 27 – Cross-section comparison for a homogeneous quarter of a five spot problem using a quadrangular structured grid, PVI=0.3 and CFL = 0.9, via a FOU method and CPR- P_3	71
Figure 28 – Production curves for a homogeneous quarter of a five spot problem for 16×16 quadrangular structured grid, PVI=1.0 and CFL = 0.9, using a FOU method, MUSCL, CPR- P_1 to CPR- P_3 (a) Oil-recovery (b) Close-view (c) Cumulative oil (d) Close-view.	73
Figure 29 – Saturation profiles for different time levels on a quarter five-spot problem with a low-permeability region computed on an unstructured grid with 1,158 cells, up to water-breakthrough in the production well, using a P_3 degree polynomial and CFL = 0.9.	74
Figure 30 – Comparison between low-order and high-order methods for a heterogeneous quarter of five a spot problem with low-permeability region in domain using 330 CVs and at PVI = 0.3.	75
Figure 31 – Comparison between low-order and high-order methods for a heterogeneous quarter of five a spot cascade problem, up to water-breakthrough in the production well, CFL = 0.9.	77
Figure 32 – \log_{10} permeability field, layer 14.	78
Figure 33 – Saturation profiles at different values of PVI for the layer 14 of the SPE-10 model, using 1024 CVs and CFL = 0.9.	79
Figure 34 – Heterogeneous reservoir with a discontinuous full tensor with a high anisotropy ratio.	80
Figure 35 – Comparison between low-order and high-order methods for a anisotropic medium in a quarter of five a spot configuration, using a 32×32 structured mesh at PVI = 0.16.	81
Figure 36 – Saturation contours for a homogeneous quarter of a five spot problem for 40×40 quadrangular structured (diagonal) grid, PVI=0.2 CFL = 0.9 and a adverse water/oil mobility ratio $M = 10$ and $M = 100$ first and second column, respectively, using (a-b) FOU method, (c-d) MUSCL, (e-f) CPR- P_1 and (g-h) CPR- P_3	83
Figure 37 – Part of a polygonal mesh, illustrating the diamond path.	97
Figure 38 – Interaction region for the LPEW (Linearity Preserving Explicit Weighted) interpolation. On the left is shown the geometry for the interaction region in a grid fragment. On the right is illustrated the detail of the interaction region.	100

LIST OF TABLES

Table 1	– Correction lifting coefficients, $g'_{DG(L,j)}$, for linear element $[-1,1]$	44
Table 2	– Correction lifting coefficients, $g'_{(SD/SV)L,j}$, for linear element $[-1,1]$	45
Table 3	– Correction lifting coefficients- $g'_{2(L,j)}$, for linear element $[-1,1]$	45
Table 4	– Accuracy study for 1-D linear advection equation CPR- g_2 SV/SD and DG, using Gauss-Lobatto distribution.	46
Table 5	– The weights w_l for Gauss-Lobatto nodes ξ_l , which are used to calculate the cell averages.	56
Table 6	– The Legendre polynomials P_n	57
Table 7	– Relevant data used in semi-analytical and numerical computation.	65
Table 8	– Error and convergence test of the MUSCL-TVD (cell-centered) and the SV/SD/NDG schemes, using second order accuracy.	66
Table 9	– CPU-time (sec) for different grid sizes and polynomial approximation.	69
Table 10	– CPU-time (min) for different grid sizes and polynomial approximation.	72

List of abbreviations and acronyms

CPR	Correction Procedures via Reconstruction Method.
CFD	Computational Fluid Dynamic.
CFL	Courant-Friedrichs-Lewy Condition.
DG	Discontinuous Galerkin.
DOF	Degrees of freedom.
DMP	Discrete Maximum Principle.
FOU	First-Order Upwind.
FV	Finite Volume.
FP	Flux Point.
FR	Flux Reconstruction Method.
IMPES	Implicit Pressure Explicit Saturation.
LCP	Lifting Collocation Penalty.
LHS	Left-Hand-Side.
LPEW	Linearity-Preserving Explicit Weighted.
MLP	Multi-Dimensional Limiting Procedure.
MPFA	Multi-Point Flux Approximation.
MPFA-D	Multi-Point Flux Approximation- <i>Diamond</i> type.
SD	Spectral Finite Difference Method.
SP	Solution Point.
SV	Spectral Finite Volume Method.
TVB	Total Variation Boundary.
TVD	Total Variation Diminishing.

List of symbols

Vectors and matrices

\vec{F}	Flux function.
\vec{g}	Vector pointing in the direction of gravity.
\mathcal{J}	Jacobian matrix.
\tilde{K}	Absolute rock permeability tensor.
\vec{N}	Surface area normal vector to control surface.
\mathcal{V}	Vandermonde matrix.
\vec{v}	Average mid-edge face velocity.
\vec{v}_α	Total phase velocity.

Roman letters

f	Fractional flow.
\mathcal{F}	Riemann Flux.
F^n	Normal flux.
F	Flux density through a face.
g_D	Prescribed pressure scalar function.
g_N	Prescribed flux scalar function.
$g'_{L,R}$	Lifting constants.
$k_{r\alpha}$	Phase relative permeability.
\mathcal{P}	Piola transform.
P	Polynomial degree.
p	Pressure.
q_α	Source or sink terms of phase velocity.
Q	The total fluid injection or production specific rate.
S_α	Phase Saturation.

\bar{S}_w	Prescribed saturation in a set of injection wells.
\bar{S}_w^0	Initial saturation distribution.
W	Test function.
$R_{R,n}$	Right Randau polynomial of degree n .

Greek letters

δ	Correction function.
ϕ	Rock Porosity.
Γ_D	Dirichlet boundary
Γ_N	Neumann boundary.
Γ_I	Injection well.
Γ_P	Production well.
λ	Mobility.
ρ_α	Phase density.
μ_α	Phase viscosity.
Π	Projection operator.
Ω	Domain.
θ	Dip angle.

Superscripts

$n + 1$	Order of accuracy of the scheme.
m	Order of degree polynomial projection..

Subscripts

α	Phase index.
c	Capillary pressure.
i	Cell index.
I, J	Edge connecting vertices.

IJ	Control face.
j, k	Solution point index.
n	n th-degree polynomial.
\hat{L}, \hat{R}	Left and right sides edge.
o	Oil fluid.
w	Water fluid.

CONTENTS

1	INTRODUCTION	21
1.1	Motivation	22
1.2	Objetives	22
1.3	Contents	22
2	LITERATURE REVIEW	24
3	MATHEMATICAL MODEL	28
3.1	Governing equations	28
3.1.1	Initial and boundary conditions	31
4	NUMERICAL FORMULATION	34
4.1	Pressure/Velocity solver	34
4.1.1	MPFA-D Method	35
4.1.2	Reconstruction of Darcy velocity inside the CV of a quadrilateral mesh . . .	37
4.2	Saturation/Transport solver	39
4.2.1	CPR method	39
4.2.1.1	<i>Nodal discontinuous Galerkin scheme</i>	43
4.2.1.2	<i>Spectral Difference/Spectral Volume methods</i>	44
4.2.1.3	<i>CPR-g₂ method</i>	45
4.2.1.4	<i>1D linear advection equation test</i>	46
4.2.1.5	<i>Conservation issues</i>	47
4.2.2	Approximate Riemann solvers	48
4.2.2.1	<i>Numerical example</i>	49
4.2.3	Shock capturing strategies	49
4.2.3.1	<i>TVB marker and minmod slope limiting strategy</i>	50
4.2.3.2	<i>Hierarchical MLP (Multidimensional Limiter Procedures) strategy</i>	51
4.2.3.3	<i>Numerical example</i>	54
4.3	From nodal to cell-centered solutions	55
4.3.1	Classic form using quadratures	55
4.3.2	Non classic form using the Vandermonde matrix and modal coefficients . . .	56
4.3.3	Numerical example	58
4.4	Discretization of the diffusive term	59
4.5	Explicit time discretization	60
5	NUMERICAL RESULTS	64
5.1	MUSCL vs CPR methods	65

5.2	Two-phase flow in heterogeneous porous media with capillary pressure effect	67
5.3	Homogeneous quarter of five a spot test	69
5.4	Quarter of a five spot with a low-permeability region	73
5.5	Heterogeneous and anisotropic quarter of five-spot test	76
5.6	Isotropic and highly heterogeneous porous media	78
5.7	Discontinuous full tensor with a high anisotropy ratio	80
5.8	Grid orientation effect test using a adverse mobility ratio	82
6	CONCLUSIONS AND FUTURE WORK	84
6.1	Conclusions	84
6.2	Future work	85
	REFERENCES	86
	ANNEX	95
	ANNEX A – MULTIPOINT FLUX APPROXIMATION-DIAMOND TYPE (MPFA-D) FINITE VOLUME METHOD	96
A.1	Solution of implicitly discretized pressure equation by the MPFA-D method	96
A.2	Treatment of boundary fluxes	99
A.3	Interpolating pressure on mesh nodes	100

1 INTRODUCTION

Over the past several years, the CFD research groups have been developing alternative formulations for different class of applications. One intensive research area is the development of high-order methods suitable for the simulation of multiple fluid phases in heterogeneous porous media.

These techniques are very useful in various aspects of petroleum reservoir engineering analysis, being used for helping decision-making in operations management. As it is well known, the computation difficulty of solving physics-mathematical models including fluid with nonlinear properties and large-scale heterogeneities in reservoir geology, with an accurate and stable numerical scheme is still a considerable challenge.

Commercial simulators in general uses structured mesh based formulations and are commonly used in the practice of reservoir engineering, despite of its limitations in terms of gridding choices. The mathematical model used in these simulators is a set of coupled PDEs (Partial Differential Equations).

As an alternative to the conventional coupled formulations, and under simplified assumptions, Peaceman (1977) proposes a robust nonlinear “segregated” model, in which the transport problem is solved using a hyperbolic equation, one for each phase, whereas the pressure field can be obtained by solving a scalar flux balance equation, which is of parabolic-elliptic type (SOUZA, 2015). The advantage of decoupling the system is the possibility of using appropriate methods to solve elliptic, parabolic and hyperbolic problems, which can be adapted to be applied to reservoir simulation (KOZDON; MALLISON; GERRITSEN, 2011; SOUZA, 2015).

In this work, we deal with the particular case of the two-phase immiscible, incompressible flow in reservoirs which can be modeled as decoupled PDEs that express conservation of mass and momentum for the two phases. The equations are nonlinear, time-dependent PDEs of elliptic nature for the pressure variable p and hyperbolic nature for the saturation S . The segregate solution procedure is the classical IMPES (IMplicit Pressure EXplicit Saturation).

In order to solve the pressure equation a MPFA-D (Multi-Point Flux Approximation-*Diamond* type) was employed. Initially the MPFA-D method was devised by Gao e Wu (2010) to solve the diffusion problems with applications to porous media. Recently this method was adapted by Contreras et al. (2016) to the solution of two-phase flows in petroleum reservoirs, in which the total mobility term on the control surface is computed as a function of the mobilities of the CVs that share at least a node with the surface.

To solve the Saturation equation a CPR (Correction Procedure via Reconstruction) scheme is employed to obtain stable, high-order accurate numerical solutions. The CPR method uses high-order shape functions for approximating numerical solutions. Shape functions are

usually chosen to be Lagrangian interpolants through Gauss-Lobatto-Legendre points.

In order to properly couple the MPFA-D method with the CPR formulation, it is necessary to obtain an adequate velocity reconstruction throughout the control volumes of the mesh. This is obtained by a reconstruction operator based on the Raviart-Thomas mixed finite-element method. This operator receives, as input, fluxes across element faces and returns the point-wise values of velocity anywhere within the cell.

1.1 Motivation

Commercial software for reservoir modeling and simulation, often based on TPFA schemes, low order approximations for the transport problem and the use of the structured grids (Cartesian and corner-point) have been an industry standard for years.

However, the low-order convergence of these commercial reservoir simulators and their difficulties in numerically modeling complex geological features of petroleum reservoirs, which may involve inclined layers, fractured media and fault zones are major drawbacks.

With the understanding of these limitations of classical numerical formulations, a practical solution is to add more resolution to overcome the problem. An alternative is by using high-order techniques due to their potential of delivering the required accuracy for flow problems with complex physics and geometry more efficiently.

Thus, this type of drawback is our initial motivation for considering the MPFA-D scheme coupled to CPR method via the IMPES formulation on unstructured grids, because of their many appealing features, to implement an academic simulator with strong stability properties and robustness to accurately resolve the physics of reservoir flows.

1.2 Objectives

This work aims to present the development and analysis the performance of a robust, stable high-order accurate numerical scheme to model two-phase immiscible, incompressible flow in reservoirs using structured or unstructured meshes. Our goal in this work is to demonstrate the effectiveness of the proposed methodology for the solution of a set of partial differential equations via an intelligent combination of the finite volume and the high-order methods with a compact stencil using a sequential approach. The flexibility of these methods that allows us to extract highly accurate solutions in various hypothetical what-if scenarios with geometric and geologic complexities in a simplified easy-to-use manner.

1.3 Contents

The rest of the document is organized as follow. The mathematical model, describing the incompressible/immiscible two-phase flow of oil and water in petroleum reservoirs is presented

in chapter 2. In chapter 3, we describe the numerical formulation of the IMPES, MPFA-D, CPR methods and some particular numerical issues, as also, we present some numerical experiments using the CPR to solve the generalized one-dimensional problems. In chapter 4, we show numerical results for several benchmark 2-D problems, including the analysis of the behavior of the reconstruction operator and in particular their ability to calculate the point-wise nodal velocity for bi-dimensional two-phase flow examples. In chapter 5, we draw some conclusions and discuss future works in the field. Finally, the MPFA-D method is discussed in annex A.

2 LITERATURE REVIEW

Specifically, this literature survey includes an overview of the literature on the MPFA methods to solve the pressure equation and with regard to the saturation equation the high-order methods, that form the subject of the present thesis are considered, namely DG (Discontinuous Galerkin), SV (Spectral Volume), SD (Spectral Difference) and the FR/CPR methods which are strongly related. Subsequently, the state of the art of the segregated formulation to deal with reservoir modeling themselves is discussed.

In the petroleum reservoir simulation community, the pattern is to approximate the elliptic term associated with the pressure equation by a simple TPFA (Two-Point Flux Approximation) method, despite its limitations to deal with full tensors and complex geometries.

A family of pressure solvers the MPFA schemes based on the work of Crumpton, Shaw and Ware (1995) have been proposed and show some promise (AAVATSMARK et al., 1998a; AAVATSMARK et al., 1998b; EDWARDS; ROGERS, 1998), to overcome the drawbacks of TPFA schemes and its generalization to deal with full tensors and arbitrary grids.

For many problems, a classical approach such as MPFA-O is appropriate (AAVATSMARK; EIGESTAD, 2006), but for some more complex situations, involving cases with strong anisotropy on arbitrary meshes, this is no longer true as spurious oscillatory solutions may be introduced and, thus, violate the DMP (Discrete Maximum Principle) (LEPOTIER, 2005; NORDBOTTEN; AAVATSMARK; EIGESTAD, 2007; LIPNIKOV et al., 2007; EDWARDS; ZHENG, 2008; CHEN et al., 2008; KUZMIN; SHASHKOV; SVYATSKIY, 2009).

The above discussion suggests that a new idea is required to use the MPFA method for problems with high anisotropic ratio and distorted grids. This new idea has been pursued by several authors in methods as the MPFA-FPS (Full Pressure Support) (EDWARDS; ZHENG, 2008), MPFA-Enriched (CHEN et al., 2008) and MPFA-Diamond (GAO; WU, 2010; CONTRERAS et al., 2016) which are examples of specific members of a much wider class of methods, all with a number of important properties, such as:

- Robustness.
- Reproducing piecewise linear solutions exactly by means of a linear preserving interpolation with explicit weights.
- Avoiding the solution of locally defined systems of equations.

An alternative non-linear approach is discussed in (LEPOTIER, 2005; LIPNIKOV et al., 2007). The advantage of the non-linear methods over MPFA schemes is a reduction of the oscillations, even to challenging modeling problems. It is, however, computationally more

expensive than the linear MPFA schemes, requiring an iterative positivity-preserving process (SOUZA, 2015).

With regard to the transport problem, as an alternative to the most straightforward approach, i.e., the Godunov method (GODUNOV, 1959), the MUSCL (Monotonic Upstream-Centered Scheme for Conservation Laws) method, which was originally proposed by Van Leer (1979) has been developed to obtain a second order approximation to solve the hyperbolic equations. It is very accurate and robust and it has been employed in several areas of knowledge, including physics, engineering and petroleum reservoir simulation (SPEKREIJSE, 1987; DURLOFSKY, 1993; BATTEN; LAMBERT; CAUSON, 1996; KIM; CHOI, 2000; DIAZ et al., 2009; DELIS; NIKOLOS, 2013; CONTRERAS et al., 2016).

During the last decades, a number of techniques for recovering a solution with a higher accuracy have been developed. Among these are the widely used ENO (HARTEN, 1983; HARTEN et al., 1987), weighted ENO (WENO) (HU; SHU, 1999), k -exact (BARTH; FREDERICKSON, 1990), and MOOD (CLAIN; DIOT; LOUBÈRE, 2011) methods, which are all techniques used in order to get very high-order spatial accuracy.

These schemes are at most second-order in regions of smooth solution and first-order close to shocks. However, as the reconstruction technique of these methods relies on using neighboring cells around the current cell for polynomial reconstruction at each time step, they were found to be very demanding on computer resources for resolution orders greater than two, which is due to the fact that in order to guarantee a k -exact reconstruction, a large local system of linear algebraic equations must be resolved, which depends on the order of the desired accuracy (COLELLA; WOODWARD, 1984; SOUZA, 2015; JALALI; GOOCH, 2017).

This also leads to losing some data locality as the large stencil extends far away from the current cell for higher-order accuracy on general unstructured grids, resulting in a series of difficulties for general implementation (HESTHAVEN; WARBURTON, 2008).

As an alternative, research in the applications of high-order methods has led to the development of formulations that use a type of local high-order reconstruction of the numerical solution that is discontinuous between neighboring cells, such as DG scheme, with applications to neutron transport (REED; HILL, 1973) and for numerically solving hyperbolic conservation laws (COCKBURN; SHU, 1989; COCKBURN; LIN; SHU, 1989; COCKBURN; HOU; SHU, 1990; COCKBURN; SHU, 2001), nodal DG, with applications to Maxwell equations (HESTHAVEN; WARBURTON, 2008), $P_N P_M$ procedure to solve the relativistic MHD (Magneto Hydro Dynamic) and Navier-Stokes equations (DUMBSER et al., 2008; DUMBSER; ZANOTTI, 2009; DUMBSER, 2010), RDG (Reconstructed Discontinuous Galerkin) method for the compressible Navier–Stokes equations (LUO et al., 2010; LUO et al., 2013) and in general for conservation laws, hybrid DG/FV method (ZHANG et al., 2012a; ZHANG et al., 2012b), Residual Distribution (RD) method (ABGRALL; MEZINE, 2003; RICCHIUTO; CSÍK; DECONINCK, 2005; ABGRALL, 2006; ABGRALL; LARAT; RICCHIUTO, 2011), SV method

(WANG, 2002; WANG; LIU, 2002; WANG; LIU, 2004; WANG; ZHANG; LIU, 2004) / SD (LIU; VINOKUR; WANG, 2006b; LIU; VINOKUR; WANG, 2006a; WANG et al., 2007; MAY; JAMESON, 2006), the SV scheme has been used to solve the shallow water equations by Choi et al. (2004).

On the other hand the FR (Flux Reconstruction) scheme (HUYNH, 2007) is a unifying framework that, depending on how the flux polynomial is defined, reproduce many existing high-order schemes, such as the DG, SD and SV with a nodal differential form. It is one of the most widely used in the CFD community, indeed the FR versions of DG, SV/SD are highly efficient (VINCENT; CASTONGUAY; JAMESON, 2011; LÓPEZ et al., 2014; WITHERDEN et al., 2015; ZHANG; LIANG; YANG, 2017).

The CPR is a numerical scheme developed quite recently for the solution of hyperbolic conservation laws on hybrid unstructured meshes and it consists on the merging of the FR and LCP (Lifting Collocation Penalty) (WANG; GAO, 2009) schemes into a common framework. In the CPR formulation, correction functions are used to correct the discontinuous flux function within an element in order to ensure flux continuity across element interfaces. Due to its potential of delivering higher accuracy with lower computational cost, the CPR scheme is believed to be among the most efficient discontinuous methods in terms of the number of operations count (WANG; GAO; HAGA, 2011; ZIMMERMAN; WANG, 2013; YU; WANG; LIU, 2014).

To follow, a review of state of art of high-order methods and its applications in petroleum engineering is carried out.

TPFA schemes coupled with low-order methods have been used traditionally in the petroleum reservoir community during the last five decades (PEACEMAN, 1977; EWING, 1983; EDWARDS; ROGERS, 1998; ARNOLD et al., 2002; EYMARD; GUICHARD; MASSON, 2012). This approach naturally works very well, i.e., it is simple to implement and highly computationally efficient but its main disadvantage lies in the inability to deal with complex geometries and the excessive spreading of the saturation profiles, besides the extreme sensitivity to grid orientation effect. In order to mitigate those drawbacks, several combinations of sequential approaches have been developed, as will be discussed below.

For the elliptic problem, there are several options for the pressure solver, although the MFE (Mixed Finite Element) approach is one of the most popular. By using the locally mass conservative MFE method, both pressure and velocity can be solved simultaneously from the Darcy system, with the same order of accuracy. The transport problem is solved subsequently using traditional methods as: Shock capturing methods (EWING, 1984; CHAVENT; JAFFRÉ, 1986), DG method (BASTIAN, 1999; RIVIERE, 2000; RIVIÈRE; WHEELER, 2002; BASTIAN, 2003; SUN; WHEELER, 2005; HOTEIT; FIROOZABADI et al., 2006; ERN et al., 2009; BASTIAN, 2014; LI; RIVIERE, 2015b). DG methods also have been used to solve both the pressure and the saturation equations (RIVIERE, 2008; LI; RIVIERE, 2015a; TANEJA; HIGDON, 2018).

The use of MFE methods coupled with FV methods has been discussed extensively in (AARNES; GIMSE; LIE, 2007; MURAD et al., 2013a; MURAD et al., 2013b) and references therein, highlighting the potential of such techniques to the simulation of multiphase flow in porous media.

In addition, some high-order schemes were implemented and tested for second-order accuracy using a MUSCL reconstruction including a limiting procedure to get a TVD (Total Variation Diminishing) scheme together with techniques to solve the elliptic equation, such as: MFE scheme (DURLOFSKY, 1993), EBFV (Edge-Based Finite Volume) method (CARVALHO, 2005) and CVD (Control-Volume Distributed) (EDWARDS, 2006), etc. Other schemes were applied to petroleum reservoir simulation, include the Mass-Weighted Upwind Scheme (MWU), the Streamline-Based Upwind Scheme, and a TVD-scheme which uses second order interpolation functions (FERNANDES; MARCONDES; SEPEHRNOORI, 2013; FERNANDES et al., 2015).

On the other hand, applications to two-phase flow modeling by using classical MPFA schemes coupled with higher order upwind or central schemes have been conducted by Lamine e Edwards (2010), Edwards (2010). Recently, a non-orthodox MPFA-D method was employed together with a high-order finite volume method to the simulation of oil–water displacements in heterogeneous and anisotropic petroleum reservoirs (CONTRERAS; LYRA et al., 2012; CONTRERAS et al., 2016).

With respect to the SV approach, it was explored in a preliminary study to the one-dimensional applications of oil and water displacements in petroleum reservoirs by Galindez (2014), Galindez-Ramirez et al. (2017), where the total velocity was assumed to be constant.

In this context, in the present work, for the first time, we use a novel methodology to solve two-phase flow problems in petroleum reservoirs simulation via a classical IMPES approach. In this technique, the pressure equation is computed by using a non-orthodox MPFA-D finite volume scheme and the saturation equation is solved via the high-order CPR method.

3 MATHEMATICAL MODEL

In this chapter we give an overview of the mathematical model adopted throughout the text, including a brief description of important variable names.

3.1 Governing equations

This model consist of a set of partial differential equations obtained using the mass conservation law, Darcy law, and some other considerations, such as

- Immiscible and incompressible flow
- Fully saturated non deformable rock
- Thermal and chemical terms neglected
- Neglecting dispersion and adsorption effects
- Darcian flow

Then the flow of two immiscible phases α , classically, oil and water (o, w), through porous formations can be described in terms of the continuity equation, as

$$\frac{\partial (\phi \rho_{\alpha} S_{\alpha})}{\partial t} = -\vec{\nabla} \cdot (\rho_{\alpha} \vec{v}_{\alpha}) + q_{\alpha} \quad (3.1)$$

which formally establishes that mass is conserved. In the previous equation, the term q_{α} models sources and sinks of phase α , ϕ is the rock porosity distribution, which may be considered constant in time, S_{α} and ρ_{α} denote the saturation and density of phase α , respectively. With respect to the phase velocity \vec{v}_{α} a generalized form of Darcy's law is adopted (HELMIG, 1997). It gives a relationship between the flow rate and the pressure gradient during laminar flow in porous media, as shown in the following equation

$$\vec{v}_{\alpha} = -\lambda_{\alpha} \tilde{K} (\nabla p_{\alpha} - \rho_{\alpha} \vec{g}) \quad (3.2)$$

in which λ_{α} é a mobilidade da fase α , \tilde{K} is the absolute permeability tensor of a particular reservoir rock, \vec{g} is the gravity acceleration vector. The permeability tensor considered here is solely a function of the position in the porous medium, and it represents a simple measurement of the ability of the rock to allow fluids to pass through it. The pressure of fluid-phase α is given by p_{α} and μ_{α} , $k_{r\alpha}(S_{\alpha})$ are the viscosity and relative permeability of phase α , respectively.

For further details about the required assumptions for Darcy's law to be valid see, for instance, Helmig (1997). Now, we can deduce the segregate formulation by algebraic manipulation of the basic equations in order to obtain a pressure equation (elliptic-parabolic) without explicit

saturation terms and a saturation equation (hyperbolic-parabolic) without explicit pressure terms (PEACEMAN, 1977; CARVALHO, 2005; CONTRERAS et al., 2016). To derive the pressure equation, the time derivative given in Eq. (3.1) is expanded and rewritten for each phase as shown follows

$$\frac{\phi S_o \partial(\rho_o)}{\partial t} + \frac{\rho_o S_o \partial(\phi)}{\partial t} + \frac{\phi \rho_o \partial(S_o)}{\partial t} = -\vec{\nabla} \cdot (\rho_o \vec{v}_o) + q_o \quad (3.3)$$

and

$$\frac{\phi S_w \partial(\rho_w)}{\partial t} + \frac{\rho_w S_w \partial(\phi)}{\partial t} + \frac{\phi \rho_w \partial(S_w)}{\partial t} = -\vec{\nabla} \cdot (\rho_w \vec{v}_w) + q_w \quad (3.4)$$

The first two terms on the RHS (Right-Hand-Side) of Eqs. (3.3) and (3.4) vanish under the consideration of incompressible fluid/rock system. Now dividing the above equations by ρ_o and ρ_w , respectively, we obtain

$$\phi \frac{\partial(S_o)}{\partial t} = -\vec{\nabla} \cdot (\vec{v}_o) + Q_o \quad (3.5)$$

and

$$\phi \frac{\partial(S_w)}{\partial t} = -\vec{\nabla} \cdot (\vec{v}_w) + Q_w \quad (3.6)$$

with $Q_\alpha = q_\alpha / \rho_\alpha$, is the total fluid injection or production specific rate. By adding Eqs. (3.5) and (3.6) one obtains

$$\phi \frac{\partial(S_o + S_w)}{\partial t} = -\vec{\nabla} \cdot (\vec{v}_o + \vec{v}_w) + Q_o + Q_w \quad (3.7)$$

Now, considering that the rock is completely saturated by the two coexisting liquid phases, a constraint for the saturation is given by $S_w + S_o = 1$, thus, the LHS (Left-Hand-Side) of Eq. (3.7) vanishes and it can be rewritten as

$$\vec{\nabla} \cdot \vec{v} = Q \quad (3.8)$$

with

$$\vec{v} = -\lambda \tilde{K} (\nabla p - \rho \vec{g}) \quad (3.9)$$

where, the total mobility is defined as, $\lambda = \lambda_w + \lambda_o$, in which $\lambda_\alpha = k_{r\alpha} / \mu_\alpha$ is fluid α mobility. It states that the velocity is proportional to the pressure gradient. Equation (3.8) is an elliptic pressure equation, where $\vec{v} = \vec{v}_o + \vec{v}_w$ is the total fluid velocity and $Q = Q_w + Q_o$. It is interesting to notice that in the pressure equation (3.8) the saturation S_α is not explicitly present. On the other hand in order to derive the saturation equation, Darcy's law, Eq. (3.2), is written for each phase, in the following form

$$\vec{v}_w = -\lambda_w \tilde{K} (\nabla p_w - \rho_w \vec{g}) \quad (3.10)$$

$$\vec{v}_o = -\lambda_o \tilde{K} (\nabla p_o - \rho_o \vec{g}) \quad (3.11)$$

Thereafter, multiplying the above equations by the mobilities λ_o and λ_w , respectively, gives

$$\lambda_o \vec{v}_w = -\lambda_w \lambda_o \tilde{K} (\nabla p_w - \rho_w \vec{g}) \quad (3.12)$$

$$\lambda_w \vec{v}_o = -\lambda_o \lambda_w K (\nabla p_o - \rho_o \vec{g}) \quad (3.13)$$

Then, subtracting one equation from the other yields

$$\lambda_w \vec{v}_o - \lambda_o \vec{v}_w = -\lambda_o \lambda_w K (\nabla p_o - \rho_o \vec{g} - \nabla p_w + \rho_w \vec{g}) \quad (3.14)$$

Multiplying the previous equation by (-1) and taking of gradient of capillary pressure, i.e., $\nabla p_c = \nabla(p_o - p_w)$, then, one can rearrange the above equation, such as

$$\lambda_o \vec{v}_w - \lambda_w \vec{v}_o = \lambda_o \lambda_w K \nabla p_c - \lambda_o \lambda_w K (\rho_o - \rho_w) \vec{g} \quad (3.15)$$

Rearranging the terms in Eq. (3.15) and using the fact that $\vec{v}_o = \vec{v} - \vec{v}_w$ and the total mobility $\lambda = \lambda_o + \lambda_w$, we can write

$$\vec{v}_w = f_w [\vec{v} - \lambda_o K (\rho_o - \rho_w) \vec{g}] + \lambda_o f_w K \nabla p_c \quad (3.16)$$

where the fractional flow of water is defined as

$$f_w = \frac{\vec{v}_w \cdot \vec{N}}{\vec{v} \cdot \vec{N}} = \left(\frac{1}{1 + \frac{\lambda_o}{\lambda_w}} \right) \left\{ 1 + \frac{\lambda_o K}{\vec{v} \cdot \vec{N}} [\nabla p_c - \Delta \rho \vec{g}] \cdot \vec{N} \right\} \quad (3.17)$$

in the above equation, \vec{N} is the surface area normal vector and $\Delta \rho = \rho_o - \rho_w$. For the case of horizontal flow, with negligible gravitational and capillary pressure effects, Eq. (3.17) becomes (FANCHI, 2005)

$$f_w = \frac{\lambda_w}{\lambda} = \frac{1}{1 + \frac{\lambda_o}{\lambda_w}} \quad (3.18)$$

Finally, the water-phase saturation equation is obtained by substituting Eq. (3.16) into Eq. (3.6), as shown in the following equation

$$\phi \frac{\partial S_w}{\partial t} = -\nabla \cdot \left(f_w [\vec{v} - \lambda_o K \Delta \rho \vec{g}] + \lambda_o f_w K \nabla p_c \right) + Q_w \quad (3.19)$$

It is worthwhile to mention that Eq. (3.8) is linked to the water-phase saturation equation (3.19) via Darcy's equation (3.9) for the total velocity.

For the one-dimensional case, we can write Eq. (3.19) as

$$\phi \frac{\partial S_w}{\partial t} = -\frac{\partial}{\partial x} (F_{\text{adv}} + F_{\text{diff}}) + Q_w \quad (3.20)$$

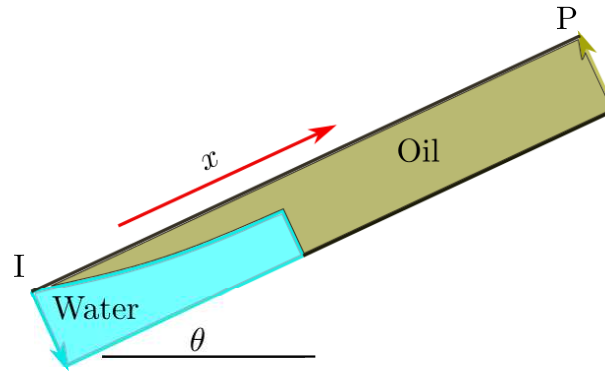
in which the advective flux is given by

$$F_{\text{adv}} = f_w [v - \lambda_o K \Delta \rho g \sin \theta] \quad (3.21)$$

where θ is the dip angle, i.e., the angle between direction x and horizontal, see Fig. 1.

The diffusive flux is defined as

$$F_{\text{diff}} = \mathcal{D} \frac{\partial S_w}{\partial x} \quad (3.22)$$

Figure 1 – Reservoir model, illustrating the displacement of oil by water in a system of dip angle θ .

Source: The author (2018).

where $\mathcal{D} = \lambda_o f_w K \frac{dp_c}{dS_w}$ which is a function of the water saturation S_w . In the present work we employ the standard practice in the petroleum industry, then we use two main models to describe the fluid properties, i.e., the (BROOKS; COREY, 1964) and Van Genuchten (1980) models, which are given by the following constitutive relations as described in (HELMIG, 1997)

Brooks-Corey

$$\begin{aligned} k_{rw}(S_w) &= S_e^\beta \\ k_{ro}(S_w) &= 1 - S_e^\gamma \end{aligned} \quad (3.23)$$

Van Genuchten

$$\begin{aligned} k_{rw}(S_w) &= S_e^{1/\zeta} \left(1 - \left[1 - S_e^{1/\zeta} \right]^\zeta \right)^2 \\ k_{ro}(S_w) &= (1 - (1 - S_e))^{1/2} \left(1 - (1 - S_e)^{1/\zeta} \right)^{2\zeta} \end{aligned} \quad (3.24)$$

with parameters β , γ , ζ and the effective saturation S_e is given by

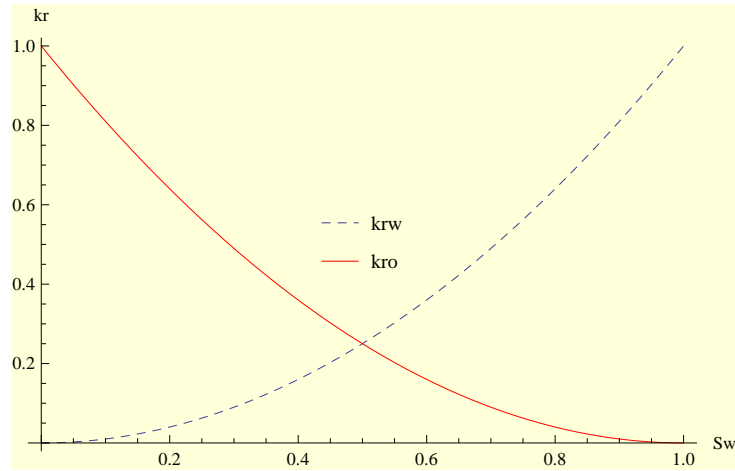
$$S_e = \frac{S_w - S_{wr}}{1 - S_{wr} - S_{or}} \quad (3.25)$$

where S_{wr} and S_{or} are residual water and oil saturations, respectively. In Fig. 2 are depicted the water and oil quadratic relative permeabilities, with $\beta = \gamma = 2$ which are assumed to be a function of water saturation.

3.1.1 Initial and boundary conditions

To guarantee a well-posed problem, which gives unique solutions, appropriate initial and boundary conditions must be provided (AZIZ; SETTARI, 1979; SOUZA, 2015). In what follows, the treatment of boundary conditions for the pressure equation (3.8) is presented. The

Figure 2 – Relative permeability functions for water-oil phases.



Source: The author (2018).

external boundary conditions can be written as

$$\begin{aligned} p(\vec{r}, t) &= g_D \text{ on } \Gamma_D \times [0, t] \\ \vec{v} \cdot \vec{n} &= g_N \text{ on } \Gamma_N \times [0, t] \end{aligned} \quad (3.26)$$

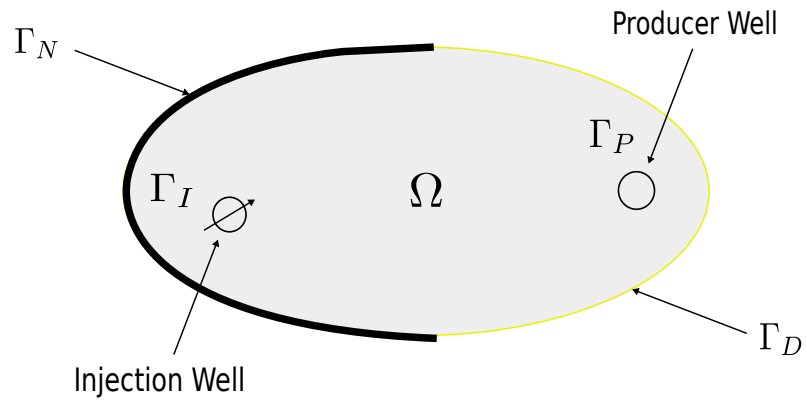
In the above equations, the prescribed pressure g_D and flux g_N are defined on Dirichlet Γ_D and Neumann Γ_N boundaries, respectively. On the other hand, the set of injection and production wells can be expressed as internal boundaries, such as, Γ_I and Γ_P , with prescribe pressure g_I and/or flux g_P , respectively as given by

$$\begin{aligned} p(\vec{r}, t) &= g_I \text{ on } \Gamma_I \times [0, t] \\ \vec{v} \cdot \vec{n} &= g_P \text{ on } \Gamma_P \times [0, t] \end{aligned} \quad (3.27)$$

see Fig. 3 for a sketch of the external and internal boundaries. Now, the classical initial and boundary conditions for saturation equation can be written as

$$\begin{aligned} S_w(\vec{r}, t) &= \bar{S}_w \text{ on } \Gamma_I \times [0, t] \text{ or } \Gamma_D \times [0, t] \\ S_w(\vec{r}, t) &= \bar{S}_w^0 \text{ on } \Omega \times t^0 \end{aligned} \quad (3.28)$$

Here, the prescribed water saturation in the injection wells is denoted by \bar{S}_w , and \bar{S}_w^0 is the initial water saturation distribution in all domain Ω for $t = t_0$.

Figure 3 – External and internal boundaries in Ω domain.

Source: The author (2018).

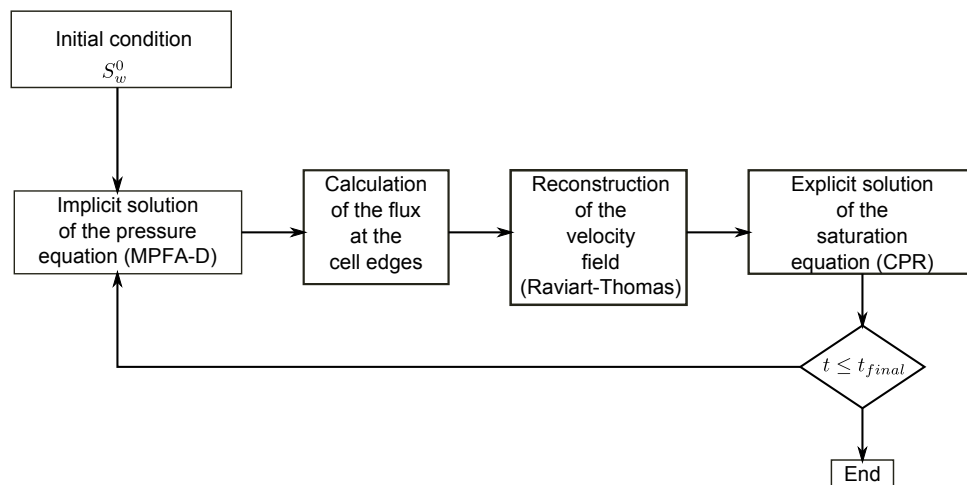
4 NUMERICAL FORMULATION

A set of key issues related to the physics of the phenomena, such as a highly heterogeneous and anisotropic porous media, non-convex advective flux function, as well as, the non-linearity of saturation equation and its coupling to the pressure equation, constitute relevant numerical challenges (GERRITSEN; DURLOFSKY, 2005; CHEN; HUAN; MA, 2006; SOUZA, 2015). In order to face these challenges, in this chapter, the numerical formulations to solve the pressure and saturation equations are presented, in addition to their direct coupling via an IMPES (Implicit Pressure-Explicit Saturation) scheme.

4.1 Pressure/Velocity solver

The IMPES strategy proposed by Sheldon, Jr et al. (1959) and by Stone and Garder (1961) is very popular in reservoir simulation community, partly because of being a simple but robust technique, to model incompressible flows (CARVALHO, 2005; CHEN; HUAN; MA, 2006; SOUZA, 2015; CONTRERAS et al., 2016). In the IMPES scheme, the total mobility $\lambda(S_w)$ is computed for a control surface, from the initial water saturation in the previous time level. Then, the pressure equation (3.8) is solved implicitly. The velocity field is computed using the Darcy law Eq. (3.9), the saturation equation (3.19) is solved explicitly, at each time step, computed according to the CFL (Courant–Friedrichs–Lewy) condition to maintain stability. To get a better understanding of the IMPES methodology, its algorithm is shown in Fig. 4. This method is easy to implement and efficient to solve and requires less memory than other methods such as that which uses a monolithic model, requiring a simultaneous solution of the pressure and saturation fields.

Figure 4 – IMPES methodology algorithm.



Source: The author (2018).

Coupling the MPFA (Multi-Point Flux Approximation) type-schemes with higher order spectral/nodal approximations is still a challenge. This is due to the fact that cell-centered finite-volumes-type discretization methods, that solve the pressure equation, classically calculate fluxes across cell faces that belong to the primal grid, but does not give information on point-wise values of velocity within a grid element (SRINIVASAN; LIPNIKOV, 2013). In order to get the complete knowledge of velocity field throughout the domain, a reconstruction operator based on the Raviart-Thomas finite-element shape function can be built. The reconstruction operator receives as input the flux across element edges, and returns the point-wise values of velocity anywhere in the cell (RAVIART; THOMAS, 1977; SRINIVASAN; LIPNIKOV, 2013). Using the reconstruction operator, the coupling via IMPES of the MPFA-type methods with spectral/nodal formulations, such as, SV/SD and CPR is possible. This issue will be further discussed in section 4.1.2.

4.1.1 MPFA-D Method

In order to solve the pressure equation for unstructured grids with anisotropic and heterogeneous permeability, a MPFA-D (Multi-Point Flux Approximation), with a *Diamond* like stencil, method is adopted. The MPFA-D scheme, which uses multiple points to approximate the flux at the interface between neighboring cells, was proposed by Gao e Wu (2010), to solve diffusion-type problems for anisotropic and heterogeneous media.

Recently this methodology was applied to petroleum reservoirs simulation by Contreras et al. (2016). The MPFA-D is a completely cell-center formulation, which requires the values of pressure for each vertex, at the two edge's endpoints, that are obtained using a linear weighted combination of the pressure values in the center of the surrounding cells. In order to solve the pressure equation (3.8), we discretize the domain Ω , with boundary Γ , into a \mathcal{N} non-overlapping polygonal CVs (control volumes), denoted as Ω_i . Now by integrating Eq. (3.8) over Ω_i and applying the Gauss Divergence theorem, we have

$$\int_{\Gamma_i} \vec{v} \cdot \vec{n} dA = \int_{\Omega_i} Q \partial \Omega_i \quad (4.1)$$

where, \vec{n} is the unit normal vector, which points outward of the control surface Γ_i . Under some assumptions, the left and right hand sides of previous equation can be written as (CONTRERAS et al., 2016)

$$\int_{\Gamma_i} \vec{v} \cdot \vec{n} \partial \Gamma_i = \sum_{IJ \in \Gamma_i} \vec{v}_{IJ} \cdot \vec{N}_{IJ} \quad (4.2)$$

and

$$\int_{\Omega_i} Q \partial \Omega_i = \bar{Q}_i V_i \quad (4.3)$$

here, \vec{N}_{IJ} is surface area (length in 2D) normal vector to face \vec{IJ} and V_i is the volume (area in 2D) of the primal CV Ω_i . In the previous equations, we can define the average mid-edge velocity, as

$$\vec{v}_{IJ} = \frac{1}{|\vec{N}_{IJ}|} \int_{\Gamma} \vec{v} \partial \Gamma \quad (4.4)$$

and, the injection/production average terms, in the following manner

$$\bar{Q}_i = \frac{1}{V_i} \int_{\Omega_i} Q \partial \Omega_i \quad (4.5)$$

For calculation of the approximated pressure and velocities, the formulation proposed by Gao e Wu (2010) was used in this work. For additional information please see, Annex A, Contreras et al. (2016), and references therein. Finally, after algebraic and geometric manipulation, the density flux through the control surface can be compactly expressed as

$$F_{IJ} = \vec{v}_{IJ} \cdot \vec{N}_{IJ} \cong \tau_{IJ} [p_{\hat{R}} - p_{\hat{L}} - v_{IJ}(p_J - p_I)] \quad (4.6)$$

where, τ_{IJ} is the scalar transmissibility, given by

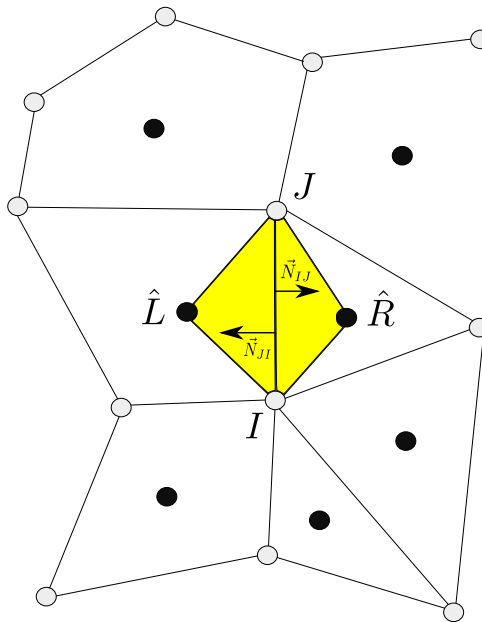
$$\tau_{IJ} = -\lambda_{IJ} \frac{K_{IJ_{\hat{L}}}^{(n)} K_{IJ_{\hat{R}}}^{(n)}}{K_{IJ_{\hat{L}}}^{(n)} h_{IJ}^{\hat{R}} + K_{IJ_{\hat{R}}}^{(n)} h_{IJ}^{\hat{L}}} |\vec{IJ}| \quad (4.7)$$

and v_{IJ} is a non-dimensional tangential parameter, which can be written as

$$v_{IJ} = \frac{\vec{IJ} \cdot \vec{\hat{L}\hat{R}}}{|\vec{IJ}|^2} - \frac{1}{|\vec{IJ}|} \left(\frac{K_{IJ_{\hat{L}}}^{(t)} h_{IJ}^{\hat{L}}}{K_{IJ_{\hat{L}}}^{(n)}} + \frac{K_{IJ_{\hat{R}}}^{(t)} h_{IJ}^{\hat{R}}}{K_{IJ_{\hat{R}}}^{(n)}} \right) \quad (4.8)$$

In Eq. (4.6), the pressures p are located in the polygonal mesh according to Fig. 5. As already said, the nodal pressures, p_I and p_J are computed using the pressure values of the CVs surrounding nodes I and J , respectively, via a LPEW (Linearity-Preserving Explicit Weighted) interpolation. For further discussion and many more details on the MPFA-D method, we refer to annex A.

Figure 5 – Part of a polygonal mesh, illustrating the diamond path.



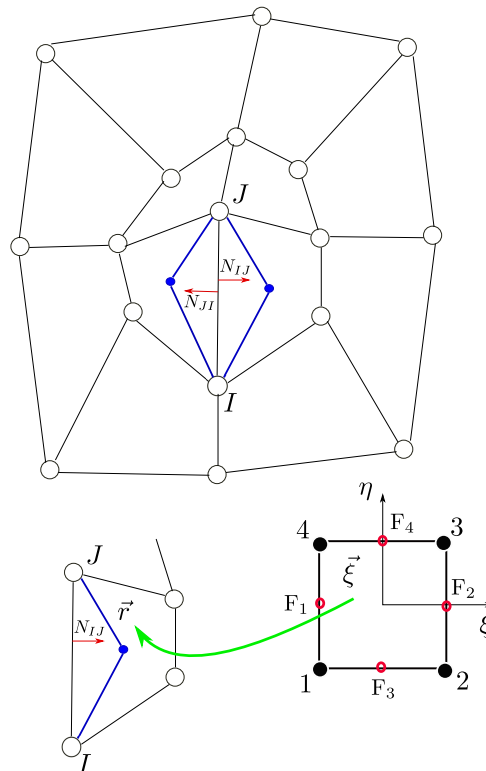
Source: Adapted from Contreras et al. (2016).

4.1.2 Reconstruction of Darcy velocity inside the CV of a quadrilateral mesh

By considering the MPFA-D discretization of the pressure field which is piecewise constant over an element of the primal grid, we can use a velocity space, namely, the lowest order Raviart-Thomas H-Div space RT_0 , that is adequate for this type of the pressure approximation (MATRINGE; JUANES; TCHELEPI, 2006). In this work, via the lowest-order Raviart-Thomas space, the point-wise velocity field inside the elements mesh is approximated using uniquely the mid-edge fluxes F_i , Eq. (4.6), through a CS (Control Surface) \vec{IJ} (RAVIART; THOMAS, 1977). Thus, the velocity field can be defined by a vector function, which receives as input an array of fluxes $[F_1, \dots, F_4]$ and returns the point-wise value velocity at any location of the current element Ω .

To obtain the full velocity field in physical domain, we need to reconstruct the velocity into a reference domain using the Raviart-Thomas space, which is based on a linear interpolation of the flux through the faces of the primal grid cells. Fig. 6 illustrates the RT_0 in the \mathbb{P} (physical) and \mathbb{R} (reference) domain.

Figure 6 – Part of a quadrilateral mesh, illustrating the RT_0 velocity interpolation.



Source: The author (2018).

The velocity interpolation using Raviart-Thomas velocity field $H(\text{div}, \Omega_i)$ can be written

as (MATRINGE; JUANES; TCHELEPI, 2006; HÆGLAND et al., 2007)

$$\vec{v}_{\mathbb{R}}(\vec{\xi}) = \begin{bmatrix} -\frac{F_1}{4}(1-\xi) + \frac{F_2}{4}(1+\xi) \\ -\frac{F_3}{4}(1-\eta) + \frac{F_4}{4}(1+\eta) \end{bmatrix} \quad (4.9)$$

on standard bi-linear quadrilateral $\{\vec{\xi} = (\xi, \eta) | -1 \leq (\xi, \eta) \leq 1\}$. By using an adequate bi-linear isoparametric mapping, where each grid element is usually mapped into a unit square in the reference domain, we have

$$\vec{r} = \varphi(\vec{\xi}) = \sum_{i=1}^{n_{\text{nodes}}} \psi_i(\vec{\xi}) \vec{r}_i \quad (4.10)$$

in which, $\psi_i(\vec{\xi})$ are the standard bi-linear shape functions on the unit square, that can be written as

$$\begin{aligned} \psi_1(\xi, \eta) &= 0.25(1-\xi)(1-\eta) & \psi_2(\xi, \eta) &= 0.25(1+\xi)(1-\eta) \\ \psi_3(\xi, \eta) &= 0.25(1+\xi)(1+\eta) & \psi_4(\xi, \eta) &= 0.25(1-\xi)(1+\eta) \end{aligned} \quad (4.11)$$

and explicitly we have

$$\begin{aligned} \vec{r} = \varphi(\vec{\xi}) &= 0.25(1-\xi)(1-\eta) \begin{bmatrix} x_1 \\ y_1 \end{bmatrix} + 0.25(1+\xi)(1-\eta) \begin{bmatrix} x_2 \\ y_2 \end{bmatrix} \\ &+ 0.25(1+\xi)(1+\eta) \begin{bmatrix} x_3 \\ y_3 \end{bmatrix} + 0.25(1-\xi)(1+\eta) \begin{bmatrix} x_4 \\ y_4 \end{bmatrix} \end{aligned} \quad (4.12)$$

that is

$$\begin{aligned} x(\xi, \eta) &= 0.25(1-\xi)(1-\eta)x_1 + 0.25(1+\xi)(1-\eta)x_2 \\ &+ 0.25(1+\xi)(1+\eta)x_3 + 0.25(1-\xi)(1+\eta)x_4 \end{aligned} \quad (4.13)$$

$$\begin{aligned} y(\xi, \eta) &= 0.25(1-\xi)(1-\eta)y_1 + 0.25(1+\xi)(1-\eta)y_2 \\ &+ 0.25(1+\xi)(1+\eta)y_3 + 0.25(1-\xi)(1+\eta)y_4 \end{aligned} \quad (4.14)$$

Finally, the velocity field from reference domain can be mapped back to physical domain, via the Piola transformation, as follows

$$\vec{v}_{\mathbb{P}}(\vec{r}) = \mathcal{P}(\vec{\xi}) \vec{v}_{\mathbb{R}}(\vec{\xi}) = \frac{1}{\det(\mathcal{J}(\vec{\xi}))} \mathcal{J}(\vec{\xi}) \vec{v}_{\mathbb{R}}(\vec{\xi}) \quad (4.15)$$

in such a way that the flux is preserved, that is, the flux across the cell interfaces in the reference and physical domain is the same. In Eq. (4.15), $\mathcal{J}(\vec{\xi})$ is the jacobian matrix of the transformation, which is given by

$$\mathcal{J} = \frac{\partial \vec{r}}{\partial \vec{\xi}} = \begin{pmatrix} \frac{\partial x}{\partial \xi} & \frac{\partial x}{\partial \eta} \\ \frac{\partial y}{\partial \xi} & \frac{\partial y}{\partial \eta} \end{pmatrix} \quad (4.16)$$

with

$$\begin{aligned}
 \frac{\partial x}{\partial \xi} &= 0.25(x_2 - x_1)(1 - \eta) + 0.25(x_3 - x_4)(1 + \eta) \\
 \frac{\partial x}{\partial \eta} &= 0.25(x_4 - x_1)(1 - \xi) + 0.25(x_3 - x_2)(1 + \xi) \\
 \frac{\partial y}{\partial \xi} &= 0.25(y_2 - y_1)(1 - \eta) + 0.25(y_3 - y_4)(1 + \eta) \\
 \frac{\partial y}{\partial \eta} &= 0.25(y_4 - y_1)(1 - \xi) + 0.25(y_3 - y_2)(1 + \xi)
 \end{aligned}
 \tag{4.17}$$

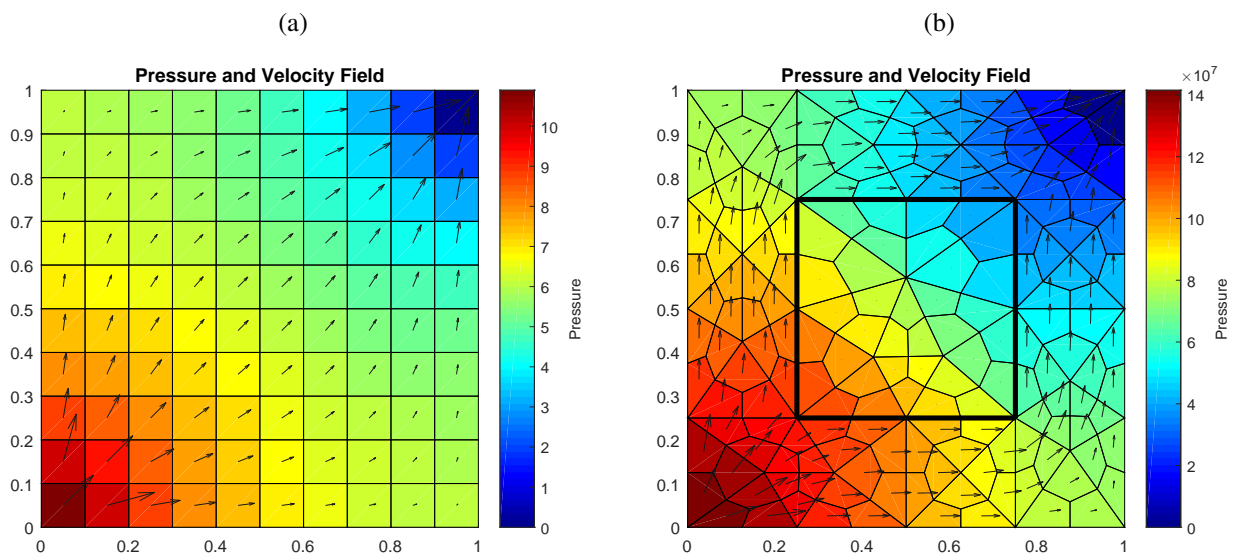
In Fig. 7 are depicted the MPFA-D pressure field and RT_0 velocity reconstruction. Here, we see a velocity field corresponding to a physical situation for a incompressible flow in an isotropic porous medium with sources/sinks (Injection and production wells), for the homogeneous case Fig. 7(a) and for a heterogeneous case, in which, the flow correctly avoids the low permeability central zone, see Fig. 7(b). In these figures the velocities were reconstructed in the collocation points (centroids) of the CVs.

4.2 Saturation/Transport solver

4.2.1 CPR method

Huynh (2007) introduce a quite new differential formulation to deal with hyperbolic equations/transport problem in nodal differential form. The scheme is called FR (Flux Reconstruction) and by using certain types of correction functions the method does indeed recover simplified versions of known schemes, such as DG, SV and SD. The FR method was originally formulated

Figure 7 – MPFA-D Pressure field and RT_0 velocity reconstruction for quadrangular grids (a) Homogeneous quarter of five spot configuration and (b) Heterogeneous quarter of five spot configuration.



Source: The author (2018).

for quadrilateral elements, subsequently, Wang e Gao (2009) extended this new methodology for triangular meshes, with the LCP (Lifting collocation penalty) framework. Finally, the names of FR and LCP are combined as CPR (Correction Procedure via Reconstruction) method (WANG; GAO; HAGA, 2011). This method is shown to be very simple and efficient, and from a practical viewpoint its implementation is relatively easy and of low computational cost. To illustrate this the governing equation will be transformed to an efficient numerical differential scheme via the CPR approach, as will be shown below under certain assumptions.

Consider the following model of immiscible flow (water and oil) on a set $\Omega \subseteq \mathbb{R}^n$ with imposition of appropriated boundary conditions on $\partial\Omega$, the water saturation Eq. (3.19), in the absence of source terms and setting $\phi = 1$ without loss of generality can be written as

$$\frac{\partial S_w}{\partial t} + \vec{\nabla} \cdot \vec{F}_w(S_w) = 0 \quad (4.18)$$

By multiplying Eq. (4.18) by the test function W and integrating over the domain Ω , we have the weighting residual form:

$$\int_{\Omega} W \left(\frac{\partial S_w}{\partial t} + \vec{\nabla} \cdot \vec{F}_w(S_w) \right) dV = 0 \quad (4.19)$$

We assume that the domain is divided into, \mathcal{N} , of non-overlapping cells Ω_i such that $\cup_{i=1}^{\mathcal{N}} \Omega_i = \Omega$. Then the solution S_w is approximated by $S_i^{P_n}$, where we have dropped the element index w for simplicity. Here, P_n is the polynomial-space of degree less than or equal to n . The dimension of P_n is $\mathcal{D} = (n+1)^2$ for quadrilateral cells. Now integrating by parts and applying the Gauss Divergence theorem to Eq. (4.19) yields the weak form of Eq. (4.18) on the cell Ω_i

$$\int_{\Omega_i} W \left(\frac{\partial S_w}{\partial t} + \vec{\nabla} \cdot \vec{F}_w(S_w) \right) dV = \int_{\Omega_i} W \frac{\partial S_i^{P_n}}{\partial t} dV + \int_{\partial\Omega_i} W \vec{F}_w(S_i^{P_n}) \cdot \vec{N} dA - \int_{\Omega_i} \vec{\nabla} W \cdot \vec{F}_w(S_i^{P_n}) dV = 0 \quad (4.20)$$

where, dA is the boundary surface differential area and W is a weighting function. To account for the data interaction across cell interfaces and to give cell coupling, the normal flux term in the surface integral of Eq. (4.20) shall be replaced with the approximated Riemann solver flux

$$\vec{F}_w(S_i^{P_n}) \cdot \vec{N} \approx \mathcal{F} \left(S_i^{P_n}, S_{(i+1)}^{P_n}, \vec{N} \right) \quad (4.21)$$

where $S_{(i+1)}^{P_n}$ is the neighboring solution at the interface of the current cell Ω_i . The previous expression can now be used to rewrite Eq. (4.20) as

$$\int_{\Omega_i} W \frac{\partial S_i^{P_n}}{\partial t} dV + \int_{\partial\Omega_i} W \mathcal{F} (S_i^{P_n}, S_{(i+1)}^{P_n}, \vec{N}) dA - \int_{\Omega_i} \vec{\nabla} W \cdot \vec{F}_w(S_i^{P_n}) dV = 0 \quad (4.22)$$

One more time, by applying integration by parts and the Gauss Divergence theorem to the last term of Eq. (4.22) gives

$$\int_{\Omega_i} W \frac{\partial S_i^{P_n}}{\partial t} dV + \int_{\partial\Omega_i} W \mathcal{F} (S_i^{P_n}, S_{(i+1)}^{P_n}, \vec{N}) dA - \int_{\partial\Omega_i} W \vec{F}_w(S_i^{P_n}) \cdot \vec{N} dA + \int_{\Omega_i} W \vec{\nabla} \cdot \vec{F}_w(S_i^{P_n}) dV = 0 \quad (4.23)$$

Rearranging the above expression becomes

$$\int_{\Omega_i} W \frac{\partial S_i^{P_n}}{\partial t} dV + \int_{\partial\Omega_i} W \left[\mathcal{F} \left(S_i^{P_n}, S_{(i+1)}^{P_n}, \vec{N} \right) - \vec{F}_w(S_i^{P_n}) \cdot \vec{n} \right] dA + \int_{\Omega_i} W \vec{\nabla} \cdot \vec{F}_w(S_i^{P_n}) dV = 0 \quad (4.24)$$

where $\vec{F}_w(S_i^{P_n}) \cdot \vec{N}$ is the normal flux based on the current solution $S_i^{P_n}$ at the boundary of the cell. The previous equation can be rewrite as

$$\int_{\Omega_i} W \left(\frac{\partial S_i^{P_n}}{\partial t} + \vec{\nabla} \cdot \vec{F}_w(S_i^{P_n}) \right) dV + \int_{\partial\Omega_i} W [F^n] dA = 0 \quad (4.25)$$

where $F^n \equiv \left[\mathcal{F} \left(S_i^{P_n}, S_{(i+1)}^{P_n}, \vec{N} \right) - \vec{F}_w(S_i^{P_n}) \cdot \vec{N} \right]$ represents the normal flux difference, i.e. a jump on the flux. Note that the quantity $\vec{\nabla} \cdot \vec{F}_w(S_i^{P_n})$ involves no influence from the data in the neighboring cells, the influence of these data is represented by the above surface integral which is named a penalty term which enforces inter-cell continuity in the domain, to guarantee weakly the identical interface normal flux between immediate neighbor cells. The penalty term in Eq. (4.25) is transformed to a volume integral through the introduction of a correction field, which is called the projection/lifting operator δ_i , that projects the contribution from the surface integrals to the interpolation nodes on Ω_i , such that

$$\int_{\Omega_i} W \delta_i dV = \int_{\partial\Omega_i} W [F^n] dA \quad (4.26)$$

the lifting operator has the normal flux differences on the boundary as input and a member of $P_n(\Omega_i)$ as output. The substitution of Eq. (4.26) into Eq. (4.25) gives the following relation

$$\int_{\Omega_i} \left(\frac{\partial S_i^{P_n}}{\partial t} + \vec{\nabla} \cdot \vec{F}_w(S_i^{P_n}) + \delta_i \right) W dV = 0 \quad (4.27)$$

and since the weighting function W is arbitrary, the integrand in Eq. (4.27) must be zero, hence Eq. (4.27) becomes

$$\frac{\partial S_i^{P_n}}{\partial t} + \vec{\nabla} \cdot \vec{F}_w(S_i^{P_n}) + \delta_i = 0 \quad (4.28)$$

For the construction of the approximate solution $S_i^{P_n}$ in 2D, it is required to define a number of solution points $r_{i,j} = (x_{i,j}, y_{i,j})$, which represents the number of degrees of freedom in the discrete cell. Then, Eq. (4.28) must be satisfied in each SP (Solution Point) j in Ω_i , according to

$$\frac{\partial S_{i,j}^{P_n}}{\partial t} + \vec{\nabla} \cdot \vec{F}_w(S_i^{P_n}) + \delta_{i,j} = 0 \quad (4.29)$$

here, it is worthwhile to note that, Eq. (4.29) is valid for arbitrary types of grid cells.

In general, for non-linear conservation laws, $\vec{\nabla} \cdot \vec{F}_w(S_i^{P_n})$ is not a member of the polynomial space $P_n(\Omega_i)$, thus, it is projected onto this space, via a degree n Lagrange interpolation

polynomial, in the following way; Based on the solution at a SP, the flux vector at each SP can be computed. Then a degree n Lagrange interpolation polynomial for the flux vector is used to approximate the (nonlinear) flux vector

$$\vec{F}_w(S_i^{P_n}) \equiv \sum_j L_j^{\text{SP}}(\vec{r}) \vec{F}_w(S_{i,j}^{P_n}) \quad (4.30)$$

where $L_j^{\text{SP}}(\vec{r})$ is the Lagrange polynomial based on the solution points $\{r_{i,j}\}$. After that, the projection is computed using

$$\Pi_j \left[\vec{\nabla} \cdot \vec{F}_w(S_i^{P_n}) \right] = \sum_j \nabla L_j^{\text{SP}} \cdot \vec{F}_w(S_{i,j}^{P_n}) \quad (4.31)$$

In this case $\Pi_j \left[\vec{\nabla} \cdot \vec{F}_w(S_i^{P_n}) \right]$ is a degree $n-1$ polynomial, which also belongs to P_n . Hence, the Eq. (4.31) can be employed to rewrite Eq. (4.29) as

$$\frac{\partial S_{i,j}^{P_n}}{\partial t} + \Pi_j \left[\vec{\nabla} \cdot \vec{F}_w(S_i^{P_n}) \right] + \delta_{i,j} = 0 \quad (4.32)$$

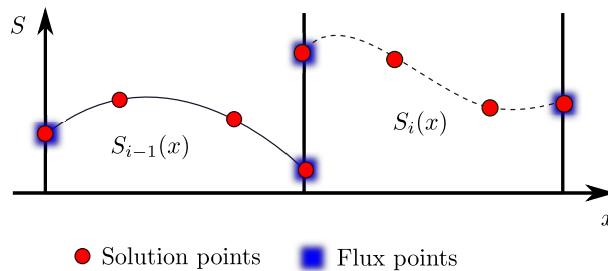
Henceforth, we will focus on different ways to define and calculate an optimal correction function g , which is very important in practice to ensure an efficient implementation of the CPR scheme. In the case of general quadrilateral elements, the correction functions are computed in the quadrilateral reference cell, in a straightforward way, due the fact that all the operations are carried out in a one-dimensional manner using a tensor product basis.

For one-dimensional conservation laws, the correction at the solution points is

$$\delta_{i,j} = \frac{2}{|\mathcal{J}|_{i,j}} (g'_{L,j}[F^n]_L + g'_{R,j}[F^n]_R) \quad (4.33)$$

where, \mathcal{J} is the Jacobian matrix of the transformation and g' is the derivative of the correction function g . Here the cell Ω_i has two numerical faces, a left and right one, and the SPs and FPs (Flux Points) have been chosen on the computational domain as shown in Fig. 8. Finally for one-dimensional case Eq. (4.32) becomes

Figure 8 – P_3 degree solution polynomials, including cell interfaces.



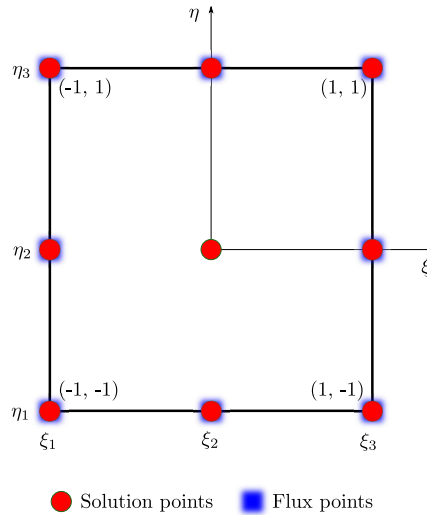
Source: Adapted from Huynh (2007).

To extend the one-dimensional CPR method to two-dimensions, let $S_{i,j,k}$ denote the DOF (degrees of freedom), cell index i and solution point indexes j , and k within quadrilateral elements, where each element i has four faces, see Fig. 9. Thus, the CPR formulation from Eq. (4.32) becomes

$$\frac{\partial S_{w(i,j,k)}^{P_n}}{\partial t} = - \left(\Pi_{j,k} \left[\vec{\nabla} \cdot \vec{F}_w(S_i^{P_n}) \right] + \frac{2}{|\mathcal{J}|_{i,j,k}} \left\{ \begin{aligned} & [\mathcal{F}_x(-1, \eta_{j,k}) - F_{x(i)}(-1, \eta_{j,k})] g'_L(\xi_j) + [\mathcal{F}_x(1, \eta_{j,k}) - F_{x(i)}(1, \eta_{j,k})] g'_R(\xi_j) + \\ & [\mathcal{F}_y(\xi_{j,k}, -1) - F_{y(i)}(\xi_{j,k}, -1)] g'_L(\eta_k) + [\mathcal{F}_y(\xi_{j,k}, 1) - F_{y(i)}(\xi_{j,k}, 1)] g'_R(\eta_k) \end{aligned} \right\} \right) \quad (4.34)$$

$$\frac{\partial S_{i,j}^{P_n}}{\partial t} + \Pi_j \left[\frac{\partial \vec{F}_w(S_i^{P_n})}{\partial x} \right] + \frac{2}{|\mathcal{J}|_{i,j}} (g'_{L,j}[F^n]_L + g'_{R,j}[F^n]_R) = 0 \quad (4.35)$$

Figure 9 – Solution and flux points on reference 2D domain for P_2 approximation.



Source: Adapted from Huynh (2007).

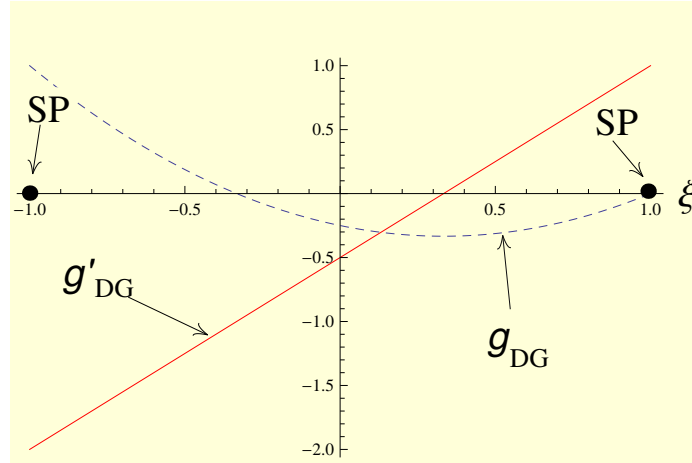
To recovery existing methods, such as, DG, SD/SV and CPR- g_2 methods, we use three different polynomials functions in the following way:

4.2.1.1 Nodal discontinuous Galerkin scheme

To obtain the reconstruction function g_{DG} , which recovers the nodal discontinuous Galerkin scheme, the $R_{R,n}$ (Right Randau) polynomial of degree $n + 1$ can be used. Thus, the g_{DG} correction function is expressed by

$$g_{DG,n} = R_{R,n} = \frac{(-1)^{n+1}}{2} (P_{n+1} - P_n) \quad (4.36)$$

where P_n is the Legendre polynomial of order n . In Fig. 10 are presented the g_{DG} correction function and its derivative. Explicitly, the aforementioned correction function and its derivative,

Figure 10 – Correction function g_{DG} and its derivative g'_{DG} , for $n = 1$.

Source: The author (2018).

for $n = 1$, can be expressed as

$$g_{DG} = \frac{1}{2} \left(-\xi + \frac{1}{2} (-1 + 3\xi^2) \right) \quad \text{and} \quad g'_{DG} = \frac{1}{2} (-1 + 3\xi) \quad (4.37)$$

By substituting the values of $SP(1) = -1.0$ and $SP(2) = 1$ into g'_{DG} Eq. (4.37), we can get directly the correction lifting coefficients, $g'_{L,1} = -2.0$ and $g'_{L,2} = 1.0$, as shown in the first column of Tab. 1.

4.2.1.2 Spectral Difference/Spectral Volume methods

Studies reveals a connection between Spectral Difference and Spectral Volume schemes for one-dimensional case (ABEELE; LACOR; WANG, 2007). Consequently, the reconstruction function $g_{SD/SV}$, which recovery the SD/SV schemes can be expressed as,

$$g_{SD/SV,n} = \frac{(-1)^{n+1}}{2} (1 - \xi)(P_{n+1}), \quad (4.38)$$

Table 1 – Correction lifting coefficients, $g'_{DG(L,j)}$, for linear element $[-1,1]$.

$SP(j)$	P_1 $g'_{L,j}$	P_2 $g'_{L,j}$	P_3 $g'_{L,j}$	P_4 $g'_{L,j}$	P_5 $g'_{L,j}$
1	-2.0	-4.5	-8.0	-12.5	-18.0
2	1.0	0.75	0.8944	1.0714	1.2591
3	-	-1.5	-0.8944	-0.9375	-1.0399
4	-	-	2.0	1.0714	1.0399
5	-	-	-	-2.5	-1.2591
6	-	-	-	-	3.0

Source: Adapted from Huynh (2007).

Table 2 – Correction lifting coefficients, $g'_{(SD/SV)L,j}$, for linear element [-1,1].

SP(j)	P_1 $g'_{L,j}$	P_2 $g'_{L,j}$	P_3 $g'_{L,j}$	P_4 $g'_{L,j}$	P_5 $g'_{L,j}$
1	-3.5	-6.5	-10.5	-15.5	-21.5
2	-0.5	0.75	1.39	1.9129	2.3821
3	-	0.5	-0.3945	-0.9375	-1.3859
4	-	-	-0.5	0.2296	0.6939
5	-	-	-	0.5	-0.1350
6	-	-	-	-	-0.5

Source: Adapted from Huynh (2007).

where P_n is the Legendre polynomial of order n (VINCENT; CASTONGUAY; JAMESON, 2011). In Tab. 2 are presented the constant lifting coefficients, SD/SV, which were calculated in a similar way as described above.

4.2.1.3 CPR- g_2 method

For CPR- g_2 method, the constant lifting coefficients for $g'_{2(L,j)}$ were calculated using the Lagrange polynomial interpolation, and the values are presented in Tab. 3 (ZIMMERMAN; WANG, 2013).

Due to symmetry, we can obtain the $g'_{R,j}$ coefficients, in the following manner $g'_{L,j} = g'_{R,n+2-j}$, which is valid for the one-dimensional case, where the reconstruction polynomial is of degree P_n .

Table 3 – Correction lifting coefficients- $g'_{2(L,j)}$, for linear element [-1,1].

SP(j)	P_1 $g'_{L,j}$	P_2 $g'_{L,j}$	P_3 $g'_{L,j}$	P_4 $g'_{L,j}$	P_5 $g'_{L,j}$
1	2.0	4.5	8.0	12.5	18.0
2	-1.0	-0.75	-0.5938	-0.2612	0.2513
3	-	1.5	0.9688	0.9375	0.8518
4	-	-	-2.0	-1.1451	-1.1244
5	-	-	-	0.5	-1.3103
6	-	-	-	-	-3.0

Source: Adapted from Huynh (2007).

4.2.1.4 1D linear advection equation test

The aim of this study is to compare the reliability and accuracy of the CPR– g_2 , SV/SD, and DG methods of the results obtained for the 1D linear advection equation

$$\frac{\partial S}{\partial t} + v \frac{\partial S}{\partial x} = 0 \quad (4.39)$$

with $v = 1$. The computational domain is $0 \leq x \leq 1$, with periodic boundary conditions. At the cell boundaries, a Roe's approximate Riemann flux was used. The initial solution is a sinusoidal pulse given by

$$S(x, 0) = \sin(\pi x) \quad (4.40)$$

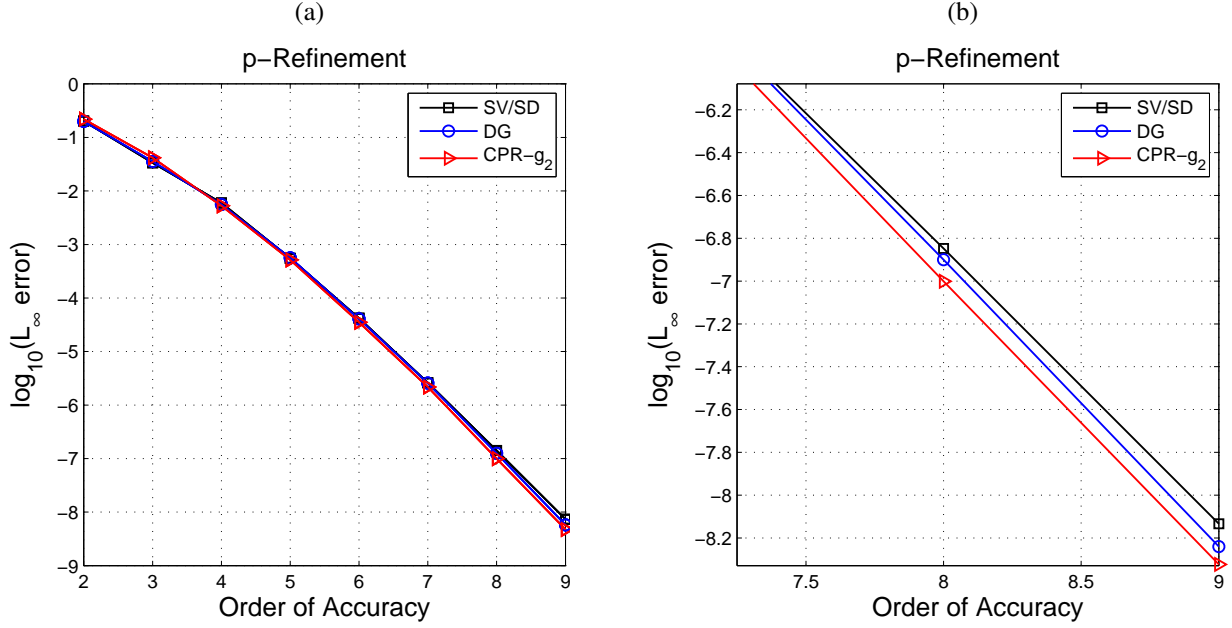
For time integration, a third-order TVD Runge-Kutta scheme was used, with a time step $\Delta t = 10^{-4}$ to ensure negligible time discretization errors. This simulation was carried out for various orders of accuracy $(n + 1) = 2, 3, 4$, for a final time $t = 1$. In Tab. 4 are shown the L_∞ and L_1 norms of error, for the CPR– g_2 , SV/SD and DG schemes. On the other hand, the Gauss-Lobatto distribution was used to localize the SPs (Solution Points) for the aforementioned schemes. As can be seen in Tab. 4, the CPR– g_2 SV/SD and DG are able to achieve super-resolution and the formal order of accuracy without problem. Similar to FEM (Finite Element Method) context for the p-refinement test, the number of cells of the primal mesh is maintained fixed, while the degree of the polynomial reconstruction n is increased inside an element. As depicted in Fig. 11, notice that logarithm of the L_∞ decreases linearly with respect to the order of accuracy, demonstrating spectral convergence behavior. Here, a slight improvement of CPR– g_2 behavior over SV/SD and DG was observed, this is clearly due to the optimal reconstruction function used by the CPR– g_2 method.

Table 4 – Accuracy study for 1-D linear advection equation CPR– g_2 SV/SD and DG, using Gauss-Lobatto distribution.

P_n	Δx	NDOF	L_∞ error			L_∞ order			L_1 error			L_1 order		
			CPR– g_2	SV/SD	DG	CPR– g_2	SV/SD	DG	CPR– g_2	SV/SD	DG	CPR	SV/SD	DG
$n = 1$	1.00e-1	20	5.34e-2	1.52e-2	5.50e-2	-	-	-	3.29e-2	9.80e-2	9.80e-3	-	-	-
	5.00e-2	40	1.41e-2	5.50e-3	5.50e-3	1.92	1.45	1.45	8.72e-3	3.60e-3	3.60e-3	1.92	1.46	1.46
	2.50e-2	80	3.56e-3	1.70e-3	1.70e-3	1.99	1.69	1.69	2.24e-3	1.10e-3	1.10e-3	1.96	1.71	1.71
	1.25e-2	160	8.94e-4	4.70e-4	4.72e-4	1.99	1.87	1.86	5.65e-4	3.00e-4	3.00e-4	1.99	1.86	1.86
	6.25e-3	320	2.24e-4	1.24e-4	1.23e-4	2.00	1.93	1.94	1.42e-5	7.86e-5	7.84e-5	1.99	1.93	1.94
$n = 2$	6.67e-2	30	3.90e-3	2.58e-3	3.90e-3	-	-	-	1.60e-3	1.07e-3	1.60e-3	-	-	-
	3.33e-2	60	5.09e-4	3.45e-4	5.23e-4	2.92	2.90	2.89	2.06e-4	1.36e-4	2.06e-4	2.95	2.97	2.95
	1.67e-2	120	6.44e-5	4.46e-5	7.89e-5	2.98	2.95	2.73	2.57e-5	1.73e-5	2.58e-5	3.00	2.97	2.99
	8.33e-3	240	8.07e-6	5.67e-6	1.01e-5	3.00	2.98	2.97	3.21e-6	2.18e-6	0.33e-5	3.00	2.99	2.97
	1.25e-2	480	1.00e-6	7.14e-7	1.27e-6	3.00	2.99	2.99	4.02e-7	2.74e-7	0.41e-6	3.00	2.99	3.00
$n = 3$	1.00e-1	20	2.60e-3	2.23e-3	2.60e-3	-	-	-	8.43e-4	6.77e-4	8.31e-4	-	-	-
	5.00e-2	40	1.94e-4	1.53e-4	1.81e-4	3.75	3.86	3.82	6.07e-5	4.61e-5	5.81e-5	3.80	3.88	3.84
	2.50e-2	80	1.23e-5	9.52e-6	1.31e-5	3.98	4.00	3.79	3.72e-6	2.95e-6	0.40e-5	4.03	3.97	3.86
	1.25e-2	160	7.75e-7	6.00e-7	0.85e-6	3.99	3.99	3.95	2.32e-7	1.86e-7	0.26e-6	4.00	3.99	3.94
	6.25e-3	320	4.86e-8	3.75e-8	2.35e-6	4.00	4.00	3.97	1.45e-8	1.17e-8	0.16e-7	4.00	3.99	4.02

Source: The author (2018).

Figure 11 – Spectral accuracy of the SV/SD, DG and CPR schemes using p-refinement, for the advection equation (a) A close-up view of spectral accuracy test (b).



Source: The author (2018).

4.2.1.5 Conservation issues

The aim here is to understand the local mass conservation property for the CPR method. Let us begin with the following weak formulation

$$\int_{\Omega_i} \left[\frac{\partial S_i^{P_n}}{\partial t} + \vec{\nabla} \cdot \vec{F}_w(S_i^{P_n}) + \delta_i \right] W dV = 0 \quad (4.41)$$

which was derived by applying a weighted residual formulation to the hyperbolic conservation law Eq. (4.18). We can rewrite Eq. (4.41) as

$$\int_{\Omega_i} W \frac{\partial S_i^{P_n}}{\partial t} dV + \int_{\Omega_i} W (\vec{\nabla} \cdot \vec{F}_w(S_i^{P_n})) dV + \int_{\Omega_i} W \delta_i dV = 0 \quad (4.42)$$

Here, we employed LP (Lagrange polynomial) interpolation to derive the correction coefficients Eq. (4.26) and to compute the divergence of the flux vector Eq. (4.31), in the following form

$$\int_{\Omega_i} W \delta_i dV = \int_{\partial\Omega_i} W [\mathcal{F} - \vec{F}_w(S_i^{P_n})]^{LP} dA, \quad \Pi^{LP}(\vec{\nabla} \cdot \vec{F}_w(S_i^{P_n})) = \sum_j \vec{\nabla} L_j^{SP} \cdot \vec{F}(S_{i,j}) \quad (4.43)$$

where, L_j is the bi-dimensional Lagrange polynomial. By substitution of Eq. (4.43) into Eq. (4.42) yields

$$\int_{\Omega_i} W \frac{\partial S_i^{P_n}}{\partial t} dV + \int_{\Omega_i} W \Pi_i(\vec{\nabla} \cdot \vec{F}_w(S_i^{P_n})) dV + \int_{\partial\Omega_i} W [\mathcal{F} - \vec{F}_w(S_i^{P_n})] dA = 0 \quad (4.44)$$

we have dropped the index LP for simplicity. Using a test function $W = 1$, which suffices to guarantee that the weighted residual formulation is conservative, see Eq. (4.19), we get

$$\int_{\Omega_i} \frac{\partial S_i^{P_n}}{\partial t} dV + \int_{\Omega_i} \Pi_i(\vec{\nabla} \cdot \vec{F}_w(S_i^{P_n})) dV + \int_{\partial\Omega_i} \vec{F}_w(S_i^{P_n}) dA + \int_{\partial\Omega_i} \mathcal{F} dA = 0 \quad (4.45)$$

reordering Eq. (4.45) becomes

$$\int_{\Omega_i} \frac{\partial S_i^{P_n}}{\partial t} dV + \int_{\partial\Omega_i} \mathcal{F} dA + \left[\int_{\Omega_i} \Pi_i(\vec{\nabla} \cdot \vec{F}_w(S_i^{P_n})) dV - \int_{\partial\Omega_i} \vec{F}_w(S_i^{P_n}) dA \right] = 0 \quad (4.46)$$

Since the term in square bracket in Eq. (4.46) vanishes, by applying the divergence theorem to the flux \vec{F}_w , which was approximated using the Lagrange interpolation in both the volume and boundary integrals, thus, we obtain the integral conservation law

$$\int_{\Omega_i} \frac{\partial S_i^{P_n}}{\partial t} dV + \int_{\partial\Omega_i} \mathcal{F}(S_i^{P_n}, S_{i+}^{P_n}, \vec{N}) dA = 0 \quad (4.47)$$

which must be satisfied in each CV Ω_i . Note that to ensure that the CPR scheme is locally conservative, the sum of all mass flux contribution along Ω_i faces should be zero. In other words, a mass flux leaving the cell Ω_i must completely enter the immediate neighboring cell without any mass generation or loss. The mass flux over a face can be computed directly, via a approximate Riemann flux at the face flux points, and then using a Gauss quadrature rule to obtain the total contribution on the edge.

4.2.2 Approximate Riemann solvers

The best method of determining the solution of a local Riemann problem is by calculating its exact solution. It is worth emphasizing that it is not straightforward besides being numerically expensive. Moreover, taking into account that sources of numerical errors always exists, another way of achieving a similar result is to replace the solution of the exact Riemann problem by an approximate solution, which will be introduced in the following discussion

At each interface between two adjacent cells, a unique common Riemann flux, as in a finite volume method, is used to deal with the numerical solution, which is a piecewise polynomial reconstruction, and hence, discontinuous across interfaces. In addition, this implies that the fluxes $F_w(S^-, S^+)$ are not directly defined with the available information, the superscripts (-) e (+) are used to indicate the left and right sides of numerical interfaces, respectively. In order to construct appropriate approximations for fluxes, the numerical flux should be defined such that given the values $S_{i+1/2}^-$ and $S_{i+1/2}^+$ on each cell side of the interface $x_{i+1/2}$, the numerical flux function $\mathcal{F}(S^-, S^+)$ returns an upstream approximation to the actual flux $F_w(S_{i+1/2})$. In this work, we use a Roe-E scheme with entropy fix, as proposed by Shu e Osher (1989), which can be written as follows

$$\mathcal{F}_{\text{Roe-E}} \cdot \vec{N} = \begin{cases} \mathcal{F}_{\text{LLF}} \cdot \vec{N}, & \text{if } \frac{\partial F_w}{\partial S}(S^-) \cdot \frac{\partial F_w}{\partial S}(S^+) < 0 \\ \mathcal{F}_{\text{Roe}} \cdot \vec{N}, & \text{otherwise} \end{cases} \quad (4.48)$$

where the LLF (Local Lax-Friedrichs) flux is defined as (COCKBURN; LIN; SHU, 1989)

$$\mathcal{F}_{\text{LLF}} \cdot \vec{N} = \frac{1}{2} \left[(F_w(S^+) + F_w(S^-)) \cdot \vec{N} - \max |\mathcal{B}| (S^+ - S^-) \right] \quad (4.49)$$

with

$$\mathcal{B} = \frac{\partial F_w(S)}{\partial S_w} \cdot \vec{N}$$

and the Roe's linearized Riemann solver, also called Murman or Murman-Roe in the scalar case is given as

$$\mathcal{F}_{\text{Roe}} = \begin{cases} F_w(S_w^-), & \text{if } \mathcal{B} \geq 0 \\ F_w(S_w^+), & \text{otherwise} \end{cases} \quad (4.50)$$

In the general case, the LLF numerical flux provides a large dose of artificial viscosity, when compared to the Roe-E numerical flux.

4.2.2.1 Numerical example

To understand what role the Riemann flux plays when applied to high-order approximations, and which criteria should be used when choosing these, we will consider the following example to appreciate the accuracy of said methods. Let us consider the Buckley-Leverett equation, which can be written in the following form

$$\frac{\partial S}{\partial t} + \frac{\partial F_w}{\partial x} = 0, \quad -1.0 \leq x \leq 1.0 \quad (4.51)$$

with non-convex fractional flux function and initial data, given by

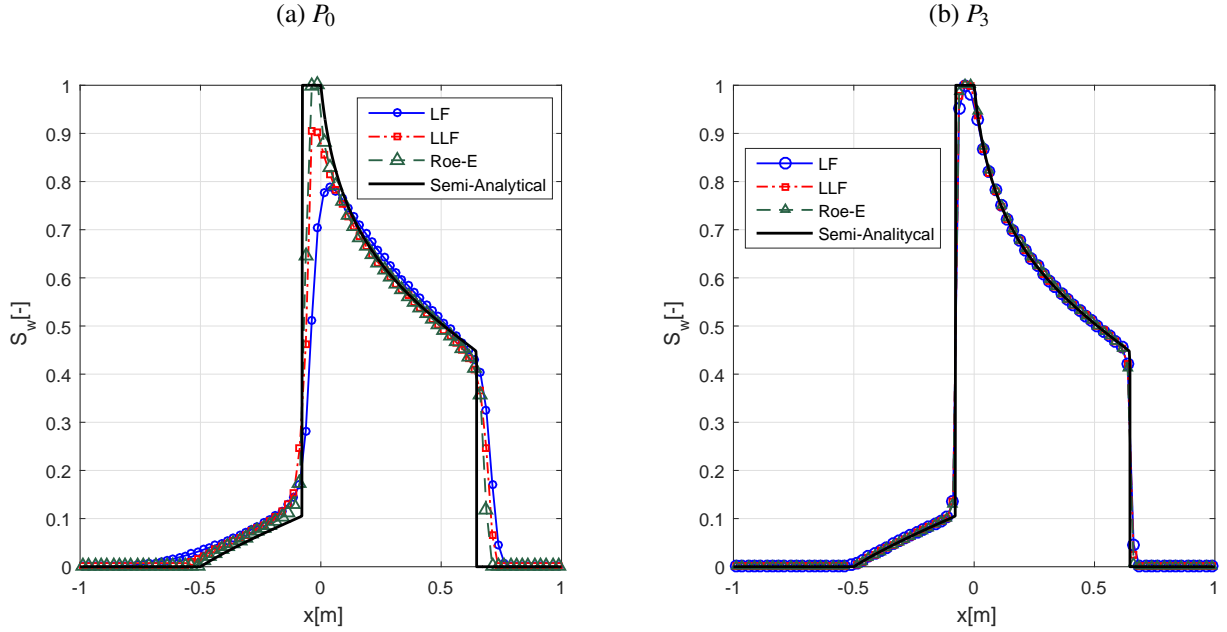
$$f_w = \frac{MS^2}{MS^2 + (1-S)^2}, \quad S(x, 0) = \begin{cases} 1, & \text{if } -0.5 \leq x \leq 0 \\ 0 & \text{otherwise} \end{cases} \quad (4.52)$$

with $M = 4$ being the ‘‘mobility’’ ratio and periodic boundary conditions. Comparing the results in Fig. 12(a), we see a significant smearing of the shock as a result of the type of approximate Riemann solver employed, i.e., in the general case indeed less artificial viscosity is introduced and better overall accuracy can be observed, in going from the LF to Roe-E. However, this difference becomes much smaller for higher order reconstructions (SHU, 1998, p. 21), as depicted in Fig. 12(b), where we utilize a Hierarchical MLP strategy to avoid oscillatory solutions around the points of discontinuity, as will be introduced in next subsection. Although in this example $f'_w(S) > 0 \forall S \in [0, 1]$, i.e., without sonic points, the Roe-E does not switch to a Lax-Friedrichs scheme, then, we can see an improvement using the simple Roe upwind flux, this is simply due the LF and LLF Riemann solver always introduces some extra dissipation whenever it is invoked at a discontinuity.

4.2.3 Shock capturing strategies

In this section, we shall give a description of two shock capturing strategies to deal with discontinuities, while keeping the high order of accuracy in smooth regions of domain. To

Figure 12 – Buckley Leverett problem for $t = 0.4$, 80 cells and $CFL = 0.9$ (a) Solution using a low-order approximation (b) Solution using a high-order approximation.



Source: The author (2018).

preserve the accuracy away from the shock region a trouble cell marker is used. The trouble cell marker is a very important part of the algorithm, it detects the cells in a region with discontinuities, where the shock capturing strategy will be triggered.

4.2.3.1 TVB marker and minmod slope limiting strategy

To identify the trouble cells, we use the following limited edge values:

$$S_i^- = \bar{S}_i - \min\text{mod} \left[(\bar{S}_i - S_i^L), (\bar{S}_i - \bar{S}_{i-1}), (\bar{S}_{i+1} - \bar{S}_i) \right] \quad (4.53)$$

$$S_i^+ = \bar{S}_i + \min\text{mod} \left[(S_i^R - \bar{S}_i), (\bar{S}_i - \bar{S}_{i-1}), (\bar{S}_{i+1} - \bar{S}_i) \right] \quad (4.54)$$

with \bar{S}_i being the averaged solution and S_i^L and S_i^R are the end saturation values of element Ω_i . If $S_i^- \neq S_i^L$ or $S_i^+ \neq S_i^R$, then, the element Ω_i is identified as a trouble cell and a conventional slope limiting strategy is employed, but otherwise, the local solution is not altered. To compute the limited P_n approximation, we assume that the solution is represented by a linear reconstruction, that is

$$S_i^{P_n}(x) = \bar{S}_i + (x - x_0) \nabla \bar{S}_i \quad (4.55)$$

where x is the position and x_0 is the centroid of Ω_i . Then, the slope limited solution is obtained by applying the following limiting procedure

$$\mathcal{L}[S_i^{P_1}(x)] = \bar{S}_i + (x - x_0) \min\text{mod} \left(\nabla \bar{S}_i, \frac{\bar{S}_{i+1} - \bar{S}_i}{h}, \frac{\bar{S}_i - \bar{S}_{i-1}}{h} \right) \quad (4.56)$$

where h is the length of Ω_i and the minmod function with three parameters is defined as

$$\text{minmod}(a, b, c) = \begin{cases} s \min(|a|, |b|, |c|), & \text{if } s = \text{sign}(a) = \text{sign}(b) = \text{sign}(c) \\ 0, & \text{otherwise} \end{cases} \quad (4.57)$$

The minmod function will return a zero unless the three arguments have the same sign. In this special case, it will return the smallest of the three arguments with the correct sign. To overcome the loss of accuracy close to local extrema, the minmod function is modified in the following form

$$\widetilde{\text{minmod}}(a, b, c) = m(a, b + \sigma h^2 \text{sign}(b), c + \sigma h^2 \text{sign}(c)) \quad (4.58)$$

The σ parameter is an upper bound on the second derivative of the solution (WANG, 2002; HESTHAVEN; WARBURTON, 2008).

4.2.3.2 Hierarchical MLP (Multidimensional Limiter Procedures) strategy

To achieve monotonicity using higher order approximations, i.e., to avoid spurious oscillations in the vicinity of solutions discontinuities or steep gradients, and ensuring formal accuracy in smooth regions, the Hierarchical MLP is employed (PARK; KIM, 2016).

In order to detect trouble cells, let us first consider the linear MLP condition which is used as a troubled-cell marker for higher-order approximation and can be written as

$$\bar{S}_i^{\min} \leq \Pi^1 S_i^{P_n}(\vec{r}_{v_J}) \leq \bar{S}_i^{\max} \quad (4.59)$$

where $\Pi^1 S_i^{P_n}(\vec{r}_{v_J})$ is the linear projected approximation of a $S_i^{P_n}(\vec{r}_{v_J})$ reconstruction onto ($n = 1$) polynomial space at vertex point v_J , \bar{S}_i^{\min} and \bar{S}_i^{\max} are the minimum and maximum cell-averaged values \bar{S}_i , respectively, among all neighboring cells that share any vertex v_J of Ω_i , with $J = 1, \dots, \mathcal{N}_v$ where \mathcal{N}_v is the total number of vertices of Ω_i , see gray-shaded region in Fig. 13. The projection procedure from $S_i^{P_n}(\vec{r})$ to linear approximation $\Pi^m S_i^{P_n}(\vec{r})$ with $m = 1$ is realized by computing the modal coefficients

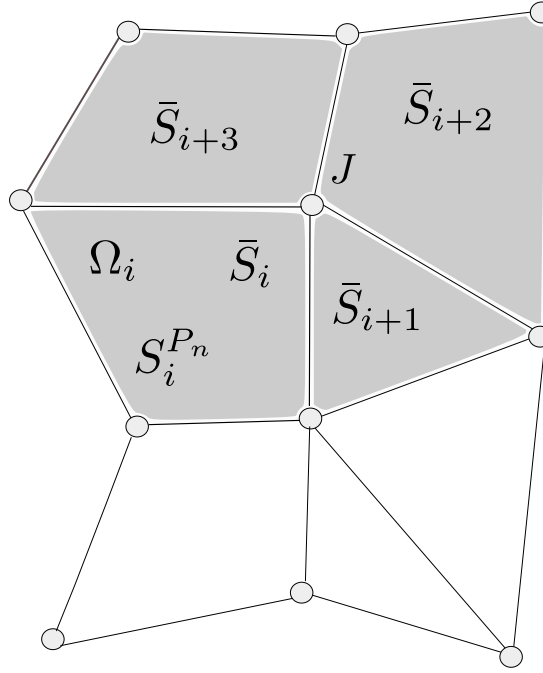
$$\hat{S}_i^{P_n}(\vec{r}) = \mathcal{V}^{-1} S_i^{P_n}(\vec{r}) \quad (4.60)$$

and truncating the higher-order modes $\mathcal{T}[\hat{S}_i^{P_n}(\vec{r})]$ greater than $n = 1$. In above equation, $\hat{S} = [\hat{S}^1, \dots, \hat{S}^{n+1}]^T$ are the $(n + 1)$ expansion coefficients and $S = [S(\vec{r}_1), \dots, S(\vec{r}_{n+1})]^T$ represents the $(n + 1)$ solution point values and \mathcal{V} is the Vandermonde matrix (HESTHAVEN; WARBURTON, 2008). Then, the projected solution can be written as

$$S_i^{P_n}(\vec{r}) = \mathcal{V} \mathcal{T}[\hat{S}_i^{P_n}(\vec{r})] \quad (4.61)$$

In order to distinguish a local smooth extreme from a discontinuous one, the following MLP smooth extreme detector is used

$$S_i^{P_n}(\vec{r}_{v_J}) = \bar{S}_i + \underbrace{(\Pi^1 S_i^{P_n}(\vec{r}_{v_J}) - \bar{S}_i)}_{\text{Linear term}} + \underbrace{(S_i^{P_n}(\vec{r}_{v_J}) - \Pi^1 S_i^{P_n}(\vec{r}_{v_J}))}_{\text{Higher-order term}} \quad (4.62)$$

Figure 13 – MLP stencil for Ω_i .

Source: Adapted from Park e Kim (2016).

The smooth extreme detector begins by evaluating on the following criteria for each vertex $v_J \in \Omega_i$

C1 – If there is a local maximum near vertex v_J , then

$$\text{Linear term} > 0, \text{Higher-order term} < 0, S_i^{P_n}(\vec{r}_{v_J}) > \bar{S}_i^{\min}$$

(4.63)

C2 – If there is a local minimum near vertex v_J , then

$$\text{Linear term} < 0, \text{Higher-order term} > 0, S_i^{P_n}(\vec{r}_{v_J}) < \bar{S}_i^{\max}$$

The emphasis so far has been on the detection of troubled-cells, what remains now is to introduce the hierarchical MLP process to deal with those trouble-cells. To pursue this idea, let us first write the limited $\mathcal{L}[S_i^{P_n}(\vec{r})]$ reconstruction in the following way

$$\begin{aligned} \mathcal{L}[S_i^{P_n}(\vec{r})] = & \bar{S}_i + \phi_{\text{MLP}} \mathcal{M}1_i(\vec{r}) + \phi_i^{P_2} [\mathcal{M}2_i(\vec{r}) + \\ & \phi_i^{P_3} (\mathcal{M}3_i(\vec{r}) + \dots + \phi_i^{P_n} \mathcal{M}n_i(\vec{r}))] \end{aligned} \quad (4.64)$$

with the $\mathcal{M}m_i(\vec{r})$ modes being

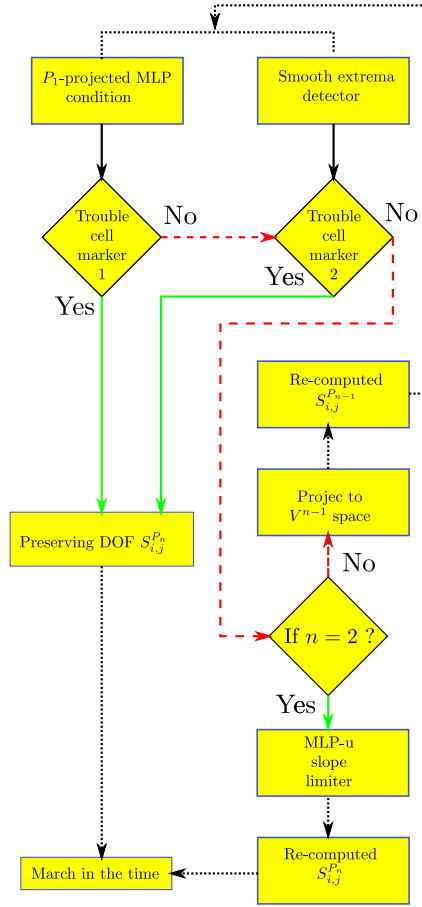
$$\mathcal{M}m_i(\vec{r}) = \Pi^m S_i^{P_n}(\vec{r}) - \Pi^{(m-1)} S_i^{P_n}(\vec{r}), \quad 1 \leq m \leq n \quad (4.65)$$

Now, for each cell Ω_i , the trouble-cell marker $\phi_i^{P_m}$ is given as

$$\phi_i^{P_m} = \min_{\forall v_J \in \Omega_i} \begin{cases} 1 & \text{if Eq. (4.59) or Eq. (4.63) is satisfied} \\ 0 & \text{otherwise} \end{cases} \quad (4.66)$$

the trouble-cell marker $\phi_i^{P_m}$ takes the constant value of 1 or 0. The first condition ensures that the local high-order accuracy is maintained and the second condition expresses that a trouble-cell

Figure 14 – Flowchart of the hierarchical MLP limiting procedure, solid green line \rightarrow if criteria is satisfied, and dashed red line \rightarrow else.



Source: Adapted from Park e Kim (2016).

was detected in the highest mode, then, the lowest $\mathcal{M}1_i$ mode is achieved in a hierarchical manner.

Finally, the $\mathcal{M}1_i$ mode is limited by the following MLP-u1 slope limiter

$$\phi_{\text{MLP}} = \min_{\forall v_J \in \Omega_i} \begin{cases} \min(1, \psi_{i,v_J}) & \text{if } |\mathcal{M}1_i(\vec{r}_{v_J})| \geq \epsilon_{\text{machine}} \\ 1 & \text{otherwise} \end{cases} \quad (4.67)$$

in which, $\epsilon_{\text{machine}}$ is the machine epsilon, and

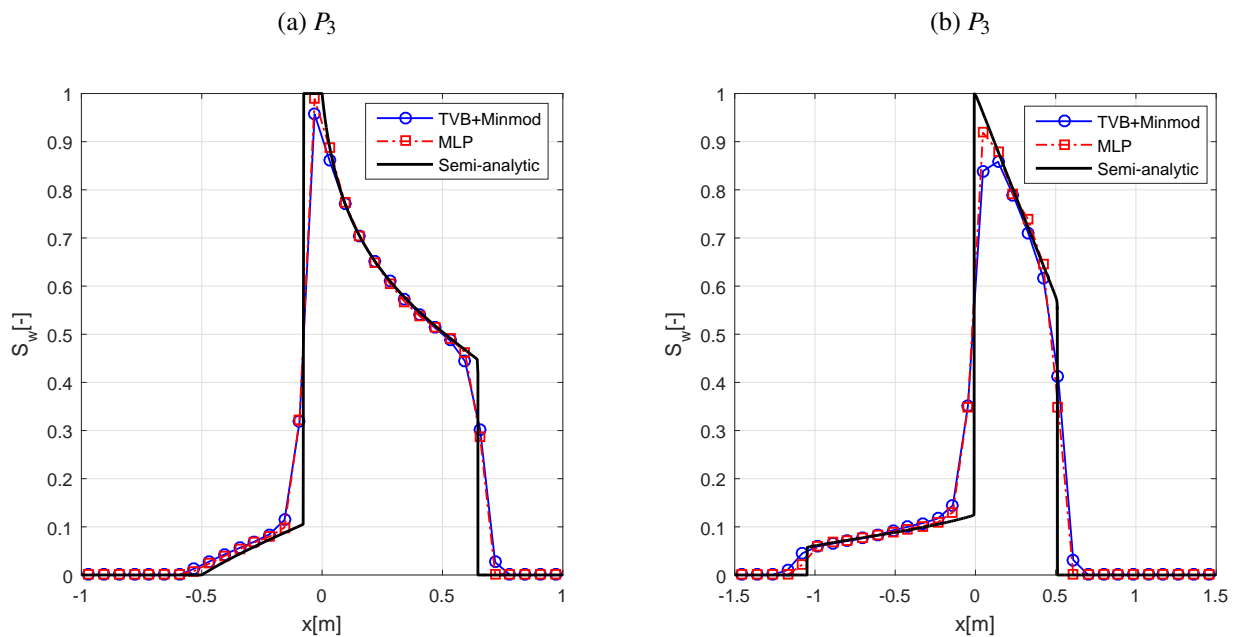
$$\psi_{i,v_J} = \max \left(\frac{\bar{S}_i^{\min} - \bar{S}_i}{\mathcal{M}1_i(\vec{r}_{v_J})}, \frac{\bar{S}_i^{\max} - \bar{S}_i}{\mathcal{M}1_i(\vec{r}_{v_J})} \right) \quad (4.68)$$

In order to better understanding of what is happening during the limiting process, Fig. 14 illustrates a schematic summary of the hierarchical MLP limiting procedure for an arbitrary degree approximation.

4.2.3.3 Numerical example

In the following test, we will discuss two different techniques aimed at addressing Gibb's oscillations introduced by the use of a high-order polynomial basis. We will attempt to show the advantage of the hierarchical limiting strategy over classical techniques, such as slope limiters (HESTHAVEN; WARBURTON, 2008). Based on earlier subsection, here we use a Roe-E approximate numerical flux, which give an excellent resolution of the shock as well as high accuracy away from the shock location, including both the low and high order approximations. For the case with adverse gravity effect, we use a mobility rate of $M = 100$, and a dip angle of $\theta = 45^\circ$, the other parameters remain the same as in the earlier test. In this test, for purposes of comparison, a TVB marker as proposed by (COCKBURN; SHU, 1998) is used to identify trouble cells and a conventional slope limiting strategy is employed, if limiting process is needed. Unfortunately, when a trouble cell is identified, the slope limiter will alter the local solution and decreases the accuracy to first order, causing a severe smearing of the shocks, as illustrated in Figs. 15. On the other hand, to overcome that problem, a Hierarchical MLP strategy is used in this work, as introduced above. Then, when a trouble cell is identified for high-order modes, Eq. (4.66), the hierarchical process starts, by decreasing the local approximation up first order of accuracy, which does not impact the high-order accuracy around extrema, as depicted in Figs. 15. We also observe that Fig. 15 (b) indicates that, for the special case with gravity effects even, the solution is fully non-oscillatory. For this test, it is worth emphasizing that the Roe-E flux always yields the correct entropy solution, due to the fact that we switch to an LLF scheme at isolated

Figure 15 – Buckley Leverett problem for $t = 0.4$, 32 cells and $CFL = 0.9$ (a) Solution without gravity effect (b) Solution with gravity effect.



Source: The author (2018).

sonic points, i.e., only in the cells which contain “expansion shocks”.

4.3 From nodal to cell-centered solutions

Once a nodal solution $S_{i,j}^{P_n}$ has been computed for a CV Ω_i , the CV piecewise cell-centered finite volume solution $\bar{S}_i^{P_n}$ must be recovered. This is achieved via the quadrature rules or the modal coefficients as adopted in the present work, which are calculate using the generalized Vandermonde Matrix \mathcal{V} (HESTHAVEN; WARBURTON, 2008) as will be presented in what follows.

For convenience, the analysis is performed for a one-dimensional case, but results are equally valid for the two-dimensional case.

4.3.1 Classic form using quadratures

The local solution in 1D can be written using a polynomial function of order P_n in nodal form as

$$S_i^{P_n}(x, t) = \sum_{j=1}^{n+1} S_i^{P_n}(\xi_j, t) L_j^{\text{SP}}(\xi), \quad x \in \Omega_i \quad (4.69)$$

where $S_i^{P_n}(\xi_j, t)$ was mapped from physical domain to the reference domain via a affine mapping. In the above equation, the Lagrange polynomial for the solution point ξ_j can be obtained as

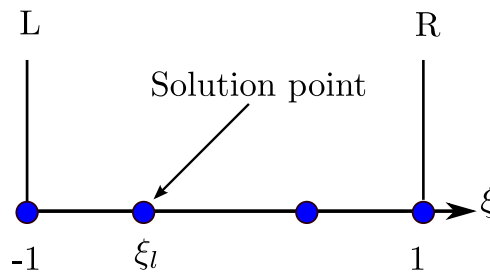
$$L_j^{\text{SP}}(\xi) = \prod_{l=1, l \neq j}^{n+1} \frac{\xi - \xi_l}{\xi_j - \xi_l} \quad (4.70)$$

where the reference variable $-1 \leq \xi \leq 1$, see Fig. 16. Explicitly for P_1 , with $\xi_1 = -1$, $\xi_2 = 1$ we have

$$L_1 = \frac{\xi - \xi_2}{\xi_1 - \xi_2} = \frac{1 - \xi}{2} \quad (4.71)$$

$$L_2 = \frac{\xi - \xi_1}{\xi_2 - \xi_1} = \frac{1 + \xi}{2} \quad (4.72)$$

Figure 16 – Solution point on reference domain.



Source: The author (2018).

In order to calculate the cell average value via the mean value theorem, we have

$$\bar{S}^{P_n} = \frac{1}{b-a} \int_a^b S^{P_n}(\xi, t) d\xi \quad (4.73)$$

or in explicit form using Eq. (4.69) as

$$\bar{S}^{P_n} = \frac{1}{2} \int_{-1}^1 [S^{P_n}(\xi_1, t)L_1(\xi) + S^{P_n}(\xi_2, t)L_2(\xi)] d\xi \quad (4.74)$$

which can be seen as a quadrature rule

$$\bar{S}^{P_n} = \frac{1}{2} [S^{P_n}(\xi_1, t)w_1 + S^{P_n}(\xi_2, t)w_2] \quad (4.75)$$

where the weights are calculate as follows

$$w_i = \int_{-1}^1 L_i(\xi) d\xi \quad (4.76)$$

Table 5 presents the 1D Gauss-Lobatto quadrature points and weights for polynomial order, up to P_2 .

4.3.2 Non classic form using the Vandermonde matrix and modal coefficients

The local solution in 1D can be written using a polynomial function of n order in modal form, using a affine mapping $x(\xi)$ as

$$S^{P_n}(x, t) = \sum_{j=1}^{n+1} \hat{S}_j(t) \varphi(\xi) \quad (4.77)$$

Considering a simple monomial base $\varphi(\xi) = \xi^{j-1}$, the previous equation become

$$S^{P_n}(x) = \sum_{j=1}^{n+1} \hat{S}_j \xi^{j-1} \quad (4.78)$$

For P_1 , in explicit form, the latter equation can be written as

$$S^{P_1}(x) = \hat{S}_1 + \hat{S}_2 \xi \quad (4.79)$$

Table 5 – The weights w_l for Gauss-Lobatto nodes ξ_l , which are used to calculate the cell averages.

P_n	ξ_l	w_l
P_1	-1	1
	1	1
P_2	-1	1/3
	0	4/3
	1	1/3

with a set of $n + 1$ distinct grid points in reference space, and \hat{S} the modal coefficients. In order to obtain \bar{S}^{P_n} from S^{P_n} , a local system of equations must be solved, which involves the generalized Vandermonde matrix \mathcal{V} (HESTHAVEN; WARBURTON, 2008). First, we calculate the modal coefficients in the following form

$$\hat{S}_j = \mathcal{V}^{-1} S^{P_n} \quad (4.80)$$

In order to obtain the cell averaged solutions, we truncate the higher-order modes $\mathcal{T}[\hat{S}_j]$ greater than $j = 1$, then the projected cell averaged solution can be written as

$$\bar{S}^{P_n}(x) = \mathcal{V} \mathcal{T} \begin{pmatrix} \hat{S}_1 \\ \hat{S}_2 \\ \vdots \\ \hat{S}_{n+1} \end{pmatrix} \quad (4.81)$$

where the Vandermonde matrix \mathcal{V} is an array in which each element is a Legendre polynomial of degree n , evaluated at the Gauss-Lobatto quadrature points ξ_l , in the following way

$$\mathcal{V} = \begin{pmatrix} P_0(\xi_1) & P_1(\xi_1) & P_n(\xi_1) \\ P_0(\xi_2) & \ddots & \vdots \\ P_0(\xi_{n+1}) & \dots & P_n(\xi_{n+1}) \end{pmatrix} \quad (4.82)$$

In Tab. 6, we depict the Legendre polynomials up to P_2 , which were obtained using the Rodrigues formula

$$P_n(\xi) = \frac{1}{2^n n!} \frac{d^n}{d\xi^n} [(\xi^2 - 1)^n] \quad (4.83)$$

Explicitly, by using Eq. (4.80) for P_2 we have,

$$\begin{pmatrix} \hat{S}_1 \\ \hat{S}_2 \\ \hat{S}_3 \end{pmatrix} = \begin{pmatrix} P_0(\xi_1) & P_1(\xi_1) & P_2(\xi_1) \\ P_0(\xi_2) & P_1(\xi_2) & P_2(\xi_2) \\ P_0(\xi_3) & P_1(\xi_3) & P_2(\xi_3) \end{pmatrix}^{-1} \begin{pmatrix} S_1^{P_2} \\ S_2^{P_2} \\ S_3^{P_2} \end{pmatrix} \quad (4.84)$$

and by truncating

$$\mathcal{T} \begin{pmatrix} \hat{S}_1 \\ \hat{S}_2 \\ \hat{S}_3 \end{pmatrix} = \begin{pmatrix} \hat{S}_1 \\ 0 \\ 0 \end{pmatrix} \quad (4.85)$$

Table 6 – The Legendre polynomials P_n .

n	$P_n(\xi)$
0	1
1	ξ
2	$\frac{1}{2}(3\xi^2 - 1)$

Finally, we obtain

$$\bar{S}^{P_2}(x) = \begin{pmatrix} P_0(\xi_1) & P_1(\xi_1) & P_2(\xi_1) \\ P_0(\xi_2) & P_1(\xi_2) & P_2(\xi_2) \\ P_0(\xi_3) & P_1(\xi_3) & P_2(\xi_3) \end{pmatrix} \begin{pmatrix} \hat{S}_1 \\ 0 \\ 0 \end{pmatrix} \quad (4.86)$$

in which, the first-row value is the cell average solution, that corresponds to the truncated modal solution of order $n = 0$.

4.3.3 Numerical example

The aim of this section is to illustrate the calculation of the cell average solutions, using quadrature rule and the Vandermonde matrix for the 1D linear advection equation

$$\frac{\partial S}{\partial t} + v \frac{\partial S}{\partial x} = 0 \quad (4.87)$$

with $v = 1$. The computational domain is $-1 \leq x \leq 1$, with periodic boundary conditions. At the cell boundaries, a Roe-E approximate Riemann flux was used. The initial solution was a sinusoidal pulse, given by:

$$S(x, 0) = -\sin(\pi x), \quad (4.88)$$

For time integration, we use a third-order TVD Runge-Kutta scheme, with a time step $\Delta t = 10^{-4}$. This simulation was carried out for P_2 , with 5 elements, and final time $t = 2$.

The solution computed is given by the matrix solution, with the matrix size ($SP_s \times$ Elements)

$$S^{P_2} = \begin{bmatrix} -0.0247 & 0.9595 & 0.6177 & -0.5777 & -0.9747 \\ 0.5891 & 0.9423 & -0.0067 & -0.9465 & -0.5782 \\ 0.9462 & 0.5865 & -0.5837 & -0.9473 & -0.0018 \end{bmatrix} \quad (4.89)$$

see Fig. 17.

Initially, we calculate the cell average for the first element via quadrature rules P_2 , given by Eq. (4.75) and Tab. 5, such that

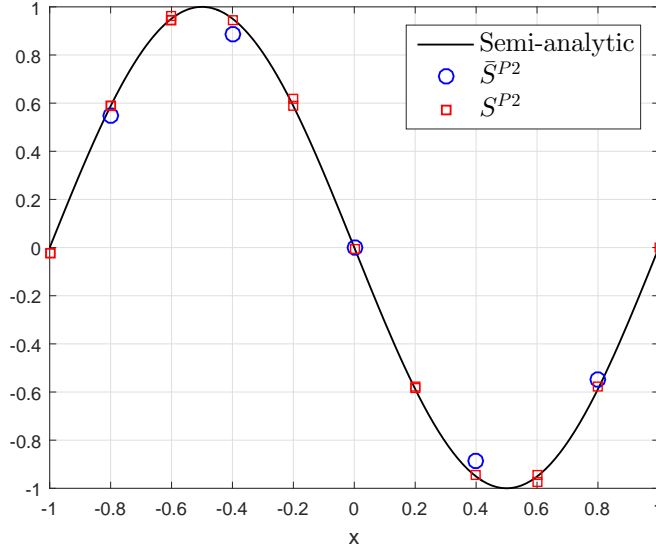
$$\bar{S}^{P_2} = \frac{1}{2} [(-0.0247)w_1 + (0.5891)w_2 + (0.9462)w_3] = 0.5463 \quad (4.90)$$

and we obtain the cell averaged solution for the whole grid

$$\bar{S}^{P_2} = \begin{bmatrix} 0.5463 & 0.8859 & 0.0012 & -0.8851 & -0.5482 \end{bmatrix} \quad (4.91)$$

Now, by using the inverse Vandermonde matrix, Eq. (4.80), we have

$$\begin{pmatrix} \hat{S}_1 \\ \hat{S}_2 \\ \hat{S}_3 \end{pmatrix} = \begin{pmatrix} 1 & -1 & 1 \\ 1 & 0 & -1/2 \\ 1 & 1 & 1 \end{pmatrix}^{-1} \begin{pmatrix} -0.0247 \\ 0.5891 \\ 0.9462 \end{pmatrix} \quad (4.92)$$

Figure 17 – Solution at $t = 2$.

Source: The author (2018).

the previous equation can be rewritten as

$$\begin{pmatrix} \hat{S}_1 \\ \hat{S}_2 \\ \hat{S}_3 \end{pmatrix} = \begin{pmatrix} 1/6 & 2/3 & 1/6 \\ -1/2 & 0 & 1/2 \\ 1/3 & -2/3 & 1/3 \end{pmatrix} \begin{pmatrix} -0.0247 \\ 0.5891 \\ 0.9462 \end{pmatrix} = \begin{pmatrix} 0.5463 \\ 0.4855 \\ -0.0856 \end{pmatrix} \quad (4.93)$$

Then, the nodal solutions can be recovered, in the following form

$$\begin{pmatrix} S_1^{P_2} \\ S_2^{P_2} \\ S_3^{P_2} \end{pmatrix} = \begin{pmatrix} 1 & -1 & 1 \\ 1 & 0 & -1/2 \\ 1 & 1 & 1 \end{pmatrix} \begin{pmatrix} 0.5463 \\ 0.4855 \\ -0.0856 \end{pmatrix} = \begin{pmatrix} 0.5463 \\ 0.5463 \\ 0.5463 \end{pmatrix} \quad (4.94)$$

in which the first-row value corresponding to the cell average value \bar{S}^{P_2} , that we are looking for. Thus, we obtain a full solution as follows

$$\bar{S}^{P_2} = \begin{bmatrix} 0.5463 & 0.8859 & 0.0012 & -0.8851 & -0.5482 \end{bmatrix} \quad (4.95)$$

In Eqs. (4.91) and (4.95) we show that the average solutions calculate by different methods are essentially the same.

In broad terms, we adopted the Vandermonde strategy as proposed by Hesthaven e Warburton (2008) due to its excellent behavior and robustness to compute L2 projection, which was also used in the stage of the hierarchical limiting process.

4.4 Discretization of the diffusive term

Let us consider the Eq. (3.19) on the horizontal domain Ω , where, for the sake of simplicity only, the gravity effect can be neglected, that is, the dip angle $\theta = 0$. Thus, the

Eq. (3.19) becomes

$$\frac{\phi \partial S_w}{\partial t} = - \left(\underbrace{\frac{\partial f_w}{\partial x} v}_{\text{Advective term}} + \underbrace{\frac{\partial}{\partial x} \left[\lambda_o f_w K(x) \frac{\partial p_c}{\partial x} \right]}_{\text{Diffusive term}} \right) + Q_w \quad (4.96)$$

Due to the distinct nature of the advective and diffusive terms their discretization are then carried out separately. Thus, in Eq. (4.96) the advective term is discretized by using the CPR method and a 1D cell center finite volume method with cell length h_i is employed to discretize the diffusive term, which can be written as (EVJE; FRIIS, 2012)

$$\frac{1}{h_i} \left\{ K_{i+1/2} [f_w \lambda_o]_{i+1/2} \left(\frac{J(S_{i+1})}{\sqrt{K(x_{i+1})}} - \frac{J(S_i)}{\sqrt{K(x_i)}} \right) - K_{i-1/2} [f_w \lambda_o]_{i-1/2} \left(\frac{J(S_i)}{\sqrt{K(x_i)}} - \frac{J(S_{i-1})}{\sqrt{K(x_{i-1})}} \right) \right\} \quad (4.97)$$

with the following arithmetic average for the interface viscous flux

$$\begin{aligned} [f_w \lambda_o]_{i+1/2} &= \frac{f_w(S_i) \lambda_o(S_i) + f_w(S_{i+1}) \lambda_o(S_{i+1})}{2} \\ [f_w \lambda_o]_{i-1/2} &= \frac{f_w(S_i) \lambda_o(S_i) + f_w(S_{i-1}) \lambda_o(S_{i-1})}{2} \end{aligned} \quad (4.98)$$

and permeabilities are computed by using a harmonic average in the following form

$$K_{i+1/2} = \frac{2K_i K_{i+1}}{K_i + K_{i+1}}, \quad K_{i-1/2} = \frac{2K_i K_{i-1}}{K_i + K_{i-1}} \quad (4.99)$$

On the other hand, following the work by (EVJE; FRIIS, 2012), the capillary pressure function, is defined as

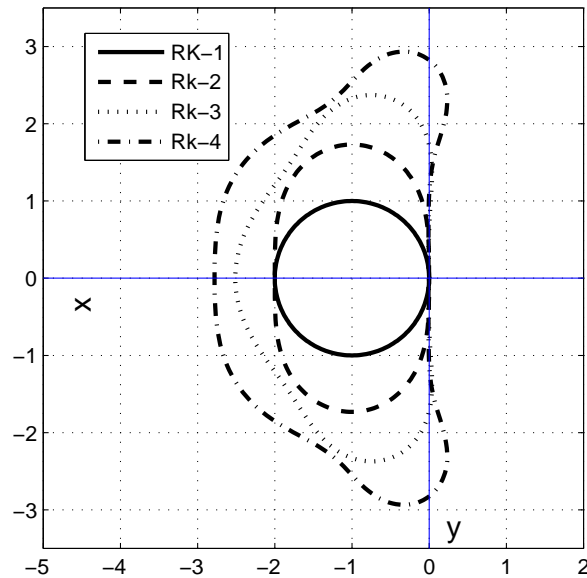
$$p_c(x, S_w) = p_e(x) J(S_w), \quad J(S_w) = \left(S_w^{-1/\zeta} - 1 \right)^{1-\zeta} \quad (4.100)$$

where the J Leverett function is also of van Genuchten type and the entry pressure is given by $p_e = 1/\sqrt{K(x)}$, with $0 < \zeta < 1$.

4.5 Explicit time discretization

In this work, we analyze the spatial discretization only, without taking into account the dispersion and dissipation effects of the time integration.

However, when time-dependent PDEs are solved numerically by high-order methods, an issue that requires careful attention is the use of efficient time marching techniques. For example, one might carry out the time stepping by explicit time marching algorithms such as a first-order forward Euler or TVD-RK (Total variation diminish Runge-Kutta) schemes (GOTTLIEB; SHU, 1998). In principle, by relaxing the order, one can obtain Runge-Kutta methods of a given stage number, with higher stability regions, as depicted in Fig. 18, where

Figure 18 – Stability regions of the Runge-Kutta method in the complex $\Omega\Delta t$ -plane, from 1 to 4 stages.Stability regions of the Runge–Kutta method in the complex $\Omega\Delta t$ -plane.**Source:** Adapted from Trefethen (2000).

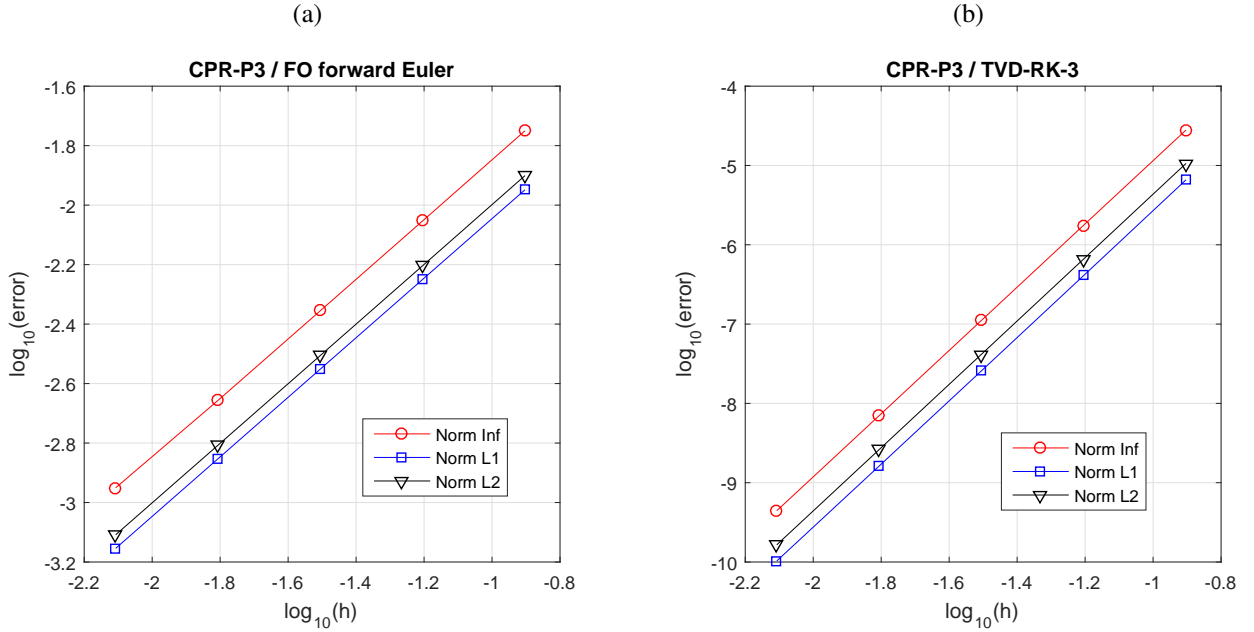
is observed that an increasing of stability region is directly related to the number of stages of the Runge-Kutta method (TREFETHEN, 2000; HIRSCH, 2007), then the added cost in the RK scheme is offset by allowing a larger stable and permissible time step, Δt which is prescribed by the CFL (Courant-Friedrichs-Lewy) condition.

The major drawback such classical algorithms is that the maximum time step tends to be very small. Such restrictively small time steps can be avoided by the use of implicit time marching algorithms, some of which are stable with arbitrarily large time steps, e.g. the second-order backward differencing scheme, which is beyond the scope of this work. However, such schemes require the solution of a nonlinear algebraic system at each time step and consequently, efficient algebraic solvers are a necessity.

It is worthwhile to highlight that in the CFD community, the pattern is usually the same, the employed of high-order schemes in space and high-order TVD-RK methods in time, often leave the global accuracy quite satisfactory. As depicted in Fig. 19 for a linear problem with smooth initial condition, i.e., $S^0 = -\sin(\pi x)$ on $\Omega = [-1, 1]$, show that by using of first-order forward Euler scheme the rate of convergence is reduced, thus, a high-order time discretization is necessary to obtain optimal convergence.

For the flows in porous media case, we agree with several authors in that the high-order approximations in time are not very relevant (DURLOFSKY, 1993; LAMINE, 2009; SOUZA, 2015), besides to deal problems with strong shocks and discontinuities, in which TVD-RK methods must be used with advantage, although this is based on experimental evidence only.

Figure 19 – Rates of spatial convergence from the grid refinement studies using a CPR-P3 spatial reconstructions for the 1D linear wave equation at $t = 2$ with CFL = 0.9 (a) Solution using a first-order forward Euler scheme (b) Solution using a third-order TVD-RK method.



Source: The author (2018).

Due to the good performance of high-order time approximations in other research areas, based on the discussion of the dispersion and dissipation characteristics of higher-order methods, which has been pursued by several authors (HESTHAVEN; WARBURTON, 2008; NOGUEIRA et al., 2010; WANG, 2011), in this work, we continue to use TVD-RK scheme, although it is computationally more expensive than the forward Euler scheme and considering the fact that for particular test problems both time discretizations are equally suitable.

Following the work by (PARK; KIM, 2016), to turn this into a useful approach, we need to understand how we choose a stable Δt for arbitrary values of n , thus we can write an adequate time step as

$$\Delta t = \frac{\text{CFL}}{2n+1} \frac{|\Omega_i|}{|\partial F / \partial S|} \quad (4.101)$$

To complete the discussion of the time discretization techniques, let us write Eq. (4.29) in compact form as

$$\frac{dS_w}{dt} = R(S_w), \quad (4.102)$$

Then, the time integration is performed using an third-order explicit Runge-Kutta method (HIRSCH, 2007; LYRA, 1994) with two intermediate stages to arrive at the t^{q+1} starting from

the t^q . Upper index (1) and (2) refer to intermediate steps in the time marching process.

$$\begin{aligned}
 S_w^{(1)} &= S_w^n + \Delta t R(S_w^q) \\
 S_w^{(2)} &= \frac{3}{4} S_w^q + \frac{1}{4} S_w^{(1)} + \frac{1}{4} \Delta t R(S_w^{(1)}) \\
 S_w^{q+1} &= \frac{1}{3} S_w^q + \frac{2}{3} S_w^{(2)} + \frac{2}{3} \Delta t R(S_w^{(2)})
 \end{aligned} \tag{4.103}$$

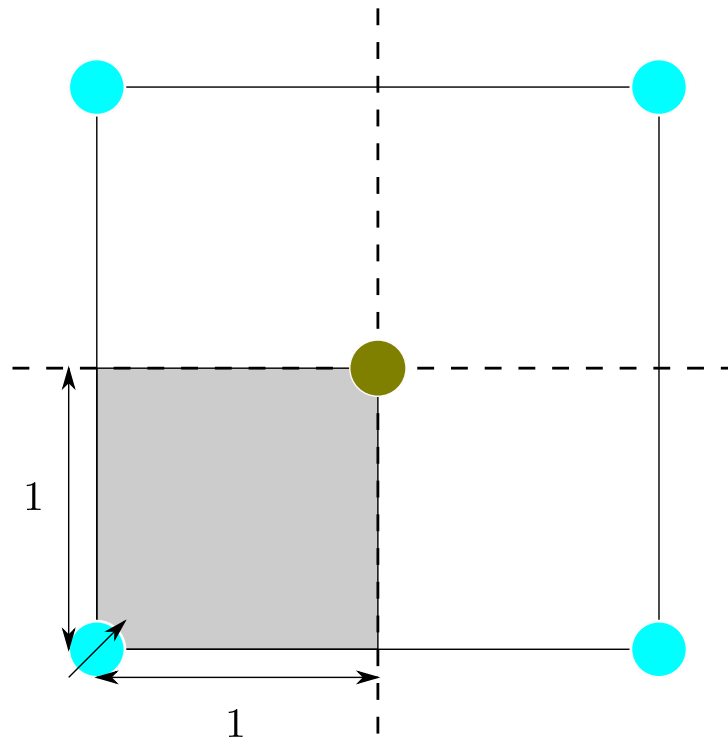
Then, we are able to compute the residual $R(S_w)$ for a given cell saturations S_w using Eq. (4.29) and so calculate S_w^{q+1} using the presented time integration method, which is precisely what we are looking for.

5 NUMERICAL RESULTS

In this chapter several numerical experiments are carried out to verify the theoretical considerations related to the different methods described to solve the equation involved in flow problems in petroleum reservoir modeling. To assess the accuracy and convergence behavior of the CPR methods to solve the transport problem Eq. (4.29), a set of benchmark problems are analyzed, starting from a simple Buckley-Leverett equation to a two-phase flow problem. For all examples a hierarchical MLP strategy to eliminate spurious oscillations around the discontinuities (Park and Kim, 2016), with a Roe-E approximate Riemann solver were used.

For the 2D examples, a classical non-dimensionalized version of a quarter five-spot test problem in a domain $\Omega = [1 \times 1]$ for $\vec{r} \in \mathbb{R}^2$ was employed, represented by the gray-shaded region in Fig. 20. It consists of an injector and a producer placed diagonally at lower left and upper right corners, respectively, opposite to each other in a square domain with no-flow conditions set on all boundaries. Injection is modeled as a source term with constant injection rate $S_w = \bar{S}_w = 1$ on $[\Gamma_I, t]$ at the bottom-left corner and fixed pressure at the producer well $p(\vec{r}, t) = g_P = 0$ on Γ_P at top-right corner.

Figure 20 – Quarter five-spot problem set-up, using a five-spot pattern, with four injection wells on the corners and one production well at the center.



Source: The author (2018).

In general, a Brooks-Corey type relative permeability relation of the form $k_{rw} = S_w^2$ and

$k_{ro} = (1 - S_w)^2$, porosity $\phi = 1$ and the mobility ratio $M = (\mu_o/\mu_w) = 4$ are adopted, for the sake of simplicity only.

To calculate the error in saturation solution, we use the following expression:

$$L_p\text{-error} = \|S_w^{P_n} - \tilde{S}_w\|_{L_p} = \left(\Delta x \sum_{-\infty}^{\infty} |S_w^{P_n(i)} - \tilde{S}_{w(i)}|^p \right)^{1/p} \quad (5.1)$$

with $p = 1, 2$ and $S_w^{P_n}$ being the numerical solution and \tilde{S}_w the semi-analytical solution. The convergence rate on two consecutive grids ($x1$) and ($x2$) was computed by

$$L\text{-rate} \propto \frac{\log(\text{error } x1) - \log(\text{error } x2)}{\log(\Delta x1) - \log(\Delta x2)} \quad (5.2)$$

The values of the required parameters employed in the numerical and semi-analytical computations are listed in Tab. 7. All runs were executed on a Dell laptop machine, with an Intel ® Core™ 2 Duo CPU T6400 @ 2.00 GHz, with 3,0 GB of RAM.

Table 7 – Relevant data used in semi-analytical and numerical computation.

Parameter	Symbol	Unit	Test 6.1	Test 6.2	Test 6.3	Test 6.4	Test 6.5	Test 6.6	Test 6.7	Test 6.8
Domain	Ω	[m]	[0, 300]	$[-1, 1]^2$	$[0, 1]^2$	$[0, 1]^2$	$[0, 1]^2$	$[0, 1]^2$	$[0, 1]^2$	$[0, 1]^2$
Total Velocity	v	[m/s]	3×10^{-7}	–	–	–	–	–	–	–
Water Residual Sat.	S_{wr}	[-]	0.0	0.0	0.0	0.0	0.0	0.0	0.0	0.0
Oil Residual Sat.	S_{or}	[-]	0.0	0.0	0.0	0.0	0.0	0.0	0.0	0.0
Porosity	ϕ	[-]	0.2	1.0	1.0	1.0	1.0	1.0	1.0	1.0
Water Inj. Rate	Q_w	[m ³ /(kg · s)]	0.0	1.0	1.0	1.0	1.0	1.0	1.0	1.0
Mobility Ratio	μ_o/μ_w	[-]	4.0	4.0	4.0	4.0	4.0	4.0	10.0/100.0	4.0
Oil density	ρ_o	[kg/m ³]	780	780	780	780	780	780	780	780
Water density	ρ_w	[kg/m ³]	1,000	1,000	1,000	1,000	1,000	1,000	1,000	1,000

Source: The author (2018).

5.1 MUSCL vs CPR methods

The MUSCL method was originally proposed by Van (LEER, 1979) to obtain a second order approximation. We have decided to use it for comparison purposes because it is very accurate and robust and it has been used in several areas of knowledge, including physics, engineering and petroleum reservoir simulation (SPEKREIJSE, 1987; DURLOFSKY, 1993; BATTEN; LAMBERT; CAUSON, 1996; KIM; CHOI, 2000; DIAZ et al., 2009; DELIS; NIKOLOS, 2013; CONTRERAS et al., 2016).

This test was adapted from (BASTIAN, 1999, p. 94). Considering the problem described by Eq. (4.29). The boundary and initial conditions are given by (BASTIAN, 1999)

$$\begin{aligned} S_w(x, 0) &= S_{wr}, \quad x \in \Omega \\ S_w(0, t) &= 1 - S_{or}, \quad x = 0 \end{aligned} \quad (5.3)$$

solutions were obtained at $t = 1, 500[d]$. A CFL = 0.3 is considered as adopted in Bastian (1999) and the semi-analytical solution was calculated using the characteristic lines method (BASTIAN,

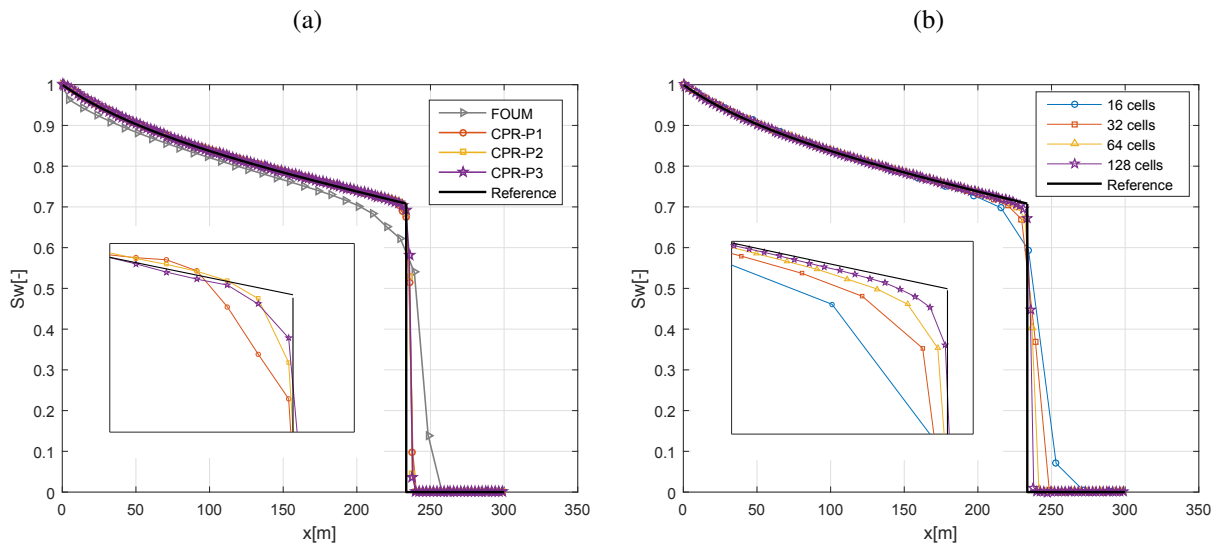
Table 8 – Error and convergence test of the MUSCL-TVD (cell-centered) and the SV/SD/NDG schemes, using second order accuracy.

Method	NDOF	L_1 -error	L_1 -rate	L_2 -error	L_2 -rate
MUSCL	32	9.10×10^{-3}	-	2.80×10^{-2}	-
	64	4.80×10^{-3}	0.94	1.98×10^{-2}	0.50
	128	2.90×10^{-3}	0.73	1.84×10^{-2}	0.11
	256	1.70×10^{-3}	0.78	1.68×10^{-2}	0.13
	512	9.00×10^{-4}	0.92	1.32×10^{-2}	0.35
Average			0.84		0.27
SV/SD	32	1.21×10^{-2}	-	3.53×10^{-2}	-
	64	7.00×10^{-3}	0.79	2.93×10^{-2}	0.27
	128	3.90×10^{-3}	0.86	2.26×10^{-2}	0.37
	256	2.10×10^{-3}	0.87	1.80×10^{-2}	0.33
	512	1.20×10^{-3}	0.85	1.45×10^{-2}	0.31
Average			0.84		0.32
NDG	32	1.01×10^{-2}	-	3.09×10^{-2}	-
	64	5.50×10^{-3}	0.88	1.87×10^{-2}	0.72
	128	3.10×10^{-3}	0.83	1.48×10^{-2}	0.34
	256	1.73×10^{-3}	0.84	1.21×10^{-2}	0.29
	512	0.92×10^{-3}	0.91	0.84×10^{-2}	0.53
Average			0.87		0.47

Source: The author (2018).

1999) and references therein. As shown in Tab. 8, we see that only the approximation order of around $O(h)$ in the L_1 -error and $O(h^{1/2})$ in the L_2 -error can be achieved, since, the solution is discontinuous, with large gradients, which can contaminate the solutions in the smooth region behind the shock and deteriorate the order of accuracy at the point of discontinuity and cause the loss of convergence.

This test case confirms that the numerical schemes considered here, give indeed similar resolution for second order of accuracy. Now, for higher-order approximations, we show the convergence of the water saturation, S_w under both order and cell refinement, to verify the accuracy and high-resolution of the CPR method. For the p-refinement test, we fix the number of cells $\mathcal{N} = 32$ in the grid and increase the order of the polynomial interpolation P_n from $n = 1, \dots, 3$. A time step of $\Delta t = 10^{-4}$ was used to avoid errors that result from the time discretization. In Fig. 21(a), we noticed that, despite the coarse mesh used, the FOU (First-Order Upwind) scheme, solved the problem, but with low accuracy, however, when we vary the polynomial interpolation degree, we observed a significant improvement in behavior of the numerical solution, i.e., the numerical solution shows higher accuracy in the smooth zone behind the shock and does not present spurious numerical oscillations around the discontinuity, hence the numerical solution converges to the semi analytical solution by increasing the degree n of the interpolating polynomial. This test highlights that one can recover a very good solution by using a P_3 approximation, as depicted in a close-up view of Fig. 21(a). Next, we test the h-refinement by fixing $n = 3$ and using four one-dimensional grids, with 16, 32, 64 and 128 cells. To satisfy the stability criterion, the time step is chosen so that the CFL = 0.9. We see from Fig. 21(b) that,

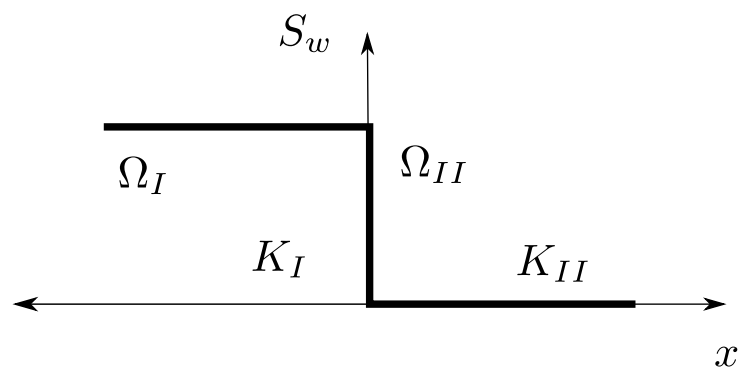
Figure 21 – Buckley Leverett problem for $t=1,500$ days (a) p-refinement and (b) h-refinement.

Source: The author (2018).

the solution does not present any unphysical oscillations, converging appropriately to the semi-analytical solution as we refine the mesh. In the next subsection, we will study the performance of CPR method in the presence of one-dimensional spatial variations in rock permeability field in petroleum reservoirs.

5.2 Two-phase flow in heterogeneous porous media with capillary pressure effect

In this case, adapted from (EVJE; FRIIS, 2012), our goal is to show the performance of our scheme to deal with heterogeneous petroleum reservoirs (In this case a simple heterogeneity, see Fig. 22). Let us consider the Eq. (4.96) on the horizontal domain $\Omega \in [-1, 1]$ where, for the sake of simplicity only, the gravity effect can be neglected, that is, the dip angle $\theta = 0$ and other parameters are listed in Tab. 7.

Figure 22 – Domain $\Omega = \Omega_I \cup \Omega_{II}$.

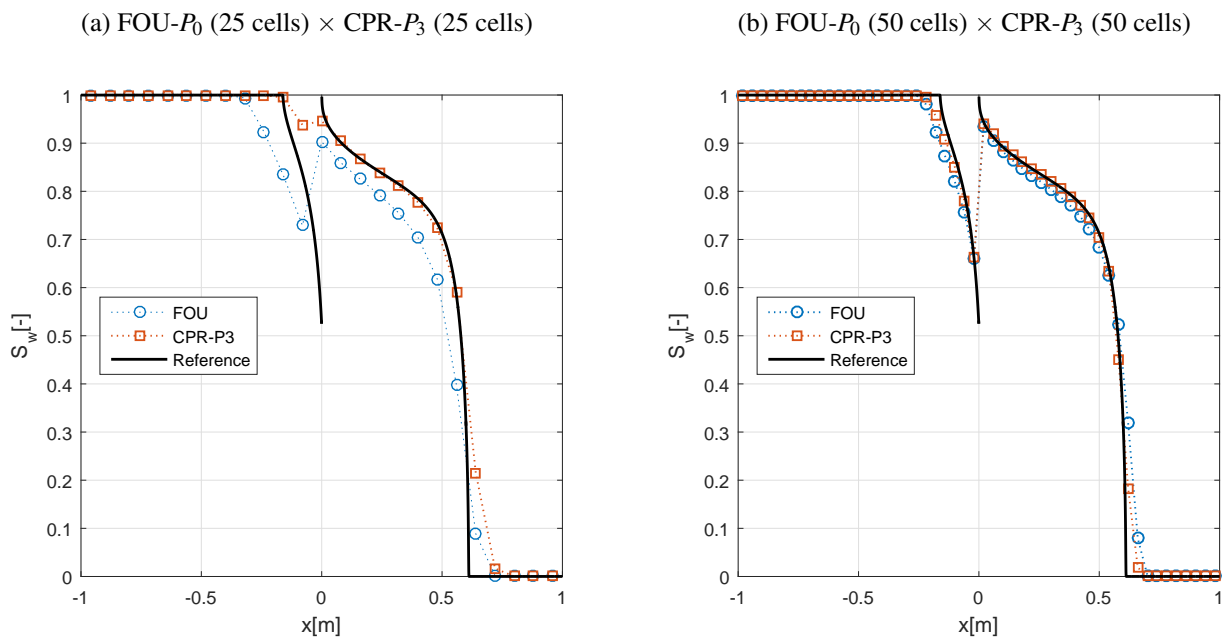
Source: The author (2018).

Initial condition and absolute permeabilities are given by

$$S(x,0) = \begin{cases} 1, & \text{if } x < 0 \\ 0 & \text{if } x > 0 \end{cases}, \quad K(x) = \begin{cases} K_I, & \text{if } x < 0 \\ K_{II} & \text{if } x > 0 \end{cases} \quad (5.4)$$

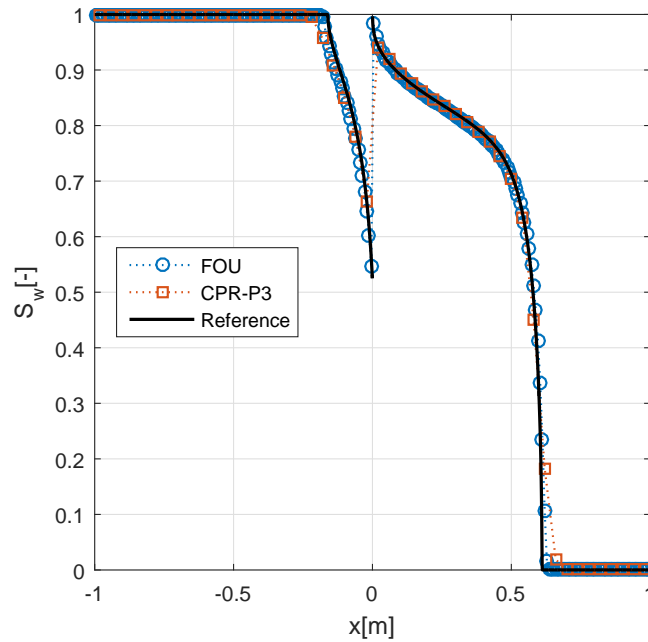
respectively. In the numerical experiments we employed $K_I = 4.2025$, $K_{II} = 0.5625$ and $\zeta = 2/3$. Other parameters are listed in Tab. 7. The results in Fig. 23 show that the CPR solution has less numerical diffusion in comparison with the FOU solution, which decreases as the number of cells is increased, this focuses on the proximity of the solution and the reference lines. Here, the reference solution was computed using a first-order cell-centered finite volume method with 4,000 control volumes, because, currently, there are no analytical solutions available when advection, diffusion, and accumulation terms are all included in the equation. The results with the FOU method with 250 cells and the CPR with 50 cells are comparable (visually), see Fig. 24. with FOU scheme a bit better at peak and shock representation and CPR better on the smooth portions of the solution. Table 9 shows the CPU time performance, which, at first, might suggest that high order methods, that is, high values of n are not really worth considering. A closer look at the results in Tab. 9, however, shows the contrary. Following the work by (HOTEIT; FIROOZABADI et al., 2006), because the results of the FOU (250 cells) and the CPR (50 cells) methods are visually comparable, the (50 cells, P_3) combination, is clearly the fastest. However, note that for the same number of cells, the CPR method is slower than the FOU scheme, partly due to the limiting process and the smaller time step required for values of $n > 0$.

Figure 23 – Two-phase flow in heterogeneous porous media with capillary pressure effect for $t = 0.45$ and $CFL = 0.9$.



Source: The author (2018).

Figure 24 – Two-phase flow in heterogeneous porous media with capillary pressure effect for $t = 0.45$ and $CFL = 0.9$, for FOU- P_0 (250 cells) \times CPR- P_3 (50 cells).



Source: The author (2018).

Table 9 – CPU-time (sec) for different grid sizes and polynomial approximation.

$P_n \setminus \mathcal{N}$	25 cells			50 cells			250 cells		
	DOF	CPU-t	Δt	DOF	CPU-t	Δt	DOF	CPU-t	Δt
FOU- P_0	25	0.39	1.7 E-2	50	2.5	4.2 E-3	250	270.3	1.7 E-4
CPR- P_3	100	3.31	2.4 E-3	200	21.7	6.0 E-4	1000	2650.2	2.4 E-5

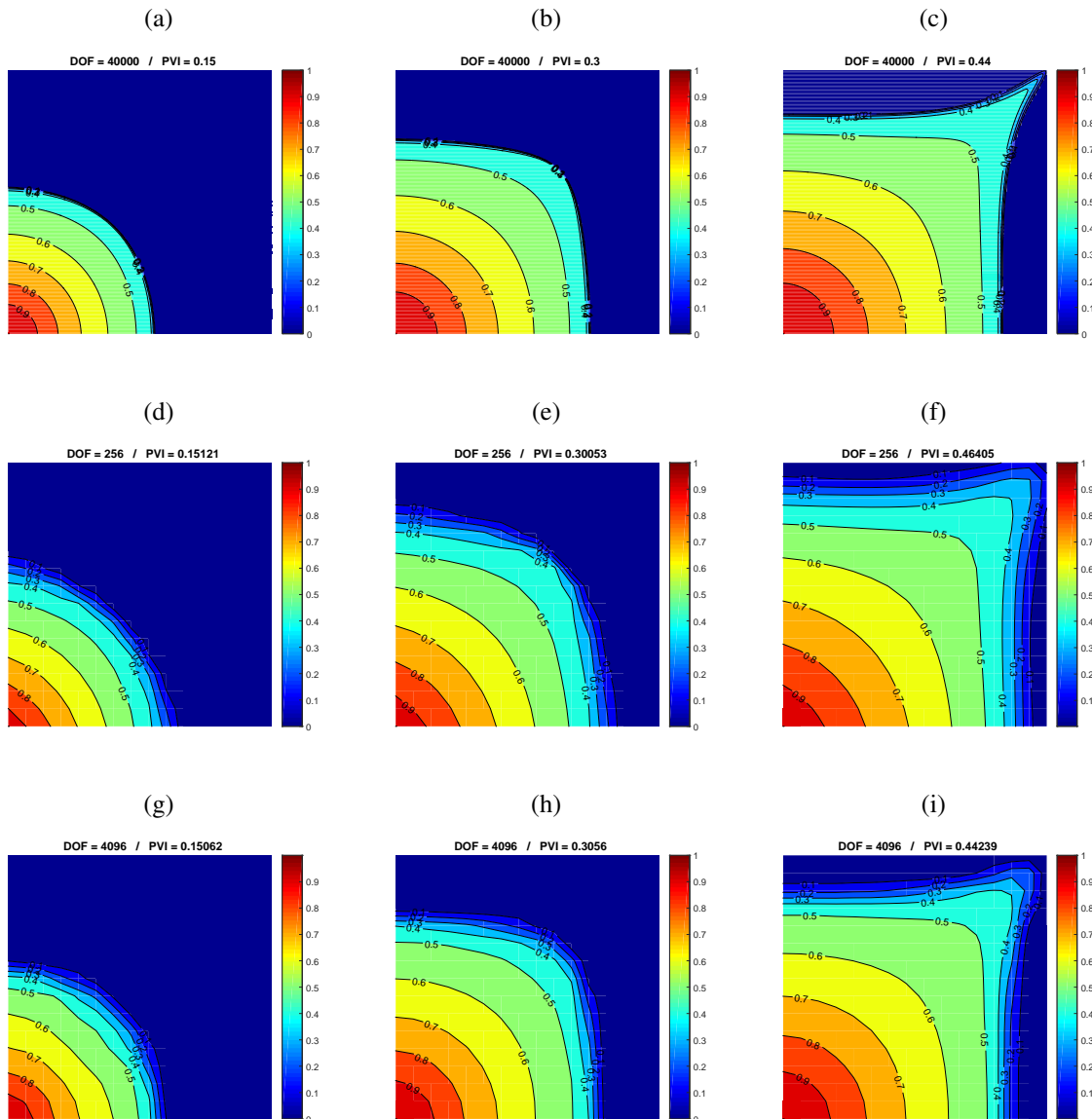
Source: The author (2018).

5.3 Homogeneous quarter of five a spot test

This test case, adapted from (ENGQUIST; LÖTSTEDT; RUNBORG, 2009, p. 16), in which, we use a homogeneous and isotropic permeability field of $\tilde{K} \equiv \tilde{I}$, where \tilde{I} is the second order identity tensor. Here, we test the performance of the solver to determine the resolution of saturation front, when a p-refinement is carried out. This example was computed using a 16×16 quadrilateral mesh, the reference solution was generated via a FOU method using an structured grid with 40,000 CV (control volumes).

The saturation contours plots at different PVI are shown in Fig. 25.

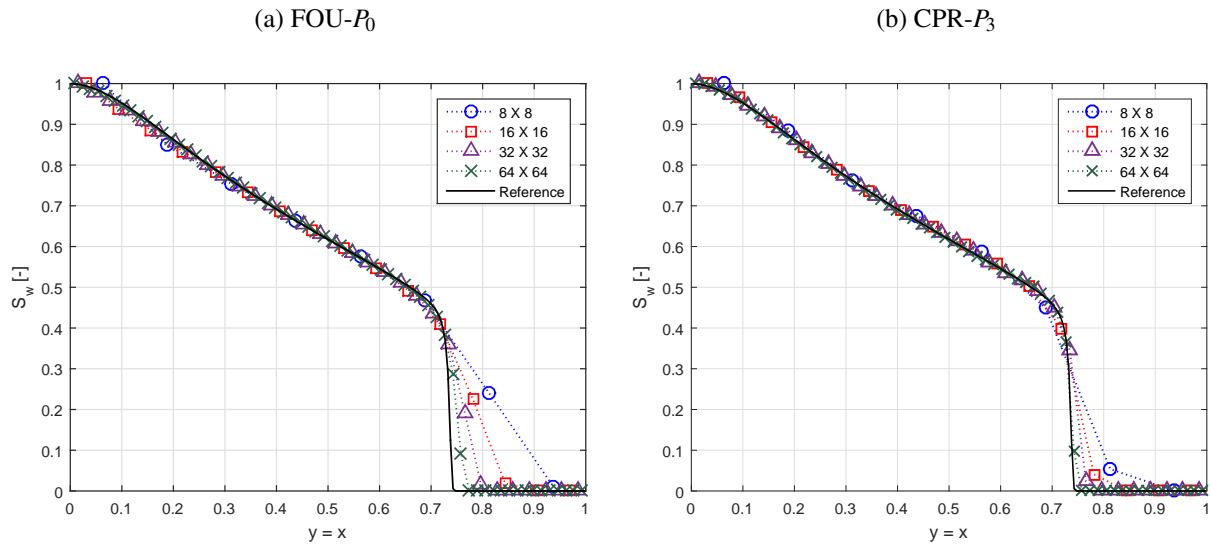
Figure 25 – Saturation profiles at different time levels on a quarter five-spot problem computed on a uniform Cartesian grid up to water-breakthrough in the production well, with CFL = 0.9: (a) to (c) Shows the reference solution, (d) to (f) gives the FOU- P_0 results and (g) to (i) illustrates the CPR- P_3 solutions.



Source: The author (2018).

In Figs. 25(a-c) are illustrated the reference solutions, that correspond to a good approximation of the physical correct saturation front. In Figs. 25 (d-f) is plotted the solution using the FOU method, and in Fig. 25 (g-i) are shown the solutions using the CPR- P_3 method. Inspection of Figs. 25 (d-f) shows that the FOU method solution tends to smear the water front, however, when we vary the polynomial interpolation degree, we observe a significant improvement in behavior of the numerical solution, i.e., the front is solved more sharply by the high-order CPR scheme, showing the convergence of the numerical solution to the reference solution by increasing the degree n of the interpolating polynomial. To achieve a better understanding of the p-refinement process, we plotted the cross-section solutions for different grid sizes in Fig. 26. Regarding the

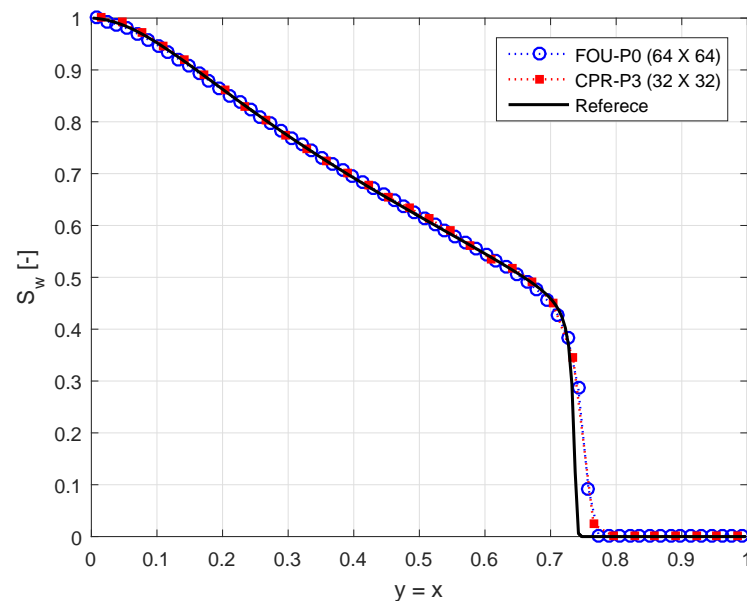
Figure 26 – Cross-section curves for a homogeneous quarter of a five spot problem for quadrangular structured grids up to PVI = 0.3 and CFL = 0.9. (a) FOU method, (b) CPR- P_3 .



Source: The author (2018).

computational performance for this test case, we see in Fig. 27 that the results computed with the FOU method with 64×64 cells are visually comparable to those computed using the CPR with 32×32 cells, where the reference solution was computed via a FOU method for a 200×200 gridding. Thus, for the same accuracy, the $(32 \times 32, P_3)$ combination, is clearly the fastest, as shown in Tab. 10.

Figure 27 – Cross-section comparison for a homogeneous quarter of a five spot problem using a quadrangular structured grid, PVI=0.3 and CFL = 0.9, via a FOU method and CPR- P_3 .



Source: The author (2018).

Table 10 – CPU-time (min) for different grid sizes and polynomial approximation.

$P_n \setminus \mathcal{N}$	8×8		16×16		32×32		64×64	
	DOF	CPU-t	DOF	CPU-t	DOF	CPU-t	DOF	CPU-t
FOU- P_0	64	0.044	256	0.387	1,024	3.284	4,096	30.1
CPR- P_3	1,024	0.201	4,096	1.158	16,384	10.406	65,536	103.7

Source: The author (2018).

These results also confirm that for the same level of accuracy a p-refinement is usually computational cheaper than the h-refinement, i.e.

$$\text{DOF} = \mathcal{N} \times \mathcal{N}_{\text{spc}} \quad (5.5)$$

where \mathcal{N} is the number of cells and \mathcal{N}_{spc} is the total number of local solutions per cell.

Explicitly, we have

$$\begin{aligned} \text{DOF}_{\text{FOU}} &= (64 \times 64) \times 1 = 4,096 \times 1 = 4,096 \\ \text{DOF}_{\text{CPR-}P_3} &= (32 \times 32) \times 16 = 1,024 \times 16 = 16,384 \end{aligned}$$

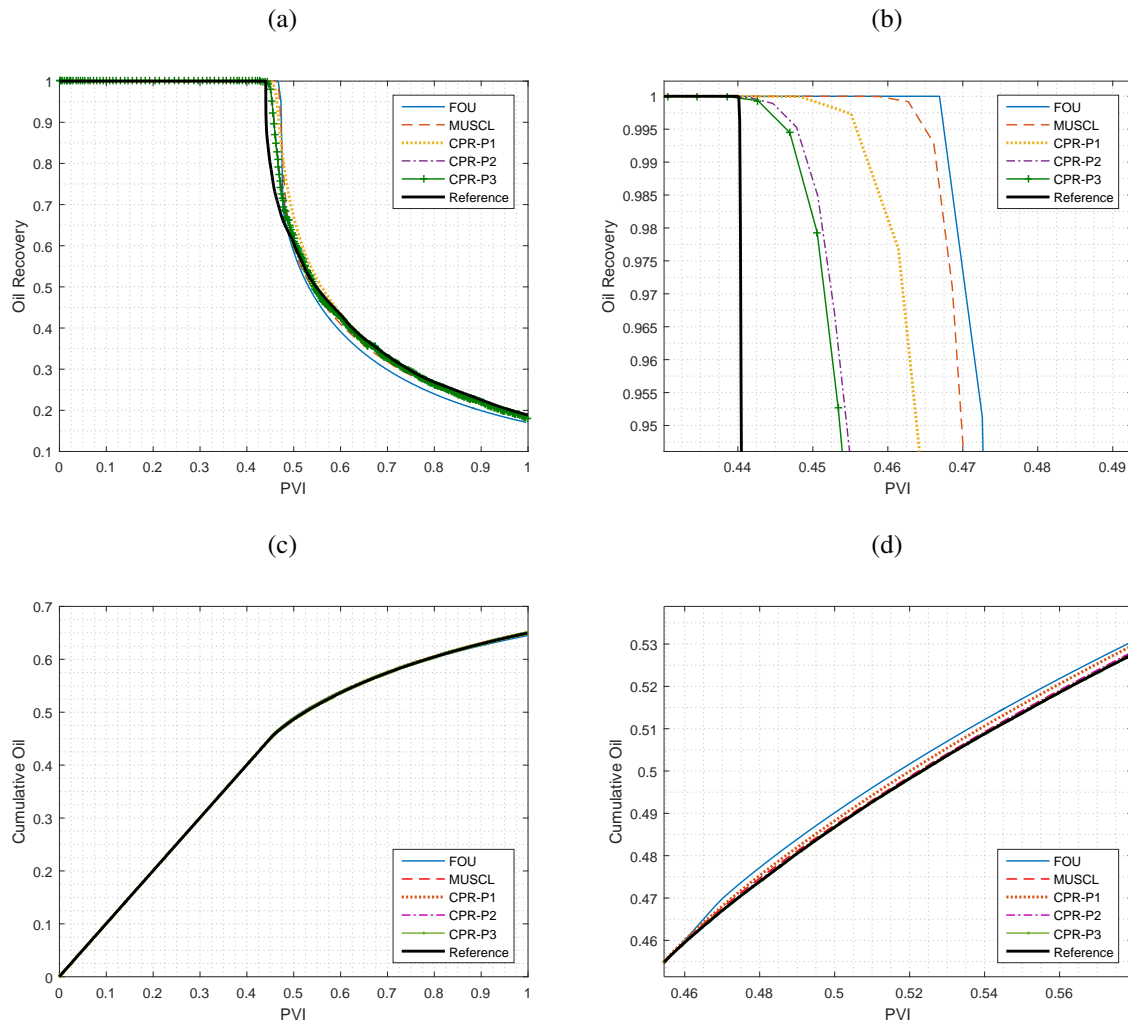
see, Tab. 10.

It is worth emphasizing that the solutions presented in Fig. 27 were computed by a simultaneous h-p combination up to the desired accuracy, which is naturally not easy to estimate a priori, and that other combinations certainly are possible, but the above results are an useful guideline to determine the computational performance requirements for this particularly interesting case.

Finally, let us now consider the production curves as depicted in Fig. 28. In Fig. 28 (a and b) we see the convergence study for the oil production curves. We can clearly see that, when we use the FOU method there is a delay of the water breakthrough, while the higher order methods are far less affected by the diffusion effects, even though, in this case, the CPR- P_1 to produce more accurate solutions than the MUSCL approach.

As illustrated in Fig. 28 (c and d) all methods produce cumulative oil curves that are close to each other even though all higher order methods produce slightly better solutions than the FOU method.

Figure 28 – Production curves for a homogeneous quarter of a five spot problem for 16×16 quadrangular structured grid, PVI=1.0 and CFL = 0.9, using a FOU method, MUSCL, CPR- P_1 to CPR- P_3 (a) Oil-recovery (b) Close-view (c) Cumulative oil (d) Close-view.

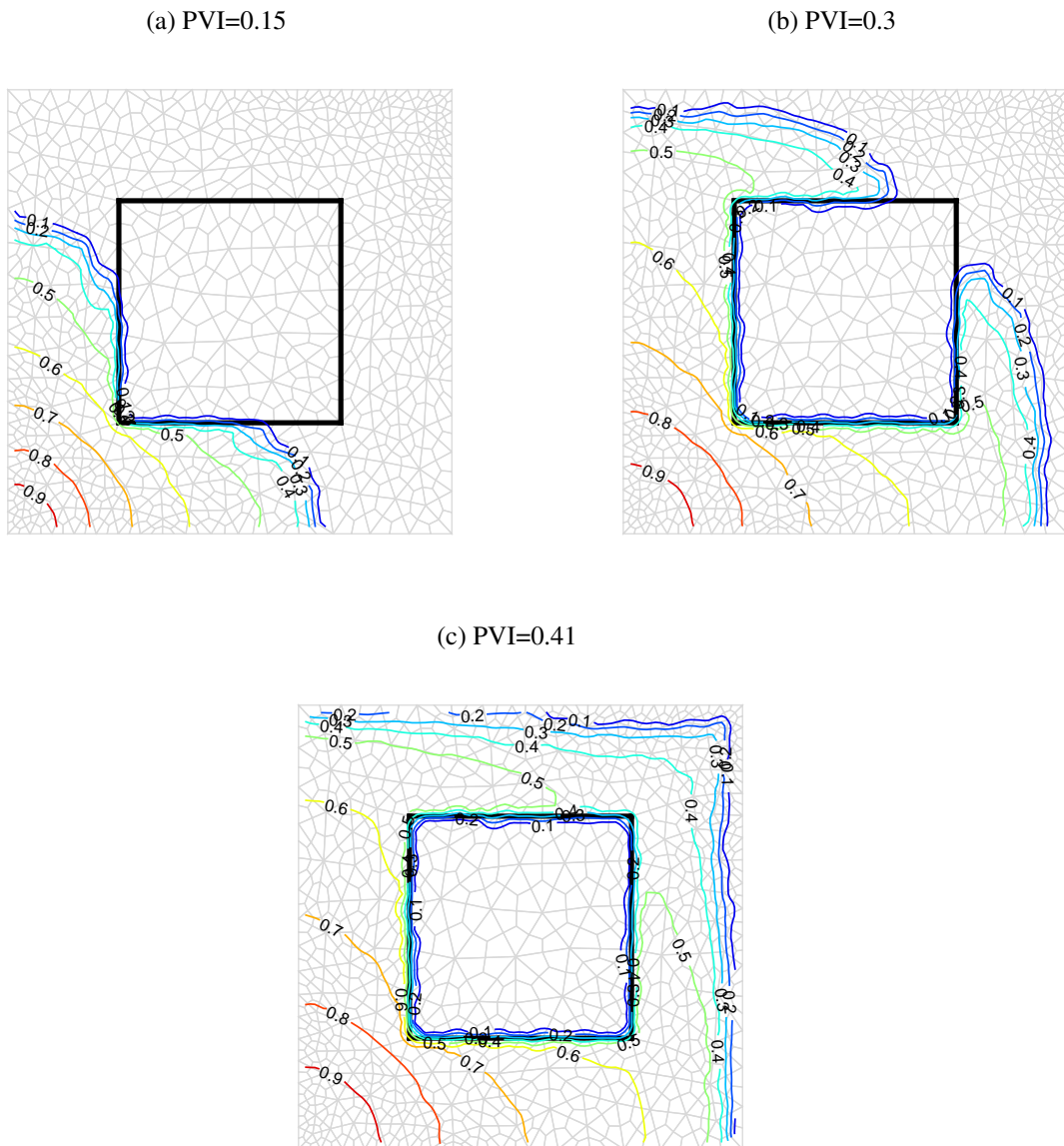


Source: The author (2018).

5.4 Quarter of a five spot with a low-permeability region

Next, we study the performance of CPR method in the presence of spatial variations in rock permeability field in petroleum reservoirs. This test case, adapted from (HELMIG, 1997; CARVALHO, 2005; SRINIVASAN; LIPNIKOV, 2013), includes a flow problem in a discontinuous isotropic permeability field, in which there is a quadrangular region inside the domain with low permeability $\tilde{K} = 10^{-6}I$, as shown in Fig. 29. The solid black lines show the boundaries of the low permeability region, and in the rest of the domain the value of the isotropic permeability is $\tilde{K} = I$. With respect to the computational discrete domain a unstructured quadrilateral mesh with 1,158 cells is used and the reference solution was computed via FOU scheme using an unstructured mesh with 4,560 CVs. The key idea of this test is to show that a correct velocity field does not allow non-physical effects. Here we can notice that the

Figure 29 – Saturation profiles for different time levels on a quarter five-spot problem with a low-permeability region computed on an unstructured grid with 1,158 cells, up to water-breakthrough in the production well, using a P_3 degree polynomial and CFL = 0.9.

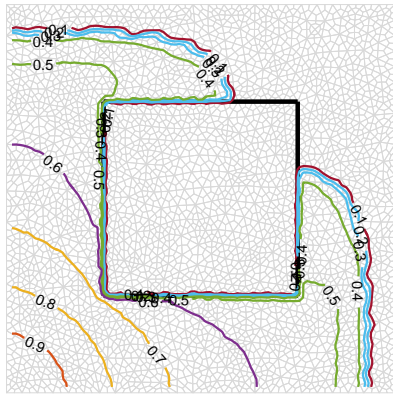


Source: The author (2018).

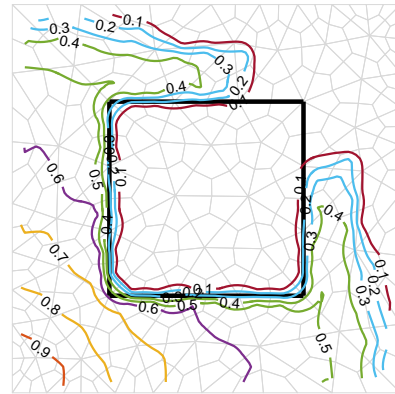
saturation front computed from the aforementioned velocity field follows the correct faster flow-path without getting stuck, or cross, in the low permeability zone, as expected, since the fluids will tend to flow into zones associated with highest permeability formations, thereby generally avoiding any “barrier” or low permeability zone inside the domain. Additionally, other discretization techniques suitable for solving the same test has been compared in Fig. 30. We note that as the polynomial degree increases the high-order methods, such as, MUSCL and CPR- P_{1-3} schemes provides a resolution sufficient to capture the strict discontinuity in the permeability distribution. With the FOU method, the low permeability zone is captured, but with

Figure 30 – Comparison between low-order and high-order methods for a heterogeneous quarter of five a spot problem with low-permeability region in domain using 330 CVs and at PVI = 0.3.

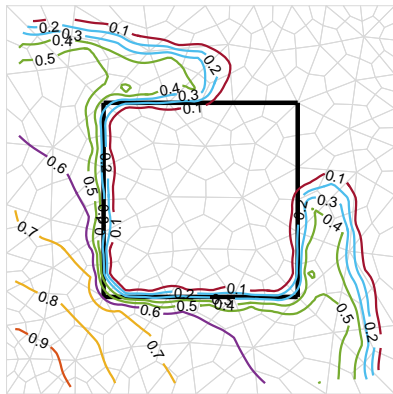
(a) Reference, 4,560 CVs



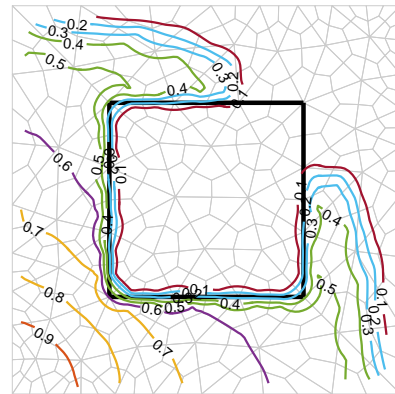
(b) FOU method



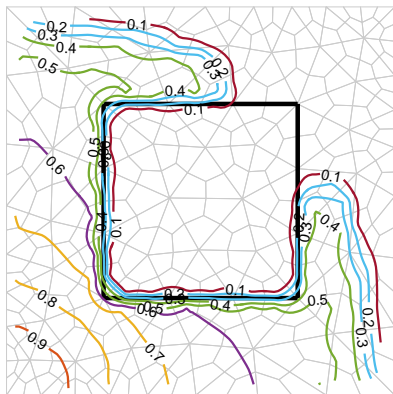
(c) MUSCL method



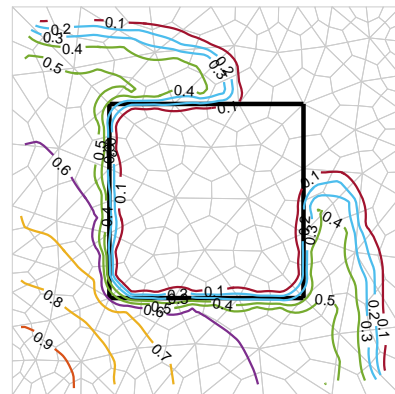
(d) CPR- P_1



(e) CPR- P_2



(f) CPR- P_3



Source: The author (2018).

some amount of numerical diffusion. In contrast, differences between the saturation profiles obtained with MUSCL method and the CPR scheme, as compared with the reference solution, we note that the CPR method significantly improves the resolution of the saturation front, whereas, for the CPR- P_{1-3} method, there are minor differences, since, in non-smooth regions, close to low permeability region, an h-refinement is better suited, as shown in Fig. 29 where the test was carried out using the CPR- P_3 method on a more refined unstructured grid with 1,158 cells.

5.5 Heterogeneous and anisotropic quarter of five-spot test

This test case, adapted from (EDWARDS, 2006, p. 1,071). In order to test the accuracy of the water saturation solution, a h-p test is carried out. Here, we use an anisotropic and heterogeneous domain with no-flow boundaries, which consisted of four identical “barriers” of low (10^{-6}) permeability aligned in the shape of a cross. The remaining of the domain was divided into four quadrants, in which, we have a diagonal permeability tensor \tilde{K}_1 in the lower left and top right quadrants and a full permeability tensor \tilde{K}_2 is imposed in the lower-right and upper left quadrants, in the following form

$$\tilde{K}_1 = \begin{bmatrix} 1 & 0 \\ 0 & 1 \end{bmatrix} \quad \text{and} \quad \tilde{K}_2 = \begin{bmatrix} 5 & 4 \\ 4 & 5 \end{bmatrix}$$

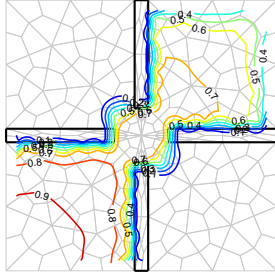
The water saturation contours for the reference solution are shown in Fig. 31 (d), which correspond to the expected physical behavior, i.e., the flow exits the lower left region, it enters the top right quadrant of the domain like a in the usual quarter five-spot configuration, and no-flow in the remain quadrants, which is partly induced by the effect of the full tensor in lower-right and upper left regions and the low-permeability barriers that force the flux to bend significantly around the obstacles. We first consider the use of an h-refinement, as depicted in Figs. 31 (a-c), where, the results are qualitatively better by modifying the element size.

Given the numerical challenges introduced by this test, it seems natural that a h-p combination should result in improved accuracy. This is confirmed by the results in Figs. 31 (e-g), where we show a simultaneous h-p refinement.

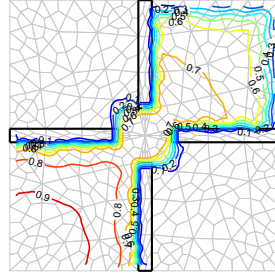
In particular, the CPR (1,122 CVs, P_3) combination provides clearer resolution of flow close to the low-permeability barriers with less amount of flow into the no-flow regions (lower

Figure 31 – Comparison between low-order and high-order methods for a heterogeneous quarter of five a spot cascade problem, up to water-breakthrough in the production well, CFL = 0.9.

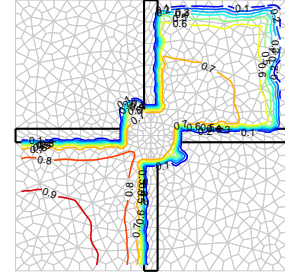
(a) FOU method, 276 CVs



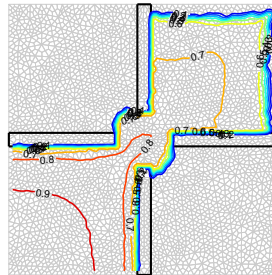
(b) FOU method, 540 CVs



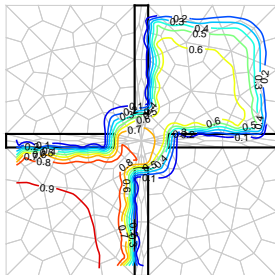
(c) FOU method, 1,122 CVs



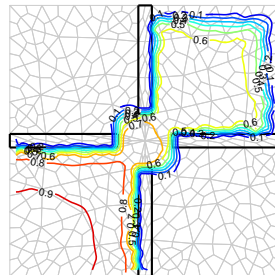
(d) Reference, 4,812 CVs



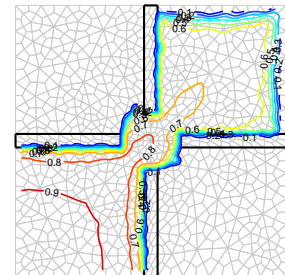
(e) CPR- P_1 , 276 CVs



(f) CPR- P_2 , 540 CVs



(g) CPR- P_3 , 1,122 CVs



Source: The author (2018).

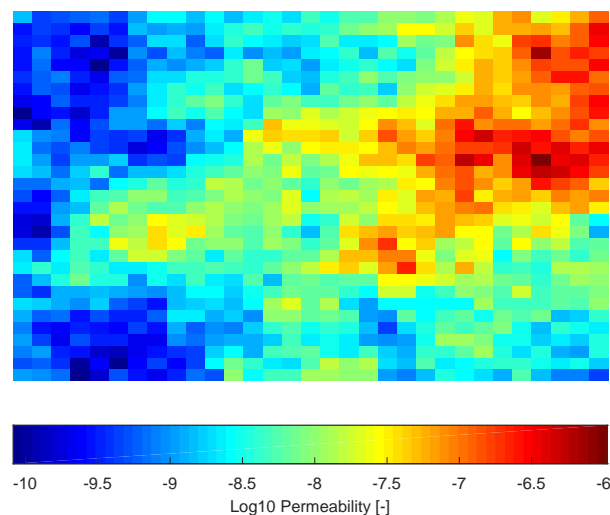
right and upper left quadrants) in this problem, when compared to the other h-p combinations.

5.6 Isotropic and highly heterogeneous porous media

This test case was adapted from (HÆGLAND et al., 2006, p. 8). In this example, we employ an interesting test case that deals with more realistic reservoir medium. Here, we used a 32×32 permeability field from slice 14 of SPE10 test case, model 2, see Fig. 32 and <http://www.spe.org/csp/datasets/set02.htm>.

This permeability field turns out to be challenging, from the numerical viewpoint. For this reason, we use this test case to assess the quality of the water saturation solution on a isotropic and highly heterogeneous porous media. The water saturation contours at different values of PVI are shown in Fig. 33.

Figure 32 – \log_{10} permeability field, layer 14.

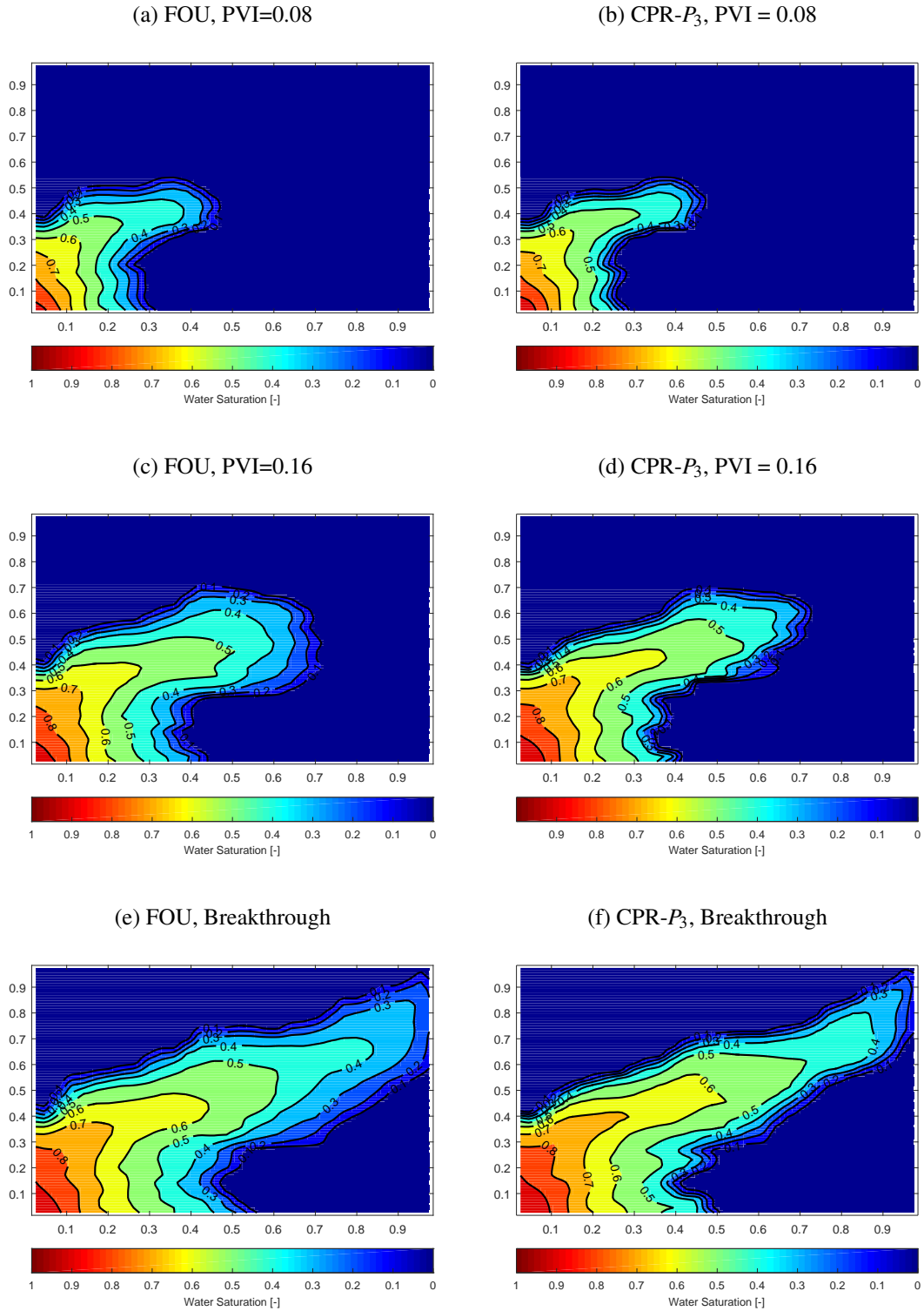


Source: The author (2018).

It is important to note that the water saturation solutions obtained using the CPR method, are physically reasonable, i.e, they avoid the low permeability region, and normally will seek high permeability zones, following the correct faster flow-path. On the other hand, to see better the effect of numerical diffusion, the black lines in Figs. 33 show the contour lines.

Here, we note that the CPR solution has less numerical diffusion in comparison with the FOU solution, this focuses on the proximity of the contour lines, the closer the contour lines (to each other) the corresponding solution produces less numerical diffusion.

Figure 33 – Saturation profiles at different values of PVI for the layer 14 of the SPE-10 model, using 1024 CVs and CFL = 0.9.

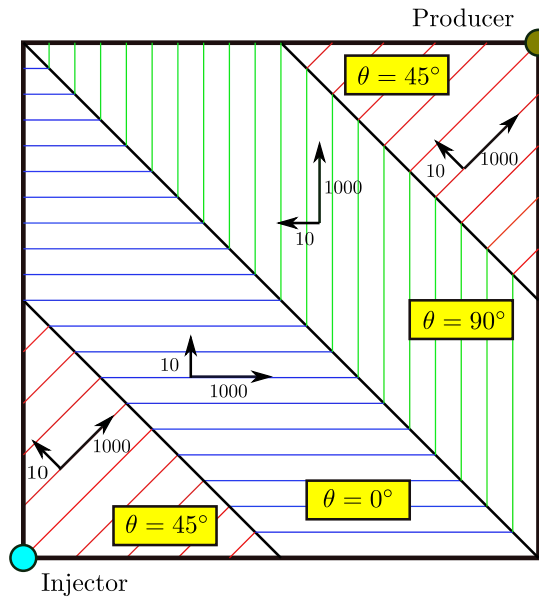


Source: The author (2018).

5.7 Discontinuous full tensor with a high anisotropy ratio

To explore the ability of the CPR to produce a correct solution for anisotropic permeability field, we will present the model problem as in Fig. 34, which was adapted from (NIKITIN; TEREKHOV; VASSILEVSKI, 2014).

Figure 34 – Heterogeneous reservoir with a discontinuous full tensor with a high anisotropy ratio.



Source: Adapted from Nikitin, Terekhov e Vassilevski (2014).

The discontinuous permeability tensor is anisotropic and can be defined as

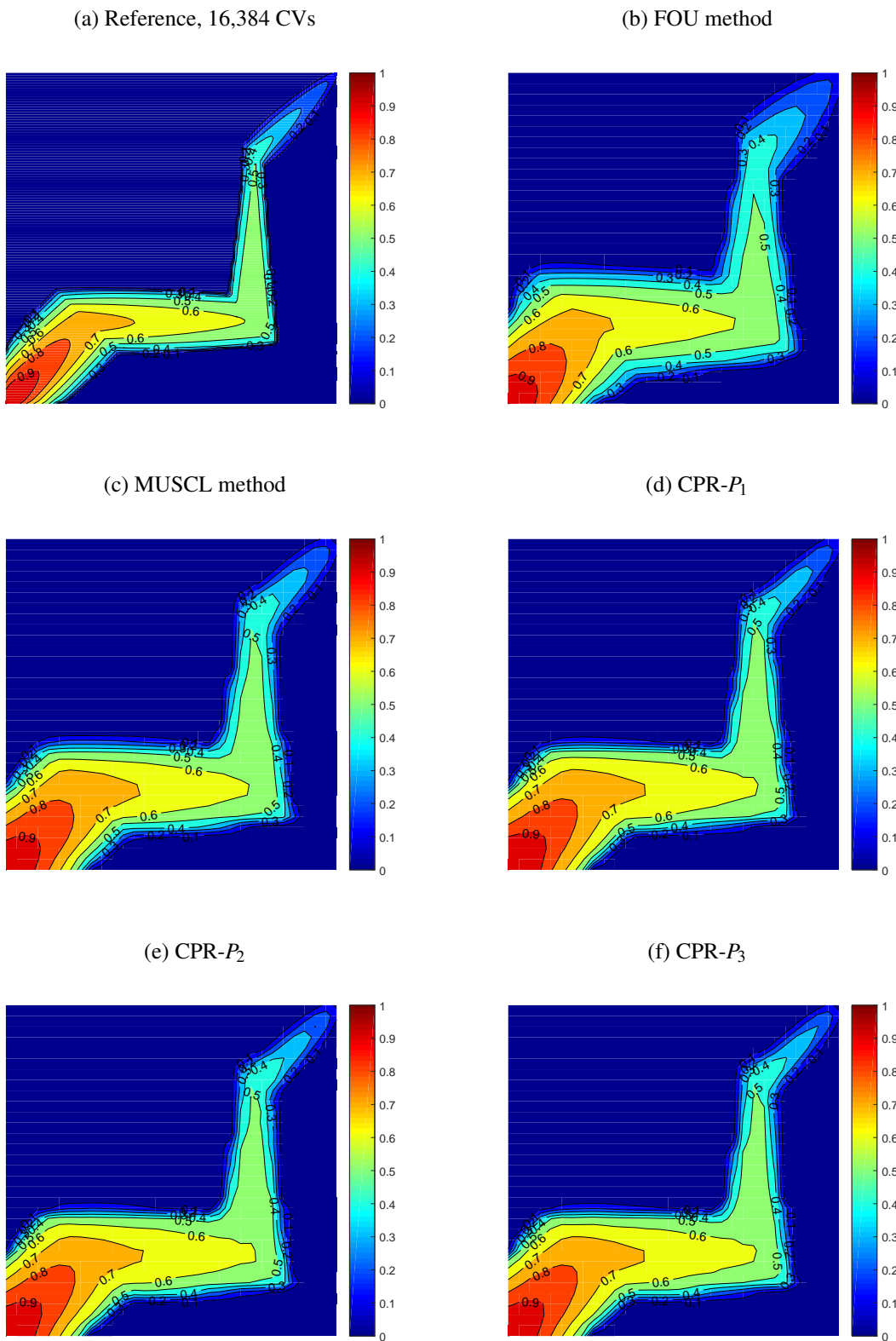
$$\underset{\sim}{K} = \begin{bmatrix} \cos \theta & -\sin \theta \\ \sin \theta & \cos \theta \end{bmatrix} \begin{bmatrix} 1000 & 0 \\ 0 & 10 \end{bmatrix} \begin{bmatrix} \cos \theta & \sin \theta \\ -\sin \theta & \cos \theta \end{bmatrix} \quad (5.6)$$

Figure 34 shows the spatial distribution of the permeability field, where the computational domain is divided into four separate regions with distinct anisotropic behavior, which the angle θ is equal to 45° in the bottom left and upper right parts of the domain and alternate between 0° and 90° in the central region.

In this test, we performed a p-refinement through increasing of degree polynomial from $n = 0, \dots, 3$, on a Cartesian grid of size 32×32 at PVI = 0.16. The saturation profiles are illustrated in Fig. 35. The computational results compared with the reference solution which was computed with the FOU method on 128×128 gridding confirm that the low and high-order methods coupled to MPFA-D scheme clearly honor the domain heterogeneity and anisotropy. However, we also note that with the FOU method, the channel flow with staircase shape is captured but with some amount of numerical diffusion.

Regarding high-order methods, there are small fundamental differences. While the behavior of the CPR-P1 method is very similar to that of the MUSCL method, although the CPR-P1 method produces solutions with much less spreading than the MUSCL scheme, this

Figure 35 – Comparison between low-order and high-order methods for an anisotropic medium in a quarter of five a spot configuration, using a 32×32 structured mesh at $PVI = 0.16$.



Source: The author (2018).

is not surprising since the degree of freedom (DOF) of the CPR-P1 scheme is 4 times as many as the MUSCL scheme. In contrast, we also note that the differences between the CPR method with the approximation of order 2 to 4 are small.

5.8 Grid orientation effect test using a adverse mobility ratio

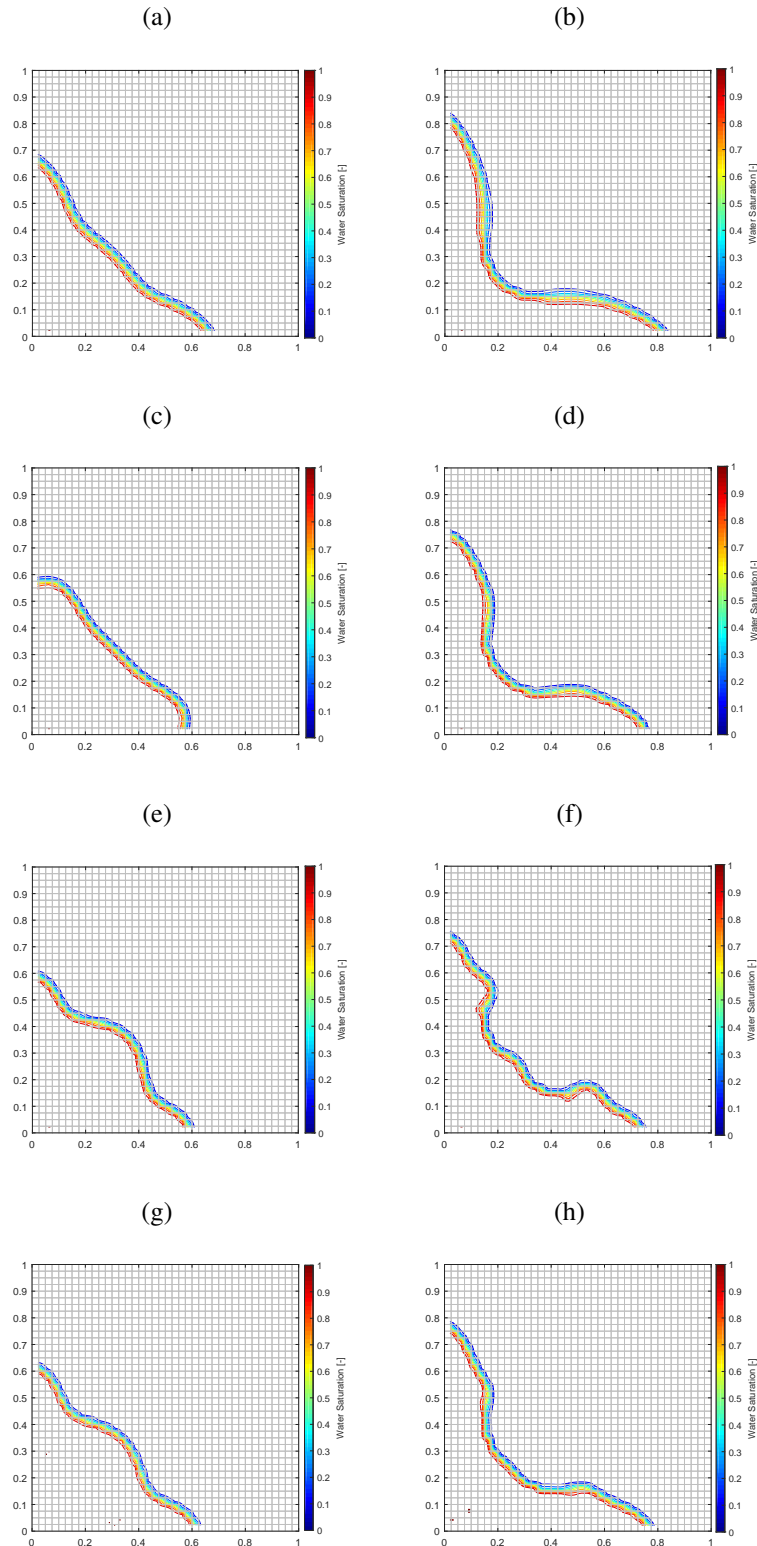
In order to show the behavior of the CPR scheme in a adverse case, the following test is conducted.

Following the work by Yanosik e McCracken (1979) the fractional flux function is defined as $F = S_w^2$ for piston type-displacement. A particularly interesting case is that of $M \geq 1$, corresponding to adverse mobility ratios, as it is characterized by the incorporation of strong discontinuities, i.e., discontinuous displacement fronts. Figure 36 shows water saturation contours computed on a 40×40 diagonal grid.

As depicted in Fig. 36 all the standard discretizations fail to solve this classic test i.e., the standard approximations produce unrealistic solutions and a suitable multidimensional approach should be used to overcome this problem. We refer the interested reader to (SOUZA, 2015) and the references therein for more details.

We do not elaborate on the details of numerical methods used to deal with multidimensional flux, as they are beyond the scope of this study.

Figure 36 – Saturation contours for a homogeneous quarter of a five spot problem for 40×40 quadrangular structured (diagonal) grid, PVI=0.2 CFL = 0.9 and a adverse water/oil mobility ratio $M = 10$ and $M = 100$ first and second column, respectively, using (a-b) FOU method, (c-d) MUSCL, (e-f) CPR- P_1 and (g-h) CPR- P_3 .



Source: The author (2018).

6 CONCLUSIONS AND FUTURE WORK

In this chapter we summarize the key conclusions and contributions of the present work.

6.1 Conclusions

The first original contribution made by this work was to review and compare different finite volume schemes, such as FOU and MUSCL methods, against the CPR scheme for solving the one-dimensional two-phase flow of oil and water in porous media.

The solutions obtained by CPR showed to be in excellent agreement with both numerical and semi-analytical results. Furthermore, the results obtained were indicative that the current method can yield solutions with similar resolution at a lower computational resource usage than traditional FV k -exact schemes up to P_1 , by using an adequate h-p combination, as shown in the two-phase flow in heterogeneous porous media with capillary pressure effect solution case compared to the FOU scheme.

In general, the advantage of the very high order CPR approach over FOU method is a dramatic reduction of the smearing close to shocks, and a better accuracy in the smooth regions.

The second original contribution made by this work was to develop a methodology for solving the governing equations of 2D two-phase incompressible flow in petroleum reservoirs. In this methodology, the two governing PDEs, i.e., the pressure and saturation equations were solved by MPFA-D and CPR methods, respectively, in a segregated manner by using IMPES and an adequate interpolation of lowest order Raviart-Thomas interpolation, RT_0 , for the density flux provided by pressure solver, to calculate the nodal values of the total velocity.

In brief, we can highlight the following:

1. CPR method has produced very good results, which are physically reasonable for both homogeneous and heterogeneous, isotropic or anisotropic porous media on structured and unstructured quadrangular grids.
2. The results obtained were indicative that the CPR method can yield solutions with similar resolution at a lower computational resource usage than traditional FV k -exact schemes up to P_1 , by using an adequate h-p combination, as shown in the homogeneous quarter of a five-spot solution case compared to the FOU scheme.
3. Regarding the behavior of the CPR scheme in adverse cases, it suggests that high order approximations may suffer from problems associated with the grid orientation effect, like their low-order counterparts and some technique, such as the multidimensional flux computation should be used to overcome this problem.

4. Finally, we can then conclude that coupling the pressure solvers based on FV methods to very high order nodal formulations through the total reconstructed velocity field using an IMPES approach is feasible.

In general, the CPR method seems suitable for Petroleum Reservoir Simulation, in the sense, that it is compact, from an implementation point of view, extensible to high-order approximations and relatively computationally efficient.

Regarding the coupling with the pressure solver, it opens the possibility to obtain very high order saturation profiles to the two-phase flow simulation using also a pressure equation calculated with any advanced discretization scheme, that provides discrete density fluxes at the cell edges.

6.2 **Future work**

- The results in this thesis show that different combinations of h-p via the CPR method can be performed successfully. Developing and implementation of an h-p adaptive methodology for the coupled solver would be an important step to enhance the accuracy of the solution calculated by the CPR method.
- Correct computation of the velocity field is very important for the CPR method. A possible approach to improve the velocity field accuracy could be to approximate it by the first order BDM (Brezzi-Douglas-Marini) interpolation.
- Furthermore, regarding the mathematical model, the CPR algorithm should be investigated further and extended to multiphase flow and 3D models.

REFERENCES

- AARNES, J. E.; GIMSE, T.; LIE, K.-A. An introduction to the numerics of flow in porous media using matlab. In: *Geometric modelling, numerical simulation, and optimization*. [S.l.]: Springer, 2007. p. 265–306. 27
- AAVATSMARK, I. et al. Discretization on unstructured grids for inhomogeneous, anisotropic media. part i: Derivation of the methods. *SIAM Journal on Scientific Computing*, SIAM, v. 19, n. 5, p. 1700–1716, 1998. 24
- AAVATSMARK, I. et al. Discretization on unstructured grids for inhomogeneous, anisotropic media. part ii: Discussion and numerical results. *SIAM Journal on Scientific Computing*, SIAM, v. 19, n. 5, p. 1717–1736, 1998. 24
- AAVATSMARK, I.; EIGESTAD, G. Numerical convergence of the mpfa o-method and u-method for general quadrilateral grids. *International journal for numerical methods in fluids*, Wiley Online Library, v. 51, n. 9-10, p. 939–961, 2006. 24
- ABEELE, K. Van den; LACOR, C.; WANG, Z. J. Short note: On the connection between the spectral volume and the spectral difference method. *Journal of Computational Physics*, Academic Press Professional, Inc., v. 227, n. 2, p. 877–885, 2007. 44
- ABGRALL, R. Residual distribution schemes: current status and future trends. *Computers & Fluids*, Elsevier, v. 35, n. 7, p. 641–669, 2006. 25
- ABGRALL, R.; LARAT, A.; RICCHIUTO, M. Construction of very high order residual distribution schemes for steady inviscid flow problems on hybrid unstructured meshes. *Journal of Computational Physics*, Elsevier, v. 230, n. 11, p. 4103–4136, 2011. 25
- ABGRALL, R.; MEZINE, M. Construction of second order accurate monotone and stable residual distribution schemes for unsteady flow problems. *Journal of Computational Physics*, Elsevier, v. 188, n. 1, p. 16–55, 2003. 25
- ARNOLD, D. N. et al. Unified analysis of discontinuous galerkin methods for elliptic problems. *SIAM journal on numerical analysis*, SIAM, v. 39, n. 5, p. 1749–1779, 2002. 26
- AZIZ, K.; SETTARI, A. *Petroleum reservoir simulation*. [S.l.]: Applied Science Publishers London, 1979. v. 476. 31
- BARTH, T. J.; FREDERICKSON, P. O. Higher order solution of the Euler equations on unstructured grids using quadratic reconstruction. *AIAA paper*, v. 90, p. 0013, 1990. 25
- BASTIAN, P. *Numerical computation of multiphase flows in porous media*. Tese (Doutorado) — Ph. D. thesis, Universitat Kiel, Kiel, 1999. 26, 65, 66
- BASTIAN, P. Higher order discontinuous galerkin methods for flow and transport in porous media. In: *Challenges in Scientific Computing-CISC 2002*. [S.l.]: Springer, 2003. p. 1–22. 26
- BASTIAN, P. A fully-coupled discontinuous galerkin method for two-phase flow in porous media with discontinuous capillary pressure. *Computational Geosciences*, Springer, v. 18, n. 5, p. 779–796, 2014. 26

- BATTEN, P.; LAMBERT, C.; CAUSON, D. Positively conservative high-resolution convection schemes for unstructured elements. *International Journal for Numerical Methods in Engineering*, Wiley Online Library, v. 39, n. 11, p. 1821–1838, 1996. 25, 65
- BROOKS, R. H.; COREY, A. T. Hydraulic properties of porous media. *Hydrology Papers, Colorado State University*, n. March, 1964. 31
- CARVALHO, D. K. d. *Uma Formulação do Método dos Volumes Finitos com Estrutura de Dados por Aresta para a Simulação de Escoamentos em Meios Porosos*. Tese (Doutorado) — Tese de Doutorado, Universidade Federal de Pernambuco (UFPE), Recife, in Portuguese., 2005. 27, 29, 34, 73
- CHAVENT, G.; JAFFRÉ, J. *Mathematical models and finite elements for reservoir simulation: single phase, multiphase and multicomponent flows through porous media*. [S.l.]: Elsevier, 1986. v. 17. 26
- CHEN, Q.-Y. et al. Enriched multi-point flux approximation for general grids. *Journal of Computational Physics*, Elsevier, v. 227, n. 3, p. 1701–1721, 2008. 24
- CHEN, Z.; HUAN, G.; MA, Y. *Computational methods for multiphase flows in porous media*. [S.l.]: SIAM, 2006. v. 2. 34
- CHOI, B.-J. et al. A spectral finite-volume method for the shallow water equations. *Monthly weather review*, v. 132, n. 7, p. 1777–1791, 2004. 26
- CLAIN, S.; DIOT, S.; LOUBÈRE, R. A high-order finite volume method for systems of conservation laws—multi-dimensional optimal order detection (mood). *Journal of computational Physics*, Elsevier, v. 230, n. 10, p. 4028–4050, 2011. 25
- COCKBURN, B.; HOU, S.; SHU, C.-W. The Runge-Kutta local projection discontinuous Galerkin finite element method for conservation laws IV: The multidimensional case. *Math. Comp*, v. 54, n. 190, p. 545–581, 1990. 25
- COCKBURN, B.; LIN, S.-Y.; SHU, C.-W. TVB Runge-Kutta local projection discontinuous Galerkin finite element method for conservation laws III: One-dimensional systems. *Journal of Computational Physics*, Elsevier, v. 84, n. 1, p. 90–113, 1989. 25, 49
- COCKBURN, B.; SHU, C.-W. TVB Runge-Kutta local projection discontinuous Galerkin finite element method for conservation laws II: General framework. *Math. Comp*, v. 52, n. 186, p. 411–435, 1989. 25
- COCKBURN, B.; SHU, C.-W. The runge–kutta discontinuous galerkin method for conservation laws v: multidimensional systems. *Journal of Computational Physics*, Elsevier, v. 141, n. 2, p. 199–224, 1998. 54
- COCKBURN, B.; SHU, C.-W. Runge–kutta discontinuous galerkin methods for convection-dominated problems. *Journal of scientific computing*, Springer, v. 16, n. 3, p. 173–261, 2001. 25
- COLELLA, P.; WOODWARD, P. R. The piecewise parabolic method (PPM) for gas-dynamical simulations. *Journal of computational physics*, Elsevier, v. 54, n. 1, p. 174–201, 1984. 25

- CONTRERAS, F. et al. A cell-centered multipoint flux approximation method with a diamond stencil coupled with a higher order finite volume method for the simulation of oil–water displacements in heterogeneous and anisotropic petroleum reservoirs. *Computers & Fluids*, Elsevier, v. 127, p. 1–16, 2016. 21, 24, 25, 27, 29, 34, 35, 36, 65, 97, 99, 100
- CONTRERAS, F. R. L.; LYRA, P. R. M. et al. Um método de volumes finitos centrado na célula para a simulação de escoamentos bifásicos em reservatórios de petróleo heterogêneos e anisotrópico. Universidade Federal de Pernambuco, 2012. 27
- CRUMPTON, P.; SHAW, G.; WARE, A. Discretisation and multigrid solution of elliptic equations with mixed derivative terms and strongly discontinuous coefficients. *Journal of Computational Physics*, Elsevier, v. 116, n. 2, p. 343–358, 1995. 24
- DELIS, A.; NIKOLOS, I. A novel multidimensional solution reconstruction and edge-based limiting procedure for unstructured cell-centered finite volumes with application to shallow water dynamics. *International Journal for Numerical Methods in Fluids*, Wiley Online Library, v. 71, n. 5, p. 584–633, 2013. 25, 65
- DIAZ, M. C. et al. Two-dimensional sediment transport models in shallow water equations. a second order finite volume approach on unstructured meshes. *Computer Methods in Applied Mechanics and Engineering*, Elsevier, v. 198, n. 33, p. 2520–2538, 2009. 25, 65
- DUMBSER, M. Arbitrary high order pnpm schemes on unstructured meshes for the compressible navier–stokes equations. *Computers & Fluids*, Elsevier, v. 39, n. 1, p. 60–76, 2010. 25
- DUMBSER, M. et al. A unified framework for the construction of one-step finite volume and discontinuous galerkin schemes on unstructured meshes. *Journal of Computational Physics*, Elsevier, v. 227, n. 18, p. 8209–8253, 2008. 25
- DUMBSER, M.; ZANOTTI, O. Very high order pnpm schemes on unstructured meshes for the resistive relativistic mhd equations. *Journal of Computational Physics*, Elsevier, v. 228, n. 18, p. 6991–7006, 2009. 25
- DURLOFSKY, L. J. A triangle based mixed finite element finite volume technique for modeling two phase flow through porous media. *Journal of Computational Physics*, Elsevier, v. 105, n. 2, p. 252–266, 1993. 25, 27, 61, 65
- EDWARDS, M. G. Higher-resolution hyperbolic-coupled-elliptic flux-continuous cvd schemes on structured and unstructured grids in 2-d. *International journal for numerical methods in fluids*, Wiley Online Library, v. 51, n. 9-10, p. 1059–1077, 2006. 27, 76
- EDWARDS, M. G. Global and local central non-upwind finite volume schemes for hyperbolic conservation laws in porous media. *International Journal for Numerical Methods in Fluids*, Wiley Online Library, v. 64, n. 7, p. 793–811, 2010. 27
- EDWARDS, M. G.; ROGERS, C. F. Finite volume discretization with imposed flux continuity for the general tensor pressure equation. *Computational geosciences*, Springer, v. 2, n. 4, p. 259–290, 1998. 24, 26
- EDWARDS, M. G.; ZHENG, H. A quasi-positive family of continuous darcy-flux finite-volume schemes with full pressure support. *Journal of Computational Physics*, Elsevier, v. 227, n. 22, p. 9333–9364, 2008. 24

- ENGQUIST, B.; LÖTSTEDT, P.; RUNBORG, O. *Multiscale modeling and simulation in science*. [S.l.]: Springer Science & Business Media, 2009. v. 66. 69
- ERN, A. et al. Accurate velocity reconstruction for discontinuous galerkin approximations of two-phase porous media flows. *Comptes Rendus Mathematique*, v. 347, n. 9, p. 551, 2009. 26
- EVJE, S.; FRIIS, H. A. Numerical treatment of two-phase flow in capillary heterogeneous porous media by finite-volume approximations. *International Journal of Numerical Analysis & Modeling*, Institute for Scientific Computing and Information at Wuhan University, Anshan University of Science and Technology and University of Alberta, v. 9, n. 3, p. 505–528, 2012. 60, 67, 97
- EWING, R. E. *The mathematics of reservoir simulation*. [S.l.]: SIAM, 1983. 26
- EWING, R. E. *The mathematics of reservoir simulation*. [S.l.]: Society for Industrial Mathematics, 1984. v. 1. 26
- EYMARD, R.; GUICHARD, C.; MASSON, R. Grid orientation effect in coupled finite volume schemes. *IMA Journal of Numerical Analysis*, Oxford University Press, v. 33, n. 2, p. 582–608, 2012. 26
- FANCHI, J. R. *Principles of applied reservoir simulation*. [S.l.]: Gulf Professional Publishing, 2005. 30
- FERNANDES, B. R. B. et al. A 3d total variation diminishing scheme for compositional reservoir simulation using the element-based finite-volume method. *Numerical Heat Transfer, Part A: Applications*, Taylor & Francis, v. 67, n. 8, p. 839–856, 2015. 27
- FERNANDES, B. R. B.; MARCONDES, F.; SEPEHRNOORI, K. Investigation of several interpolation functions for unstructured meshes in conjunction with compositional reservoir simulation. *Numerical Heat Transfer, Part A: Applications*, Taylor & Francis, v. 64, n. 12, p. 974–993, 2013. 27
- GALINDEZ, R. G. *Método espectral dos volumes finitos para simulação 1-D de escoamentos bifásicos em reservatórios de petróleo*. Dissertação (Mestrado) — Federal Universty of Pernambuco (UFPE), Recife, Brazil, 1 2014. 27
- GALINDEZ-RAMIREZ, G. et al. Numerical simulation of 1-d oil and water displacements in petroleum reservoirs using the spectral finite volume method. *Journal of the Brazilian Society of Mechanical Sciences and Engineering*, Springer, v. 39, n. 7, p. 2687–2700, 2017. 27
- GAO, Z.; WU, J. A linearity-preserving cell-centered scheme for the heterogeneous and anisotropic diffusion equations on general meshes. *International Journal for Numerical Methods in Fluids*, Wiley Online Library, v. 67, n. 12, p. 2157–2183, 2010. 21, 24, 35, 36, 97, 99, 100
- GENUCHTEN, M. T. V. A closed-form equation for predicting the hydraulic conductivity of unsaturated soils 1. *Soil science society of America journal*, Soil Science Society of America, v. 44, n. 5, p. 892–898, 1980. 31
- GERRITSEN, M. G.; DURLOFSKY, L. J. Modeling fluid flow in oil reservoirs. *Annu. Rev. Fluid Mech.*, Annual Reviews, v. 37, p. 211–238, 2005. 34
- GODUNOV, S. A finite-difference method for the numerical computation of discontinuous solutions of the equations of fluid dynamics. *Mat. Sb*, v. 47, n. 271, 1959. 25

- GOTTLIEB, S.; SHU, C.-W. Total variation diminishing runge-kutta schemes. *Mathematics of computation of the American Mathematical Society*, v. 67, n. 221, p. 73–85, 1998. 60
- HÆGLAND, H. et al. Improved streamlines and time-of-flight for streamline simulation on irregular grids. *Advances in Water Resources*, Elsevier, v. 30, n. 4, p. 1027–1045, 2007. 38
- HÆGLAND, H. et al. Adaptive streamline tracing for streamline simulation on irregular grids. In: *Proceedings of the XVI International Conference on Computational Methods in Water Resources, Copenhagen, Denmark*. [S.l.: s.n.], 2006. p. 18–22. 78
- HARTEN, A. High resolution schemes for hyperbolic conservation laws. *Journal of computational physics*, Elsevier, v. 49, n. 3, p. 357–393, 1983. 25
- HARTEN, A. et al. Uniformly high order accurate essentially non-oscillatory schemes, iii. In: *Upwind and high-resolution schemes*. [S.l.]: Springer, 1987. p. 218–290. 25
- HELMIG, R. *Multiphase flow and transport processes in the subsurface*. [S.l.]: Springer Berlin, 1997. v. 6. 28, 31, 73
- HESTHAVEN, J.; WARBURTON, T. Nodal discontinuous galerkin methods. *Texts in Applied Mathematics*, v. 54, 2008. 25, 51, 54, 55, 57, 59, 62
- HIRSCH, C. *Numerical computation of internal and external flows: the fundamentals of computational fluid dynamics*. [S.l.]: Butterworth-Heinemann, 2007. v. 1. 61, 62
- HOTEIT, H.; FIROOZABADI, A. et al. Compositional modeling by the combined discontinuous galerkin and mixed methods. *SPE Journal*, Society of Petroleum Engineers, v. 11, n. 01, p. 19–34, 2006. 26, 68
- HU, C.; SHU, C.-W. Weighted essentially non-oscillatory schemes on triangular meshes. *Journal of Computational Physics*, v. 150, n. 1, p. 97–127, 1999. 25
- HUYNH, H. A flux reconstruction approach to high-order schemes including discontinuous galerkin methods. *AIAA paper*, v. 4079, p. 2007, 2007. 26, 39, 42, 43, 44, 45
- JALALI, A.; GOOCH, C. F. O. An hp-adaptive unstructured finite volume solver for compressible aerodynamic flows. In: *55th AIAA Aerospace Sciences Meeting*. [S.l.: s.n.], 2017. p. 0082. 25
- KIM, D.; CHOI, H. A second-order time-accurate finite volume method for unsteady incompressible flow on hybrid unstructured grids. *Journal of computational physics*, Elsevier, v. 162, n. 2, p. 411–428, 2000. 25, 65
- KOZDON, J. E.; MALLISON, B. T.; GERRITSEN, M. G. Multidimensional upstream weighting for multiphase transport in porous media. *Computational Geosciences*, Springer, v. 15, n. 3, p. 399–419, 2011. 21
- KUZMIN, D.; SHASHKOV, M. J.; SVYATSKIY, D. A constrained finite element method satisfying the discrete maximum principle for anisotropic diffusion problems. *Journal of Computational Physics*, Elsevier, v. 228, n. 9, p. 3448–3463, 2009. 24
- LAMINE, M. S. *Multi-dimensional higher resolution methods for flow in porous media*. [S.l.]: Swansea University (United Kingdom), 2009. 61

- LAMINE, S.; EDWARDS, M. G. Multidimensional upwind convection schemes for flow in porous media on structured and unstructured quadrilateral grids. *Journal of computational and applied mathematics*, Elsevier, v. 234, n. 7, p. 2106–2117, 2010. 27
- LEER, B. V. Towards the ultimate conservative difference scheme. V. A second-order sequel to Godunov's method. *Journal of computational Physics*, Elsevier, v. 32, n. 1, p. 101–136, 1979. 25, 65
- LEPOTIER, C. Schéma volumes finis monotone pour des opérateurs de diffusion fortement anisotropes sur des maillages de triangles non structurés. *Comptes Rendus Mathématique*, Elsevier Masson, v. 341, n. 12, p. 787–792, 2005. 24
- LI, J.; RIVIERE, B. High order discontinuous galerkin method for simulating miscible flooding in porous media. *Computational Geosciences*, Springer, v. 19, n. 6, p. 1251–1268, 2015. 26
- LI, J.; RIVIERE, B. Numerical solutions of the incompressible miscible displacement equations in heterogeneous media. *Computer Methods in Applied Mechanics and Engineering*, Elsevier, v. 292, p. 107–121, 2015. 26
- LIPNIKOV, K. et al. Monotone finite volume schemes for diffusion equations on unstructured triangular and shape-regular polygonal meshes. *Journal of Computational Physics*, Elsevier, v. 227, n. 1, p. 492–512, 2007. 24
- LIU, Y.; VINOKUR, M.; WANG, Z. Discontinuous spectral difference method for conservation laws on unstructured grids. In: *Computational Fluid Dynamics 2004*. [S.l.]: Springer, 2006. p. 449–454. 26
- LIU, Y.; VINOKUR, M.; WANG, Z. J. Spectral difference method for unstructured grids i: basic formulation. *Journal of Computational Physics*, Elsevier, v. 216, n. 2, p. 780–801, 2006. 26
- LÓPEZ, M. R. et al. Verification and validation of hifiles: a high-order les unstructured solver on multi-gpu platforms. In: *32nd AIAA Applied Aerodynamics Conference*. [S.l.: s.n.], 2014. p. 3168. 26
- LUO, H. et al. A reconstructed discontinuous galerkin method for the compressible navier–stokes equations on arbitrary grids. *Journal of Computational Physics*, Elsevier, v. 229, n. 19, p. 6961–6978, 2010. 25
- LUO, H. et al. A reconstructed discontinuous galerkin method based on a hierarchical weno reconstruction for compressible flows on tetrahedral grids. *Journal of Computational Physics*, Elsevier, v. 236, p. 477–492, 2013. 25
- LYRA, P. R. M. *Unstructured grid adaptive algorithms for fluid dynamics and heat conduction*. Tese (Doutorado) — University of Wales Swansea, 1994. 62
- MATRINGE, S. F.; JUANES, R.; TCHELEPI, H. A. Robust streamline tracing for the simulation of porous media flow on general triangular and quadrilateral grids. *Journal of Computational Physics*, Elsevier, v. 219, n. 2, p. 992–1012, 2006. 37, 38
- MAY, G.; JAMESON, A. A spectral difference method for the euler and navier-stokes equations on unstructured meshes. In: *44th AIAA Aerospace Sciences Meeting and Exhibit*. [S.l.: s.n.], 2006. p. 304. 26

- MURAD, M. A. et al. A new locally conservative numerical method for two-phase flow in heterogeneous poroelastic media. *Computers and Geotechnics*, Elsevier, v. 48, p. 192–207, 2013. 27
- MURAD, M. A. et al. New locally conservative numerical schemes for hydrogeomechanical couplings in strongly heterogeneous presalt reservoirs. In: SOCIETY OF PETROLEUM ENGINEERS. *SPE Reservoir Simulation Symposium*. [S.l.], 2013. 27
- NIKITIN, K.; TEREKHOV, K.; VASSILEVSKI, Y. A monotone nonlinear finite volume method for diffusion equations and multiphase flows. *Computational Geosciences*, Springer, v. 18, n. 3-4, p. 311–324, 2014. 80
- NOGUEIRA, X. et al. On the simulation of wave propagation with a higher-order finite volume scheme based on reproducing kernel methods. *Computer Methods in Applied Mechanics and Engineering*, Elsevier, v. 199, n. 23-24, p. 1471–1490, 2010. 62
- NORDBOTTEN, J. M.; AAVATSMARK, I.; EIGESTAD, G. Monotonicity of control volume methods. *Numerische Mathematik*, Springer, v. 106, n. 2, p. 255–288, 2007. 24
- PARK, J. S.; KIM, C. Hierarchical multi-dimensional limiting strategy for correction procedure via reconstruction. *Journal of Computational Physics*, Elsevier, v. 308, p. 57–80, 2016. 51, 52, 53, 62
- PEACEMAN, D. W. *Fundamentals of numerical reservoir simulation*. [S.l.]: Elsevier, 1977. v. 6. 21, 26, 29
- RAVIART, P.; THOMAS, J. A mixed finite element method for 2-nd order elliptic problems. *Mathematical Aspects of Finite Element Methods*, Springer, p. 292–315, 1977. 35, 37
- REED, W. H.; HILL, T. *Triangular mesh methods for the neutron transport equation*. [S.l.], 1973. 25
- RICCHIUTO, M.; CSÍK, Á.; DECONINCK, H. Residual distribution for general time-dependent conservation laws. *Journal of Computational Physics*, Elsevier, v. 209, n. 1, p. 249–289, 2005. 25
- RIVIERE, B. Discontinuous galerkin finite element methods for solving the miscible displacement problem in porous media. *Ph. D. thesis, The University of Texas at Austin*, 2000. 26
- RIVIERE, B. *Discontinuous Galerkin methods for solving elliptic and parabolic equations: theory and implementation*. [S.l.]: SIAM, 2008. 26
- RIVIÈRE, B.; WHEELER, M. F. Discontinuous galerkin methods for flow and transport problems in porous media. *Communications in numerical methods in engineering*, Wiley Online Library, v. 18, n. 1, p. 63–68, 2002. 26
- SHELDON, J.; JR, W. C. et al. One-dimensional, incompressible, noncapillary, two-phase fluid flow in a porous medium. Society of Petroleum Engineers, 1959. 34
- SHU, C.-W. Essentially non-oscillatory and weighted essentially non-oscillatory schemes for hyperbolic conservation laws. In: *Advanced numerical approximation of nonlinear hyperbolic equations*. [S.l.]: Springer, 1998. p. 325–432. 49

- SHU, C.-W.; OSHER, S. Efficient implementation of essentially non-oscillatory shock-capturing schemes, ii. *Journal of Computational Physics*, Elsevier, v. 83, n. 1, p. 32–78, 1989. 48
- SOUZA, M. R. *Simulação Numérica de Escoamento Bifásico em Reservatórios de Petróleo Heterogêneos e Anisotrópicos Utilizando um Método de Volumes Finitos Verdadeiramente Multidimensional com Aproximação de Alta Ordem*. Tese (Doutorado) — Tese de Doutorado, Universidade Federal de Pernambuco (UFPE), Recife, in Portuguese., 2015. 21, 25, 31, 34, 61, 82
- SOUZA, M. R. et al. A higher-resolution flow-oriented scheme with an adaptive correction strategy for distorted meshes coupled with a robust mpfa-d method for the numerical simulation of two-phase flow in heterogeneous and anisotropic petroleum reservoirs. *SPE Journal*, Society of Petroleum Engineers, 2018. 97
- SPEKREIJSE, S. Multigrid solution of monotone second-order discretizations of hyperbolic conservation laws. *Mathematics of Computation*, v. 49, n. 179, p. 135–155, 1987. 25, 65
- SRINIVASAN, G.; LIPNIKOV, K. On the reconstruction of darcy velocity in finite-volume methods. *Transport in porous media*, Springer, v. 96, n. 2, p. 337–351, 2013. 35, 73
- SUN, S.; WHEELER, M. F. Discontinuous galerkin methods for coupled flow and reactive transport problems. *Applied Numerical Mathematics*, Elsevier, v. 52, n. 2-3, p. 273–298, 2005. 26
- TANEJA, A.; HIGDON, J. A fully-coupled discontinuous galerkin spectral element method for two-phase flow in petroleum reservoirs. *Journal of Computational Physics*, Elsevier, v. 352, p. 341–372, 2018. 26
- TREFETHEN, L. N. *Spectral methods in MATLAB*. [S.l.]: Siam, 2000. v. 10. 61
- VINCENT, P. E.; CASTONGUAY, P.; JAMESON, A. A new class of high-order energy stable flux reconstruction schemes. *Journal of Scientific Computing*, Springer, v. 47, n. 1, p. 50–72, 2011. 26, 45
- WANG, Z.; GAO, H. A unifying lifting collocation penalty formulation including the discontinuous galerkin, spectral volume/difference methods for conservation laws on mixed grids. *Journal of Computational Physics*, Elsevier, v. 228, n. 21, p. 8161–8186, 2009. 26, 40
- WANG, Z.; GAO, H.; HAGA, T. A unifying discontinuous formulation for hybrid meshes. *Adaptive High-Order Methods in Computational Fluid Dynamics*, Edited by ZJ Wang, World Scientific Publishing, World Scientific, 2011. 26, 40
- WANG, Z. J. Spectral (Finite) Volume Method for Conservation Laws on Unstructured Grids. Basic Formulation. *Journal of Computational Physics*, Elsevier, v. 178, n. 1, p. 210–251, 2002. 26, 51
- WANG, Z. J. *Adaptive high-order methods in computational fluid dynamics*. [S.l.]: World Scientific, 2011. v. 2. 62
- WANG, Z. J.; LIU, Y. Spectral (finite) volume method for conservation laws on unstructured grids: II. Extension to two-dimensional scalar equation. *Journal of Computational Physics*, Elsevier, v. 179, n. 2, p. 665–697, 2002. 26

- WANG, Z. J.; LIU, Y. Spectral (finite) volume method for conservation laws on unstructured grids iii: One dimensional systems and partition optimization. *Journal of Scientific Computing*, Springer, v. 20, n. 1, p. 137–157, 2004. 26
- WANG, Z. J. et al. Spectral difference method for unstructured grids ii: extension to the euler equations. *Journal of Scientific Computing*, Springer, v. 32, n. 1, p. 45–71, 2007. 26
- WANG, Z. J.; ZHANG, L.; LIU, Y. Spectral (finite) volume method for conservation laws on unstructured grids IV: extension to two-dimensional systems. *Journal of Computational Physics*, Elsevier, v. 194, n. 2, p. 716–741, 2004. 26
- WITHERDEN, F. D. et al. *On the development and implementation of high-order flux reconstruction schemes for computational fluid dynamics*. Tese (Doutorado) — PhD thesis, Imperial College London, 2015. 26
- YANOSIK, J.; MCCRACKEN, T. A nine-point, finite-difference reservoir simulator for realistic prediction of adverse mobility ratio displacements. *Society of Petroleum Engineers Journal*, Society of Petroleum Engineers, v. 19, n. 04, p. 253–262, 1979. 82
- YU, M.; WANG, Z.; LIU, Y. On the accuracy and efficiency of discontinuous galerkin, spectral difference and correction procedure via reconstruction methods. *Journal of Computational Physics*, Elsevier, v. 259, p. 70–95, 2014. 26
- ZHANG, L. et al. A class of hybrid dg/fv methods for conservation laws i: Basic formulation and one-dimensional systems. *Journal of Computational Physics*, Elsevier, v. 231, n. 4, p. 1081–1103, 2012. 25
- ZHANG, L. et al. A class of hybrid dg/fv methods for conservation laws ii: Two-dimensional cases. *Journal of Computational Physics*, Elsevier, v. 231, n. 4, p. 1104–1120, 2012. 25
- ZHANG, X.; LIANG, C.; YANG, J. A high-order flux reconstruction/correction procedure via reconstruction method for shock capturing with space-time extension time stepping and adaptive mesh refinement. In: *55th AIAA Aerospace Sciences Meeting*. [S.l.: s.n.], 2017. p. 0519. 26
- ZIMMERMAN, B. J.; WANG, Z. J. The efficient implementation of correction procedure via reconstruction with gpu computing. In: *21st AIAA Computational Fluid Dynamics Conference*. [S.l.: s.n.], 2013. p. 2692. 26, 45

Annex

ANNEX A – Multipoint Flux Approximation-Diamond type (MPFA-D) Finite Volume Method

In this annex, we discuss in detail the MPFA-D method, including a description of important variable names.

A.1 Solution of implicitly discretized pressure equation by the MPFA-D method

Pressure is implicitly estimated by solving the following elliptic equation

$$\vec{\nabla} \cdot \vec{v} = Q, \quad \text{with} \quad \vec{v} = -\lambda K(\nabla p - \rho \vec{g}) \quad (\text{A.1})$$

via the MPFA-D method, where λ is the total mobility, i.e., $\lambda = \lambda_w + \lambda_o$. Then, the last equation is integrated over the whole continuous domain Ω , to obtain

$$\int_{\Omega} \vec{\nabla} \cdot \vec{v} = \int_{\Omega} Q \quad (\text{A.2})$$

In the following, the physical domain Ω with boundary Γ is partitioned into a finite number of sub-domains \mathcal{N} , namely CVs (Control Volumes) denoted by Ω_i , such that $\Omega = \bigcup_{i=1}^{\mathcal{N}} \Omega_i$. By integrating the pressure Eq. (A.1) over a control volume Ω_i and by applying the Gauss divergence theorem, we have

$$\int_{\Gamma_i} \vec{v} \cdot \vec{n} dA = \int_{\Omega_i} Q \partial \Omega_i \quad (\text{A.3})$$

with \vec{n} being the unit outward normal vector to the control surface Γ_i . After, the left hand and right hand sides of Eq. (A.3), can be approximated by

$$\int_{\Gamma_i} \vec{v} \cdot \vec{n} \partial \Gamma_i \cong \sum_{IJ \in \Gamma_i} \vec{v}_{IJ} \cdot \vec{N}_{IJ} \quad \text{and} \quad \int_{\Omega_i} Q \partial \Omega_i = \bar{Q}_i V_i \quad (\text{A.4})$$

where, V_i is the volume (area in 2D) of the control volume Ω_i and \bar{Q}_i is an average value of Q and \vec{v}_{IJ} is the total flow rate on the control surface (edge in 2D domains) formed by nodes I and J as illustrated in Fig. 37. The normal vector to this face is denoted by \vec{N}_{IJ} , such as $|\vec{N}_{IJ}| = |\vec{IJ}|$ with $|\vec{IJ}|$ being the length of the edge \vec{IJ} .

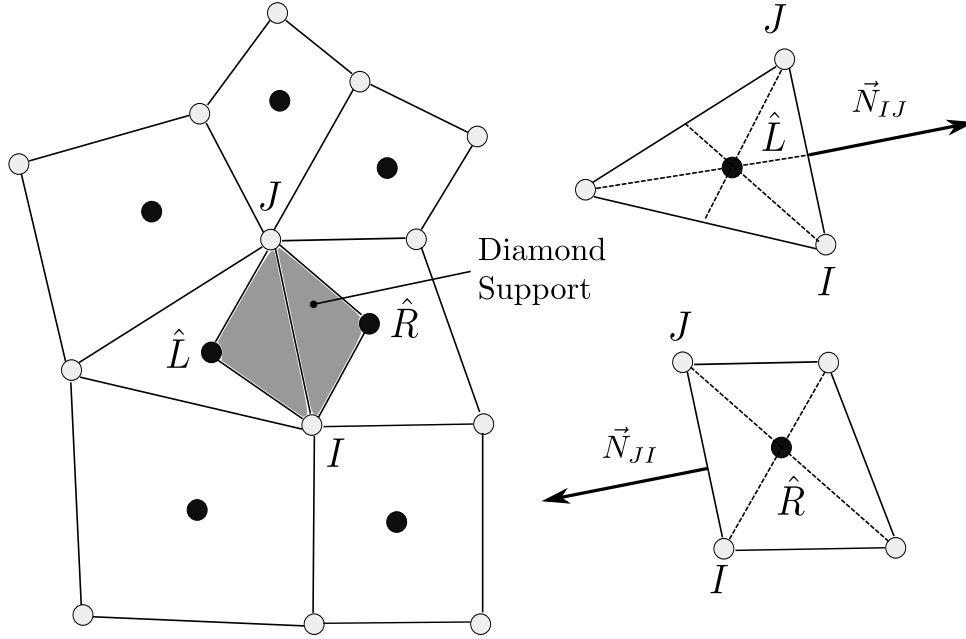
Then, the summation is performed over all faces that make up the control volume. From Eqs. (A.4) we can write

$$\sum_{IJ \in \Gamma_i} \vec{v}_{IJ} \cdot \vec{N}_{IJ} = \bar{Q}_i V_i \quad (\text{A.5})$$

with

$$\vec{v}_{IJ} = \frac{1}{|\vec{N}_{IJ}|} \int_{\Gamma} \vec{v} \partial \Gamma \quad \text{and} \quad \bar{Q}_i = \frac{1}{V_i} \int_{\Omega_i} Q \partial \Omega_i \quad (\text{A.6})$$

Figure 37 – Part of a polygonal mesh, illustrating the diamond path.



Source: Adapted from Contreras et al. (2016).

By Darcy's Law, in Eq. (A.1), the approximate velocity \vec{v}_{IJ} varies with the permeability tensor and the total mobility on the face. In order to maintain a second order approximation for mobility, it can be defined by

$$\lambda_{IJ}(S_w) = \frac{\lambda_I(S_w) + \lambda_J(S_w)}{2} \quad (\text{A.7})$$

where, $\lambda_I(S_w)$ and $\lambda_J(S_w)$ are the nodal mobilities on I and J nodes respectively. On the other hand, the nodal mobilities are approximated by using a weight average (EVJE; FRIIS, 2012; CONTRERAS et al., 2016; SOUZA et al., 2018), so that

$$\lambda_I(S_w) = \frac{\sum_{i=1}^{\mathcal{N}_I} \lambda_i(S_w) V_i}{\sum_{i=1}^{\mathcal{N}_I} V_i} \quad \text{and} \quad \lambda_J(S_w) = \frac{\sum_{i=1}^{\mathcal{N}_J} \lambda_i(S_w) V_i}{\sum_{i=1}^{\mathcal{N}_J} V_i} \quad (\text{A.8})$$

where $\lambda_i(S_w)$ is the total mobility in the control volume i and \mathcal{N}_I and \mathcal{N}_J are the numbers of CVs surrounding nodes I and J , respectively.

The numerical discretization of Eq. (A.5) is obtained via the method proposed by Gao e Wu (2010). This method ensures that the pressure field solutions obtained are piecewise linear, requiring that the approximate pressure gradient satisfy the following Lemma (GAO; WU, 2010).

Lemma A.1.1 Assume that p is a pressure function, which has been defined into the triangle ΔABC , with vertices A, B and C in counterclockwise order. Then

$$\vec{\nabla} p \cong \frac{p_A - p_B}{|AB|} \vec{AB} + \frac{\mathfrak{R} \vec{AB}}{|AB|^2} [(p_B - p_A) \cot \angle BCA + (p_C - p_A) \cot \angle ABC] \quad (\text{A.9})$$

where the counterclockwise rotation matrix is given by

$$\mathfrak{R} = \begin{bmatrix} \cos \theta & \sin \theta \\ -\sin \theta & \cos \theta \end{bmatrix}, \text{ with } \theta = \frac{\pi}{2} \quad (\text{A.10})$$

Via o Lemma A.1.1 the estimated gradient on left (\hat{L}) and right (\hat{R}) CVs can be written, respectively, as

$$\nabla p_{IJ}^{\hat{L}} \cong \frac{p_J - p_I}{|\vec{IJ}|} \vec{IJ} + \frac{\mathfrak{R}\vec{IJ}}{|\vec{IJ}|^2} [(p_I - p_{\hat{L}}) \cot \angle IJ\hat{L} + (p_J - p_{\hat{L}}) \cot \angle \hat{L}IJ] \quad (\text{A.11})$$

$$\nabla p_{IJ}^{\hat{R}} \cong \frac{p_I - p_J}{|\vec{JI}|} \vec{JI} + \frac{\mathfrak{R}\vec{JI}}{|\vec{JI}|^2} [(p_I - p_{\hat{R}}) \cot \angle \hat{R}JI + (p_J - p_{\hat{R}}) \cot \angle JI\hat{R}] \quad (\text{A.12})$$

In Eqs. (A.11) and (A.12) $p_I, p_J, p_{\hat{L}}$ and $p_{\hat{R}}$ are the pressures at the vertices of the triangles $\Delta \hat{L}IJ$ and $\Delta \hat{R}JI$. From Eq. (A.11), by considering the triangle $\Delta \hat{L}IJ$, we can approximate the flow on the control surface \vec{IJ} , corresponding to the left CV, as

$$\vec{v}_{IJ}^{\hat{L}} \cdot \vec{N}_{IJ} \cong -\lambda_{IJ} \left\{ K_{IJ_{\hat{L}}}^{(n)} [(p_I - p_{\hat{L}}) \cot \angle IJ\hat{L} + (p_J - p_{\hat{L}}) \cot \angle \hat{L}IJ] + K_{IJ_{\hat{L}}}^{(t)} (p_J - p_I) \right\} \quad (\text{A.13})$$

with the superscripts (n) and (t) being the normal and tangential directions, respectively.

Analogously, by using the gradient computed in Eq. (A.12), we can now derive the other side flux $\vec{v}_{IJ}^{\hat{R}} \cdot \vec{N}_{JI}$ considering the triangle $\Delta \hat{R}JI$ corresponding to the right CV.

The projections of the permeability tensor of the adjacent CVs that share the face \vec{IJ} on the normal and tangential directions to this edge are computed in the following form

$$K_{IJ_{\hat{i}}}^{(n)} = \frac{(\vec{N}_{IJ})^T K_{\hat{i}}(\vec{N}_{IJ})}{|\vec{IJ}|^2}, \quad K_{IJ_{\hat{i}}}^{(t)} = \frac{(\vec{N}_{IJ})^T K_{\hat{i}}(\vec{IJ})}{|\vec{IJ}|^2} \quad (\text{A.14})$$

with $\hat{i} = \hat{L}, \hat{R}$ and $\vec{N}_{IJ} = \mathfrak{R}\vec{IJ}$.

By using the above equation, then, Eq. (A.13) can be rewritten as

$$\begin{aligned} \frac{h_{IJ}^{\hat{L}}}{\lambda_{IJ} K_{IJ_{\hat{L}}}^{(n)}} \vec{v}_{IJ}^{\hat{L}} \cdot \vec{N}_{IJ} \cong & -\frac{1}{|\vec{IJ}|} \left((p_I - p_{\hat{L}}) \frac{\vec{J}\hat{L} \cdot \vec{JI}}{|\vec{JI}|} + (p_J - p_{\hat{L}}) \frac{\vec{I}\hat{L} \cdot \vec{IJ}}{|\vec{JI}|} \right) \\ & - (p_J - p_I) h_{IJ}^{\hat{L}} \frac{K_{IJ_{\hat{L}}}^{(t)}}{K_{IJ_{\hat{L}}}^{(n)}} \end{aligned} \quad (\text{A.15})$$

where $h_{IJ}^{\hat{L}}$ is the distance from the centroids of the left control volume to the edge \vec{IJ} . It is worthwhile to highlight that the geometric and physical parameters in Eqs. (A.14) and (A.15) are calculated in a preprocessing stage.

Imposing flux continuity throught the control surface \vec{IJ} , yields

$$\vec{v}_{IJ}^{\hat{L}} \cdot \vec{N}_{IJ} = -\vec{v}_{IJ}^{\hat{R}} \cdot \vec{N}_{JI} = \vec{v}_{IJ} \cdot \vec{N}_{IJ} \quad (\text{A.16})$$

and by using Eqs. (A.14)-(A.16) and after some algebraic manipulation, the continuity equation can be written as

$$\begin{aligned} \left(\frac{h_{IJ}^{\hat{L}} K_{IJ_{\hat{R}}}^{(n)} + h_{IJ}^{\hat{R}} K_{IJ_{\hat{L}}}^{(n)}}{\lambda_{IJ} K_{IJ_{\hat{R}}}^{(n)} K_{IJ_{\hat{L}}}^{(n)}} \right) \vec{v}_{IJ} \cdot \vec{N}_{IJ} = - |\vec{IJ}| (p_{\hat{R}} - p_{\hat{L}}) \\ + \left(\frac{\vec{IJ} \cdot \vec{\hat{L}\hat{R}}}{|\vec{IJ}|} - \left[h_{IJ}^{\hat{L}} \frac{K_{IJ_{\hat{L}}}^{(t)}}{K_{IJ_{\hat{L}}}^{(n)}} + h_{IJ}^{\hat{R}} \frac{K_{IJ_{\hat{R}}}^{(t)}}{K_{IJ_{\hat{R}}}^{(n)}} \right] \right) (p_J - p_I) \end{aligned} \quad (\text{A.17})$$

Rearranging terms, Eq. (A.17) is compactly rewritten as

$$\vec{v}_{IJ} \cdot \vec{N}_{IJ} = \tau_{IJ} [p_{\hat{R}} - p_{\hat{L}} - \nu_{IJ} (p_J - p_I)] \quad (\text{A.18})$$

where, τ_{IJ} is the scalar transmissibility, given by

$$\tau_{IJ} = -\lambda_{IJ} \frac{K_{IJ_{\hat{L}}}^{(n)} K_{IJ_{\hat{R}}}^{(n)}}{K_{IJ_{\hat{L}}}^{(n)} h_{IJ}^{\hat{R}} + K_{IJ_{\hat{R}}}^{(n)} h_{IJ}^{\hat{L}}} |\vec{IJ}| \quad (\text{A.19})$$

and ν_{IJ} is a non-dimensional tangential parameter, which can be written as

$$\nu_{IJ} = \frac{\vec{IJ} \cdot \vec{\hat{L}\hat{R}}}{|\vec{IJ}|^2} - \frac{1}{|\vec{IJ}|} \left(\frac{K_{IJ_{\hat{L}}}^{(t)}}{K_{IJ_{\hat{L}}}^{(n)}} h_{IJ}^{\hat{L}} + \frac{K_{IJ_{\hat{R}}}^{(t)}}{K_{IJ_{\hat{R}}}^{(n)}} h_{IJ}^{\hat{R}} \right) \quad (\text{A.20})$$

Expression A.18 requires the values of pressure not only at the collocation points, but at the nodes that defines the edge \vec{IJ} under consideration. A LPEW (Linearity Preserving Explicit Weighted) interpolation described by Gao e Wu (2010) is adopted and will be briefly described in A.3.

Remark. In structured quadrilateral grids, the expression of the flow, given by Eq. (A.18), yields a nine-point cell-centered FV method. The tangential term in ν_{IJ} disappears if K is isotropic, and whenever we are using K-orthogonal grids the scheme becomes a TPFA (Two-Point Flux Approximation) scheme (CONTRERAS et al., 2016).

A.2 Treatment of boundary fluxes

For control surfaces \vec{IJ} over boundaries Γ_D with prescribed pressures (Dirichlet boundary conditions) and considering Eq. (A.17), we have

$$\vec{v}_{IJ} \cdot \vec{N}_{IJ} = \tau_{IJ} \left\{ p_{\hat{L}} + \frac{1}{|\vec{IJ}|} \left(g_D(I) \left[h_{IJ}^{\hat{L}} \frac{K_{IJ_{\hat{L}}}^{(t)}}{K_{IJ_{\hat{L}}}^{(n)}} - \frac{\vec{J\hat{L}} \cdot \vec{J\hat{I}}}{|\vec{IJ}|} \right] - g_D(J) \left[h_{IJ}^{\hat{L}} \frac{K_{IJ_{\hat{L}}}^{(t)}}{K_{IJ_{\hat{L}}}^{(n)}} + \frac{\vec{I\hat{L}} \cdot \vec{I\hat{J}}}{|\vec{IJ}|} \right] \right) \right\} \quad (\text{A.21})$$

In above equation the transmissibility term is given by

$$\tau_{IJ} = \lambda_{IJ} \frac{K_{IJ_{\hat{L}}}^{(n)}}{h_{IJ}^{\hat{L}}} |\vec{IJ}| \quad (\text{A.22})$$

Using Eq. (A.17), for the case of control surfaces \vec{IJ} over boundaries Γ_N with imposed fluxes (Neumann boundary conditions) the flux can be written as

$$\vec{v}_{IJ} \cdot \vec{N}_{IJ} = g_N |\vec{IJ}| \quad (\text{A.23})$$

In Eqs. (A.21) and (A.23) nodal pressures are given by the scalar functions $g_D(J)$ and $g_D(I)$ defined on Γ_D and the prescribed flux on Γ_N is given by g_N .

A.3 Interpolating pressure on mesh nodes

To complete the MPFA-D scheme for solving the pressure equation, we need to compute the nodal pressure P_I as in explicit weight interpolation of the surrounding collocation pressure, as proposed by Gao e Wu (2010):

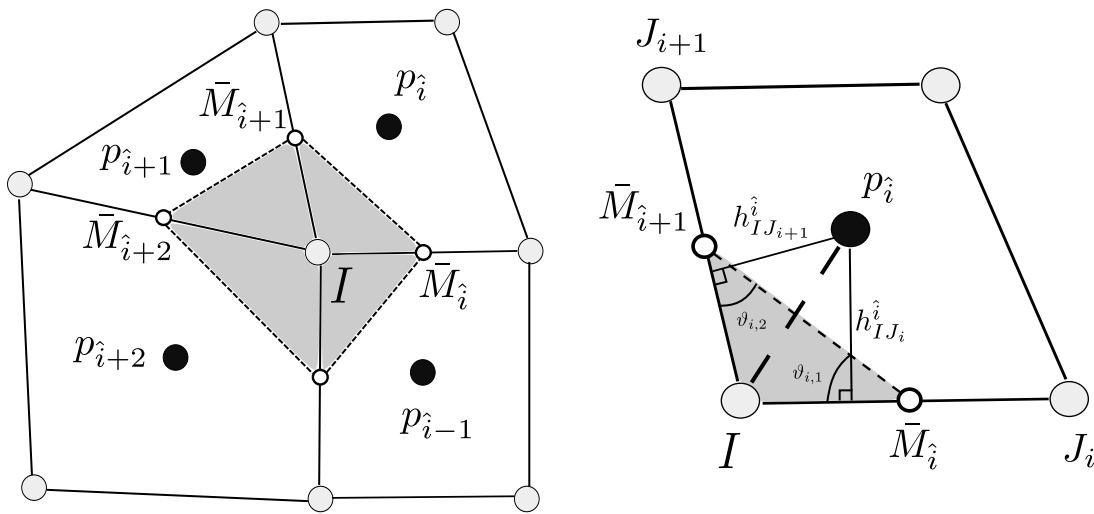
$$p_I = \sum_{\hat{i}=1}^{\mathcal{N}_{CV}} w_{\hat{i}} p_{\hat{i}} \quad (\text{A.24})$$

with \mathcal{N}_{CV} being the number of CVs that share the vertex I , see Fig. 38, and $w_{\hat{i}}$ is the weight associated with the CV \hat{i} calculated according to the following equation

$$w_{\hat{i}} = \frac{\bar{\omega}_{\hat{i}}}{\sum_{\hat{i}=1}^{\mathcal{N}_{CV}} \bar{\omega}_{\hat{i}}} \quad (\text{A.25})$$

in which $w_{\hat{i}}$ is a coefficient, and for further discussion and many more details, we refer to (GAO; WU, 2010; CONTRERAS et al., 2016) and references therein.

Figure 38 – Interaction region for the LPEW (Linearity Preserving Explicit Weighted) interpolation. On the left is shown the geometry for the interaction region in a grid fragment. On the right is illustrated the detail of the interaction region.



Source: Adapted from Contreras et al. (2016).